

Survey on 3D face reconstruction from uncalibrated images

Araceli Morales^a, Gemma Piella^a, Federico M. Sukno^a

^a*Pompeu Fabra University, Barcelona, Spain*

Abstract

Recently, a lot of attention has been focused on the incorporation of 3D data into face analysis and its applications. Despite providing a more accurate representation of the face, 3D face images are more complex to acquire than 2D pictures. As a consequence, great effort has been invested in developing systems that reconstruct 3D faces from an uncalibrated 2D image. However, the 3D-from-2D face reconstruction problem is ill-posed, thus prior knowledge is needed to restrict the solutions space. In this work, we review 3D face reconstruction methods in the last decade, focusing on those that only use 2D pictures captured under uncontrolled conditions. We present a classification of the proposed methods based on the technique used to add prior knowledge, considering three main strategies, namely, statistical model fitting, photometry, and deep learning, and reviewing each of them separately. In addition, given the relevance of statistical 3D facial models as prior knowledge, we explain the construction procedure and provide a comprehensive list of the publicly available 3D facial models. After the exhaustive study of 3D-from-2D face reconstruction approaches, we observe that the deep learning strategy is rapidly growing since the last few years, becoming the standard choice in replacement of the widespread statistical model fitting. Unlike the other two strategies, photometry-based methods have decreased in number since the required strong assumptions cause the reconstructions to be of more limited quality than those resulting from model fitting and deep learning methods. The review also identifies current gaps and suggests avenues for future research.

Keywords: 3D face reconstruction, 3D face imaging, 3D morphable model

1. Introduction

Facial analysis has been widely exploited in many different applications, including human-computer interaction [1, 2], security [3, 4], animation [5, 6], and even health [7, 8, 9, 10]. A recent trend in this field is to incorporate 3D data to overcome some of the intrinsic problems of the ubiquitous 2D facial analysis. Due to the 3D nature of the face, a 2D image is insufficient to accurately capture its geometry, as it collapses one dimension. Furthermore, 3D imaging provides a representation of the facial geometry that is invariant to pose and illumination, which are two of the major inconveniences of 2D imaging.

The advantages brought by 3D facial analysis systems come at the price of a more complex imaging process, which can often limit their scope. 3D facial information is usually captured using stereo-vision systems [11, 12, 13], 3D laser scanners [14] (e.g. NextEngine and Cyberware), and RGB-D cameras (such as Kinect). The first two capture high quality facial scans but require controlled environments and expensive machinery. In contrast, RGB-D cameras are cheaper and easier to use, but the resulting scans are of limited quality [15, 16].

An appealing alternative to capturing a 3D scan of the face is to estimate its geometry from an uncalibrated 2D picture [17, 18, 19]. This 3D-from-2D reconstruction alternative aims to combine the simplicity of capturing 2D images with the benefit of a 3D representation of the facial geometry.

Even though this approach is attractive, it is an inherently ill-posed problem. From a single picture, the individual facial geometry, the pose of the head and its texture (including illumination and colour) have to be recovered, which leads to an underdetermined problem. As a consequence, there are ambiguities in the solution of the 3D-from-2D face reconstruction since a single 2D picture can be generated from different 3D faces, and it is hard to determine which corresponds to the true geometry.

Recent methodological progress has helped to achieve remarkably convincing reconstructions, which has made it possible to use 3D-from-2D face reconstruction in a wide variety of fields [20, 21, 22, 23]. Some of them are even able to recover local details, such as wrinkles, or to reconstruct the 3D face from images viewed under extreme conditions, such as occlusions or large head poses [17, 18].

A key to their success is the addition of prior knowledge to resolve ambiguities in the solutions. In the last decade, we can distinguish three strategies for adding this prior information, namely, statistical model fitting, photometric stereo, and deep learning. In the first one, prior

Email addresses: mariadearaceli.morales@upf.com (Araceli Morales), gemma.piella@upf.com (Gemma Piella), federico.sukno@upf.com (Federico M. Sukno)

knowledge is encoded in a 3D facial model, built from a set of 3D facial scans, which is fitted to the input images. In the second one, a 3D template face or a 3D facial model is combined with photometric stereo methods to estimate the facial surface normals. Approaches under this strategy generally use information from multiple images, which further constrains the problem. In the last one, the 2D-3D mapping is directly learnt from a collection of 3D-2D pairs using deep learning systems that, after learning, encode prior knowledge of the geometry and appearance of faces.

In this work, we review the research on 3D face reconstruction from one or more uncalibrated 2D images in the last decade. For each of the three main strategies described separately (i.e., statistical model fitting, photometric stereo, and deep learning), we summarise, compare and discuss the most relevant approaches proposed in the last decade. We introduce a common mathematical framework to all the proposed methods whose notation is summarised in [Appendix A](#).

Although there are other reviews of the field [24, 25, 26, 27, 28, 29], none of them provides a in-depth and up-to-date study of the state-of-the-art research on 3D-from-2D face reconstruction. Stylianou and Lanitis [25] presented a survey on 3D face reconstruction from 2D images, but they only covered works up to 2009. The rapid expansion in this field over the last decade and the emergence of the deep learning techniques make this work obsolete. Also, Levine and Yu [24] presented a review of this topic, but narrowed it to reconstruction from single images, focusing on model fitting approaches for face recognition. More recently, Zollhöfer et al. [28] presented another review on 3D face reconstruction from single images, but they focused only on optimisation-based approaches, also missing methods based on deep learning and photometric stereo. This last work was updated in 2020 by Egger et al. [29]. They presented a very extensive survey specially focused on statistical facial models, reviewing 3D data acquisition, 3D facial model construction, and 2D image generation. Even though they included 3D face reconstruction, it is only reviewed as an application of the 3D facial models and they focused on single-image reconstruction (both RGB and RGB-D) and model fitting, discussing briefly methods based on deep learning. Other surveys of 3D face reconstruction, such as Suen et al. [26] and Widanagamaachchi and Dharmaratne [27], study the general strategies, discussing their strengths and drawbacks, but without providing an in-depth review of the most relevant works within each of them.

The remainder of this survey is organised as follows: in [Section 2](#), we first introduce the most popular way of constructing a statistical 3D facial model and list the publicly available models. In [Section 3](#), we review methods based on statistical model fitting. In [Sections 4](#) and [5](#), we review the photometry-based and deep learning approaches, respectively. [Section 6](#) groups methods that use other machine learning approaches, such as regression. Finally, in

[Section 7](#), a summary and conclusions are provided.

2. Statistical 3D Facial Models

As stated in the introduction, 3D-from-2D face reconstruction is an ill-posed problem, thus it requires some kind of prior knowledge to resolve the otherwise underdetermined solution.

Statistical 3D facial models are the most popular way of adding this prior information since they encode the geometric variations of the face, possibly in conjunction with the appearance. This kind of models consist of a mean face along with the modes of variation of its geometry and appearance. Fitting a 3D facial model to a photograph is done by estimating, apart from the model parameters, the 3D pose and the illumination such that the projection into the image plane of the resulting 3D face produces an image as similar as possible to the given picture.

In this section, we explain how the 3D facial models are built and provide a list of the ones that are publicly available. We refer to [29] for a detailed review on statistical facial models.

2.1. Construction of a 3D facial model

The most widespread statistical models of 3D faces are the 3D Morphable Models (3DMM), which were introduced to the community by Blanz and Vetter [30]. A 3DMM consists of a shape (i.e., geometry) model and, optionally, an albedo (a.k.a texture or colour) model, separately constructed using principal component analysis (PCA). In this work, we use texture, albedo or colour indistinctly, and we explicitly mention when the lighting is modelled separately from raw colour.

Let M be the number of 3D faces in the training set and N the number of vertices in each mesh. Let $\mathbf{x} = (x_1, y_1, z_1, \dots, x_N, y_N, z_N) \in \mathbb{R}^{3N}$ be the shape vector of a mesh, and $\mathbf{c} = (R_1, G_1, B_1, \dots, R_N, G_N, B_N) \in [0, 1]^{3N}$ the albedo vector that contains the R (red), G (green), and B (blue) values of the RGB colour model for each of the N vertices. The idea behind the 3DMM is that, if the set of 3D faces is sufficiently large, one can express any new textured shape as a linear combination of the shapes and textures of the training 3D faces:

$$\mathbf{x}_{\text{new}} = \sum_{m=1}^M a_m \mathbf{x}_m, \quad \mathbf{c}_{\text{new}} = \sum_{m=1}^M b_m \mathbf{c}_m$$

with $a_m, b_m \in \mathbb{R} \forall m = 1, \dots, M$.

Thus, we can parametrise any new face by its shape $\mathbf{x}_{\text{new}} = (a_1, \dots, a_M)^T$ and albedo $\mathbf{c}_{\text{new}} = (b_1, \dots, b_M)^T$. However, this parametrisation gets more complicated when the number of shapes in the training set M is large. PCA helps compressing the data, performing a basis transformation to an orthogonal coordinate system defined by the eigenvectors ϕ_i and ψ_i of the covariance matrices computed over the shapes and albedos in the training set. In

the orthogonal basis given by PCA,

$$\mathbf{x}_{\text{new}} = \bar{\mathbf{x}} + \sum_{i=1}^{M-1} \alpha_i \phi_i = \bar{\mathbf{x}} + \mathbf{\Phi} \alpha, \quad (1)$$

$$\mathbf{c}_{\text{new}} = \bar{\mathbf{c}} + \sum_{i=1}^{M-1} \beta_i \psi_i = \bar{\mathbf{c}} + \mathbf{\Psi} \beta, \quad (2)$$

with $\bar{\mathbf{x}} = \frac{1}{M} \sum_{m=1}^M \mathbf{x}_m$ the mean shape, $\alpha = (\alpha_1, \dots, \alpha_{M-1})^T \in \mathbb{R}^{M-1}$ the shape parameters of the model, and $\mathbf{\Phi} = (\phi_1, \dots, \phi_{M-1}) \in \mathbb{R}^{3N \times (M-1)}$ the matrix of the shape basis of the model; $\bar{\mathbf{c}}$, β and $\mathbf{\Psi}$ are analogously defined for the texture. The probability of the shape parameters $p(\alpha)$ is given by

$$p(\alpha) \propto \exp \left[-\frac{1}{2} \sum_{i=1}^{M-1} \left(\frac{\alpha_i}{\sigma_{\alpha_i}} \right)^2 \right] \quad (3)$$

where $\sigma_{\alpha_i}^2$ are the eigenvalues of the corresponding eigenvectors ϕ_i . The probability of the albedo parameters $p(\beta)$ is defined analogously.

Finally, the shape model of the 3DMM is defined by the mean shape, $\bar{\mathbf{x}}$, the eigenvectors of the shape covariance matrix, $\mathbf{\Phi}$, and the corresponding eigenvalues, $\{\sigma_{\alpha_i}^2\}_{i=1}^{M-1}$. Similarly, the albedo model is given by $\bar{\mathbf{c}}$, $\mathbf{\Psi}$, and $\{\sigma_{\beta_i}^2\}_{i=1}^{M-1}$.

However, some of the variation modes (eigenvectors ϕ_i , ψ_i) may have very small variance (eigenvalues $\sigma_{\alpha_i}^2$, $\sigma_{\beta_i}^2$), thus they are dispensable. Keeping only the directions that represent most of the variance of the training set allows us to reduce the dimension of the data, which is very useful when M is large. Assuming the eigenvalues $\sigma_{\xi_i}^2$ (denoting either $\sigma_{\alpha_i}^2$ or $\sigma_{\beta_i}^2$) are ordered in descending order, the \tilde{M} first eigenvectors with higher eigenvalues

$$\tilde{M} = \arg \max_{1 \leq m \leq M-1} \left\{ \sum_{i=1}^m \sigma_{\xi_i}^2 < \eta V_{\text{total}} \right\}.$$

keep the 100 η % of the total variance V_{total} .

Although most of the existing 3D statistical facial models are based on the procedure explained above, Jin et al. [31] claimed that a drawback of PCA is that it learns the data globally, so subtle information, such as wrinkles, is not captured. Therefore, it is very hard to reconstruct facial details by fitting a 3DMM. They proposed to apply non-negative matrix factorisation (NMF) instead of PCA since it decomposes a shape into localised features, which improves the reconstruction of the details.

Building a 3D facial model, either using PCA or NMF, requires full (i.e. dense) point-to-point correspondence across all of the faces in the training set. This is not an easy task since any small inaccuracy in the correspondence may lead to a model of poor quality. There are two main ways of establishing this dense correspondence: directly in 3D, usually deforming a 3D template non-rigidly, or in a common 2D space where all the 3D faces are projected, usually a UV-space.

Other techniques to build a 3D statistical facial model have been proposed, such as Brunton et al. [32], Lüthi et al. [33] and Tran and Liu [34]. However, we only explain the construction of the 3DMM, since they are the most-widespread 3D facial models.

2.2. Available 3D facial models

In the last decades, several 3DMM have been built and made public. Blanz and Vetter [30] constructed a morphable model with 200 laser scans of heads of young adults (100 males and 100 females). They put the 3D faces of the training set in point-to-point correspondence using an optical flow algorithm based on the flattening of the 3D faces to a UV-space in 2D. Each 3D face is associated to 2D cylindrical parametrisation by a bijective mapping. Notice that establishing a dense correspondence between two UV images implicitly establishes a 3D-to-3D dense correspondence (due to the bijection). Paysan et al. [35] constructed the well-known Basel Face Model (BFM) by applying the nonrigid iterative closest point (NICP) algorithm [36] to compute these dense correspondences directly between 3D faces. The BFM was built also with 100 female and 100 male subjects between 8 and 62 years old, with an average of 24.97 years old. One technical improvement of the BFM with respect to the 3DMM of Blanz and Vetter is the scanner, which is able to capture the facial geometry with higher resolution and precision in shorter time.

Huber et al. [37] presented the Surrey Face Model (SFM). It was built from 169 subjects, very diverse both in age (see Figure 1) and in ethnicity (60% Caucasian, 20% Eastern Asian, 6% Black African and 14% of other ethnicities comprising South Asian, Arabic or Latin). The scans were put in dense correspondence using the iterative multi-resolution dense 3D registration method [38], which registers two 3D faces in three stages (global mapping, local matching, and energy minimisation) in a coarse-to-fine manner. To build the texture model, the 2D images captured by the camera system that generated the 3D scans were mapped to the registered 3D faces, obtaining in this way textured 3D faces. These textures were mapped back to 2D through a mapping that preserves the geodesic distances. The texture model was built from these resulting 2D representations.

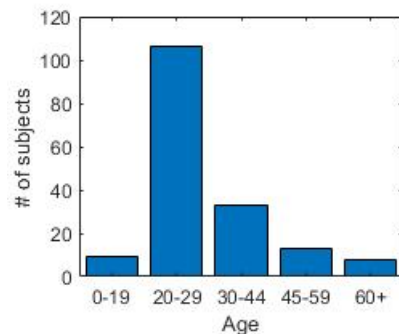


Figure 1: SFM dataset age distribution

Table 1: Characteristics of the available 3DMMs.

3DMM	#subjects	% Males	Age (years old)	Expression	Ethnicity
BlanzVetter 1999 [30]	200	50	“young adults”	×	–
BFM [35]	200	50	8-62	×	“most Europeans”
SFM [37]	169	–	Fig. 1	×	60% Caucasian
LSFM [39]	9663	48	Fig. 2	×	82% White
LYHM [40]	1212	50	Fig. 3	×	–
FaceWarehouse [41]	150	–	7-80	✓	“various”

Booth et al. [39] and Dai et al. [40] proposed fully automated pipelines to construct a 3DMM, both consisting mainly of an automatic detection of landmarks, the computation of a shared triangulation across all the meshes and the model construction. To locate a set of 3D landmarks in the facial meshes, Booth et al. [39] detected 2D landmarks various rendered 2D images from each mesh using a state-of-the-art landmark detector. These 2D landmarks were mapped to the 3D face by inverting the rendering. Then, dense correspondences were established by deforming a predefined template mesh to fit the facial shapes using the NICP algorithm. From an initial PCA model of all fittings, erroneous correspondences can be identified by the corresponding shape vectors that behave as outliers. The final model was then obtained by applying PCA on the training sets after excluding the outliers. With this pipeline, they presented the largest 3DMM until now, the Large Scale Facial Model (LSFM), built from 9,663 individuals covering a wide variety of ages (Figure 2), gender (48% male), and ethnicity (82% White, 9% Asian, 5% mixed heritage, 3% Black and 1% other ethnicities). The size of this dataset allowed the construction of smaller models from shapes of a specific age range and ethnicity.

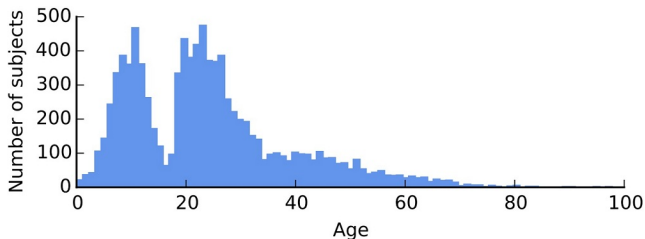


Figure 2: LSFM dataset age distribution (extracted from [39]).

The pipeline presented by Dai et al. [40] is similar to the one in [39]; however, rather than rendering images from the 3D scans to detect landmarks in 2D, Dai et al. [40] used the 2D image captured by the image system, like Huber et al. [37]. The dense correspondences were also established by deforming a 3D facial template to each facial shape, but instead of using NICP, they used an approach based on the coherent point drift algorithm [42] and refined the correspondences using optical flow for the tex-

ture channel. Finally, the facial model was built from the meshes in dense correspondence using PCA. They built a 3D model of the whole head, the Liverpool-York Head Model (LYHM), with 1,212 3D scans of subjects from a wide range of ages (Figure 3) and balanced in gender.

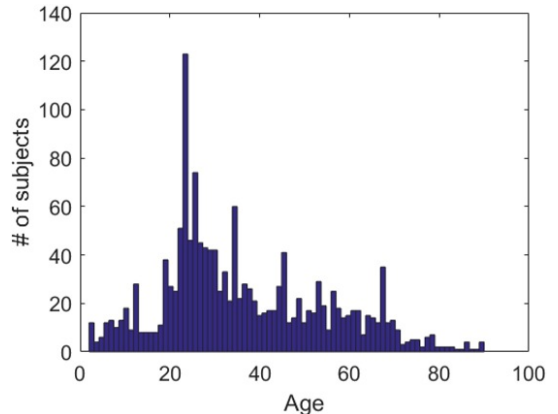


Figure 3: LYHM dataset age distribution (extracted from Dai et al. [40]).

In contrast to all the previous models, which capture geometric variations due to shape only, Cao et al. [41] constructed the FaceWarehouse model, a bilinear face model that includes also expression variations. They used a Kinect system to capture 20 expressions (one of them being the neutral) of 150 individuals aged between 7 and 80 years old. For each of the expressions, 74 landmarks were located on the 2D picture using active shape model [43]. These landmarks were then used to guide the fitting process of the Blanz and Vetter face model [30] to the depth map, in order to obtain meshes in correspondence. Individual-specific expression blendshapes were then generated from the meshes obtaining 47 expressions for each subject, which were used as the face database. To build the bilinear face model, they assembled all the vectorised meshes into a 3-rank data tensor (vertices \times identities \times expressions) and applied N-mode singular value decomposition to decompose it.

3. Statistical Model Fitting Methods

Using a statistical model as the representation of the prior knowledge of the 3D structure of a face allows for a reconstruction of a new 3D face from one or more photographs by finding the linear combination of the model bases that best fits to the given 2D image(s).

Essentially, fitting a 3D facial model to 2D images implies optimising a non-linear cost function. Other approaches have also been explored, such as the linearisation of the cost function or a probabilistic point of view.

In this section, we summarise and compare the most relevant proposed approaches to fit a 3D facial model to a one or more 2D images in the last decade. First, we overview the different inputs the community has been using, analysing their strengths and weaknesses (Section 3.1). Then, we review the three different approaches we have identified among the 3DMM fitting works: non-linear optimisation of a cost function (Section 3.2), linear approaches (Section 3.3), and probabilistic approaches (Section 3.4). Finally, in Section 3.5, we explain how some researchers have proposed to fit a 3DMM in a local manner by dividing the face into subregions. The reviewed proposals are compiled in Tables 2 and 3, and main conclusions are summarised in Section 3.6.

3.1. Input types

Reconstructing the 3D facial geometry and appearance of a person from a single in-the-wild picture is much more challenging than using multiple images. This is why most works have mainly focused on 3D face reconstruction from a single image. Even so, some researchers have considered multiple images to improve the reconstruction accuracy by observing the subject’s face under different poses and illumination conditions. In the same line, others have proposed to use 2D video sequences as a simple way of obtaining a set of pictures from the same person. However, when using a video, the temporal relation between frames has to be taken into account when reconstructing the 3D facial shape.

On the other hand, landmark locations and simple image features, such as raw pixel values and texture edges, are the most used features to estimate the 3DMM parameters. Nonetheless, some researchers have proposed to extract complex features from the input image, which are considered to be more robust against changes in imaging conditions.

3.1.1. Multiple images methods

Piotraschke and Blanz [57] took advantage of the multiple input images to reconstruct a single 3D face by combining the 3D faces that resulted from applying a single-image method to each of the input images. In contrast, [31, 51, 49, 59, 66, 67] estimated the parameters from all the input images at the same time by minimising a cost function that is the sum of the cost function applied to each of the images: $\mathbb{E}(\theta) = \sum_{j=1}^P \mathbb{E}_j(\theta_j)$, where

some of the parameters θ_j are shared across all the images (such as the shape parameters) and some are not (such as the projection parameters or the illumination). Jin et al. [31], Sariyanidi et al. [66] used that technique to fit the 3DMM to a set of independent images, whereas [51, 49, 59, 67] used videos but considering the set of frames as separate images.

Booth et al. [17], extending their work from [62], added a fitting procedure to videos. However, since a video provides more information than multiple independent images, they added a term to the cost function that ensures temporal smoothness of the parameters, i.e., regularity across consecutive frames. Garrido et al. [58] also proposed a technique to fit the 3D facial model to videos but in an iterative manner by optimising the parameters for each of the frames.

Contrary to all the above approaches, Hernandez et al. [61] proposed to estimate the model parameters for each frame of a video sequence by imposing photo-consistency between consecutive frames. However, unlike Booth et al. [17], they minimised a local representation \mathcal{F} around the projection over consecutive frames, t and $t + 1$, of the 3D vertices, $i = 1, \dots, N$ of the estimated 3D faces for each frame, $\mathbf{x}^t = \mathbf{x}(\alpha^t)$ and $\mathbf{x}^{t+1} = \mathbf{x}(\alpha^{t+1})$:

$$\mathbb{E} = \sum_t \sum_{i=1}^N \|\mathcal{F}(\mathcal{P}(\mathbf{x}_i^t, \zeta^t)) - \mathcal{F}(\mathcal{P}(\mathbf{x}_i^{t+1}, \zeta^{t+1}))\|_2^2,$$

where \mathbf{x}_i^t represents the i th vertex of \mathbf{x}^t , $\mathcal{P}(\mathbf{x}_i^t, \zeta^t)$ is the projection of the vertex \mathbf{x}_i^t according to the projection parameters of frame t , ζ^t , and \mathcal{F} is the local feature extraction function (image colour, image intensity, complex image features, etc.).

3.1.2. Image features

Booth et al. [62, 17] used image features to construct a texture model that was later employed to recover the facial appearance, whereas Huber et al. [53], Zhu et al. [55], Hernandez et al. [61] and Gecer et al. [64] used them in the reconstruction process.

Gecer et al. [64] extracted identity features from the input and rendered images using a pre-trained face recognition networks and used them to compute the difference between both images.

On the other hand, Hernandez et al. [61], Huber et al. [53], and Zhu et al. [54] extracted image features from patches of the input image \mathbf{I}_m around the projections of 3D vertices from the reconstruction into the image plane. Unlike the first authors [61] who projected all the vertices in the 3D facial mesh, [53, 54] only extracted features around the projected the 3D-landmarks $\hat{\ell}^{2D}$.

Huber et al. [53] and Zhu et al. [55] also proposed to include complex image features (e.g. SIFT or HOG) in the fitting process, but their approach differed from [62, 17] in many ways. They trained a cascaded regressor that jointly optimised the camera ζ and the shape α

Table 2: 3D-from-2D face reconstruction approaches based on 3DMM fitting - part I.

Reference	Images	Features used to fit	Fitting			
			Camera parameters	Shape	Texture	Illumination model
Aldrian and Smith [44]	Single	Landmarks	Linear	Maximise posterior	Colour channels ratios	Lambertian
Aldrian and Smith [45]	Single	Landmarks	Linear	Maximise posterior	Minimise error	Lambertian + specular
Aldrian and Smith [46]	Single	Landmarks	Linear	Maximise posterior	Minimise error	Lambertian + specular
Aldrian and Smith [47]	Single	Landmarks	Linear	Maximise posterior	Minimise error	Lambertian + specular
Schönborn et al. [48]	Single	Render image, landmarks	Minimise error	Maximise posterior	Maximise posterior	Spherical harmonics
Shi et al. [49]	Video	Landmarks	Minimise error	Minimise error	–	–
Ding et al. [50]	Single	Landmarks	Linear	Maximise posterior	–	–
Qu et al. [51]	Multiple	Landmarks	Minimise error	Minimise error	–	–
Qu et al. [52]	Single	Landmarks	Minimise error	Minimise error	–	–
Huber et al. [53]	Single	Features around landmarks	Cascaded regression	Cascaded regression	–	–
Zhu et al. [54]	Single	Landmarks	Minimise error	Minimise error	–	–
Zhu et al. [55]	Single	Features around landmarks	Cascaded regression	Cascaded regression	–	–
Bas et al. [56]	Single	Landmarks, texture edges	Minimise error	Minimise error	–	–
Piotraschke and Blanz [57]	Multiple	Render image, landmarks	Minimise error	Minimise error	Minimise error	Phong
Garrido et al. [58]	Video	Render image, landmarks	Minimise error	Minimise error	Minimise error	Lambertian
Thies et al. [59]	Single, video	Render image, landmarks	Minimise error	Minimise error	Minimise error	Lambertian
Hu et al. [60]	Single	Render image, landmarks	Minimise error	Minimise error	Minimise error	Phong
Hernandez et al. [61]	Video	Image features around projected 3D vertices	Minimise error	Minimise error	–	–
Booth et al. [62]	Single	Render image, landmarks	Minimise error	Minimise error	Minimise error	Image features
Jin et al. [31]	Two	Render image, landmarks	Regression model	Minimise error	Minimise error	Phong
Booth et al. [17]	Single, video	Render image, landmarks	Minimise error	Minimise error	Minimise error	Image features

Table 3: 3D-from-2D face reconstruction approaches based on 3DMM fitting - part II.

Reference	Images	Features used to fit	Fitting			
			Camera parameters	Shape	Texture	Illumination model
Jiang et al. [63]	Single	Render image, landmarks	Minimise error	Minimise error	Minimise error	Lambertian
Gecer et al. [64]	Single	Render image, landmarks & image features	Minimise error	Minimise error	Minimise error	Phong
Liu et al. [65]	Single	Landmarks	Minimise error	Minimise error	–	–
Sariyanidi et al. [66]	Mutliple	Render image, landmarks	Minimise error	Minimise error	Minimise error	Phong
Koujan and Roussos [67]	Mutliple	Subset of 3D vertices	Minimise error	Minimise error	–	–

parameters given an initial feature vector, thereby avoiding the optimisation of a non-linear cost function. These feature vectors were SIFT features extracted from patches of the input image \mathbf{I}_{in} around the projections of the 3D-landmarks into the image plane $\hat{\ell}^{2\text{D}}$. Hence, at each step t , given the parameters $\theta_t = \{\zeta_t, \alpha_t\}$ estimated by the previous weak regressor \mathcal{R}_{t-1} , the 3D-landmarks in $\mathbf{x}(\alpha_t)$, $\{\ell_i^{3\text{D}}(\alpha_t)\}_{i=1}^L$, were projected into the input image plane $\mathcal{P}(\ell_i^{3\text{D}}(\alpha_t), \zeta_t) = \hat{\ell}_i^{2\text{D}}(\alpha_t)$, and image features were extracted from patches of \mathbf{I}_{in} centred at $\hat{\ell}_i^{2\text{D}}(\alpha_t)$, $\{\mathbf{f}_t^i = \mathbf{f}(\theta_t, \hat{\ell}_i^{2\text{D}}(\alpha_t))\}_{i=1}^L$. Each weak regressor \mathcal{R}_t inputted a vector of features $\mathbf{f}_t = [\mathbf{f}_t^1, \dots, \mathbf{f}_t^L]$ and outputted an optimal parameter update $\Delta\theta_t$ such that $\theta_{t+1} = \theta_t + \Delta\theta_t$.

3.2. Non-linear optimisation of a cost function

Blanz and Vetter [30] not only introduced the 3DMMs to the community but also proposed a method to fit them to a single facial image, indicating a way of extending it to many images that inspired many others. Their fitting process was based on a simple idea: if the input image and the image rendered from the fitted 3D face are similar, the 3D reconstruction is faithful to the input image. In an iterative manner, using the stochastic gradient descent method, they optimised the shape α and the albedo β parameters alongside with a set of rendering parameters ρ (including intrinsic camera parameters, projection parameters as well as illumination parameters) such that they produced an image \mathbf{I}_{mod} as close as possible to the input \mathbf{I}_{in} ; i.e., they minimised the sum of the Euclidean distance between each pixel (x, y) of the input and the reconstructed images:

$$\mathbb{E}_{\mathbf{I}}(\alpha, \beta, \rho) = \sum_{x,y} \|\mathbf{I}_{\text{in}}(x, y) - \mathbf{I}_{\text{mod}}(x, y)\|_2^2. \quad (4)$$

\mathbf{I}_{mod} was rendered using the Phong reflectance model [68]

and a perspective projection defined by $\mathcal{P}_{\text{PP}} : \mathbb{R}^3 \rightarrow \mathbb{R}^2$

$$\mathcal{P}_{\text{PP}}(\mathbf{v}, \zeta) = \frac{f}{v'_z} \begin{pmatrix} v'_x \\ v'_y \end{pmatrix} + \begin{pmatrix} o_x \\ o_y \end{pmatrix} \quad (5)$$

where $\begin{pmatrix} v'_x \\ v'_y \\ v'_z \end{pmatrix} = \mathbf{R}\mathbf{v} + \tau$

for a point $\mathbf{v} \in \mathbb{R}^3$. The projection parameters $\zeta = \{\mathbf{R}, \tau, f, \mathbf{o}\}$ include the rotation matrix \mathbf{R} and the translation τ of the face, the focal length f and the coordinates of the optical axis in the image plane $\mathbf{o} = (o_x, o_y)^T$.

However, only by minimising the distance between the input and the rendered images, a face-like surface is not guaranteed since the minimisation is ill-posed. To solve this issue, Blanz and Vetter added to the cost function a regularisation term for the parameters using the prior probabilities of the model coefficients (see eq. (3)) and an ad-hoc prior for the rendering coefficients:

$$\mathbb{E}_{\text{reg}}(\alpha, \beta, \rho) = \sum_{i=1}^{\tilde{M}-1} \frac{\alpha_i^2}{\sigma_{\alpha_i}^2} + \sum_{i=1}^{\tilde{N}-1} \frac{\beta_i^2}{\sigma_{\beta_i}^2} + \sum_j \frac{(\rho_j - \bar{\rho}_j)^2}{\sigma_{\rho_j}^2}.$$

Later, in [69], they extended their work by adding to the cost function a term that enforces a fixed set of facial feature points (landmarks) in the reconstructed facial shape, $\ell_i^{3\text{D}}$ ($i = 1, \dots, L$), to be such that their projections, $\hat{\ell}_i^{2\text{D}}$, lie over the corresponding set of manually annotated landmarks in the input image, $\ell_i^{2\text{D}}$,

$$\mathbb{E}_{\text{lmk2D}}(\zeta) = \sum_{i=1}^L \left\| \ell_i^{2\text{D}} - \hat{\ell}_i^{2\text{D}} \right\|_2^2. \quad (6)$$

This 3DMM fitting approach based on the minimisation of the distance between the input and the rendered image has been followed by many others [49, 51, 52, 54, 57, 31, 59, 56, 58, 61, 60, 62, 17, 63, 65, 66].

Piotraschke and Blanz [57] used Blanz and Vetter's approach [69], adding an automatic landmark detector to ex-

tract the facial points in the input image, thus obtaining a fully automatic system. Whereas, Thies et al. [59] used [69] for face reenactment by fitting a 3DMM to the source and the target subjects and transferring to the target subject the estimated expression of the source subject.

Hernandez et al. [61], Qu et al. [52], Liu et al. [65] and Zhu et al. [54] proposed to use only one of the error terms used by Blanz and Vetter [69]. Whereas Hernandez et al. [61] focused on ensuring photometric consistency, Qu et al. [52], Liu et al. [65] and Zhu et al. [54] used only the landmark term (eq. (6)), including to the set of the facial landmarks, the contour landmarks. Qu et al. [52] separated the in-face and the contour landmarks in two terms. Since the contour landmarks are not well defined in non-frontal poses, treating contour landmarks separately allowed them to define the 2D contour landmark in a softer manner: a 2D contour landmark corresponding to a 3D contour landmark is the nearest landmark in the image to the projection of the 3D landmark. Similarly, Liu et al. [65] iteratively updated the 2D contour landmarks while estimating the shape and projection parameters. This update consisted in taking as new landmarks the nearest points on the 2D contour line to the projected 3D contour landmarks. In this way, the contour landmarks' correspondence is improved, helping to better estimate the 3D face. In contrast, Zhu et al. [54] jointly estimated the 3DMM parameters, the projection parameters and the position of 3D landmarks on the 3DMM given the 2D landmarks on the image. They observed that the pose parameters and the landmarks depended on each other; thus, they proposed to iteratively estimate first the shape and pose parameters and then update the landmarks position.

Koujan and Roussos [67] also used only a set of corresponding 3D-2D points to fit the 3DMM to images but, contrary to [52, 65, 54], they obtained a dense set of points. They used a video sequence to estimate the 3D facial geometry of a person by first computing optical flow from a reference frame to all the rest, and then finding correspondences between the set of moving 2D points identified by the optical flow algorithm and the 3D vertices of the facial shape, which was previously initialised using only landmarks.

Sariyanidi et al. [66], Booth et al. [62, 17], and Gecer et al. [64] completely redefined the image error, $\mathbb{E}_{\mathbf{I}}$. The first authors defined the image error as the gradient correlation [70] between the input and the rendered images, $\mathbb{E}_{\mathbf{I}} = \nabla \mathbf{I}_{\text{in}}^{\top} \nabla \mathbf{I}_{\text{mod}}$, which they claimed is more robust against illumination variations and occlusions. The gradients $\nabla \mathbf{I}_{*}$ are computed as the concatenation of the magnitude-normalised differences along the vertical and horizontal axes for each of the K pixels. However, their main contribution is a regularisation of the model parameters based on adding inequality constraints to the minimisation problem, whose upper and lower bounds are extracted from the 3DMM. The authors argued that adding a regularisation term to the cost function (see eq. (3.2)) may lead to unsatisfying results, either because of a too smoothed 3D face or

the opposite, since the weight of the regularisation on the minimisation problem is controlled by a parameter that is chosen ad-hoc.

Booth et al. [62, 17] proposed a texture model constructed from a dense feature-based representation of in-the-wild images. Instead of using the per-pixel RGB values of the 3D face, the training samples used to build the texture model (see eq. (2)) were image feature vectors, \mathbf{f}_i . These were obtained by applying a dense feature extraction function to each of the in-the-wild images in the training set. Then, assuming known shape parameters α (thus, known 3D facial shape, $\mathbf{x}(\alpha)$) and projection parameters ζ for each training image, they computed the projection of the 3D faces $\mathbf{x}(\alpha)$ according to ζ into the image plane $\mathcal{P}(\mathbf{x}(\alpha), \zeta)$, and sampled the feature vectors on the location of the projection of the 3D faces. Therefore, for each training image, they obtained a vector \mathbf{f}_i composed of the features vectors on the location of the corresponding projected 3D face. Then, the image error $\mathbb{E}_{\mathbf{I}}$ was redefined as

$$\mathbb{E}_{\mathbf{I}}(\alpha, \beta, \zeta) = \|\mathbf{F}(\mathcal{P}(\mathbf{x}(\alpha), \zeta)) - \mathbf{f}(\beta)\|_2^2, \quad (7)$$

where \mathbf{F} is the function that extracts the features from the pixels in the input image corresponding to the location of the projected reconstructed 3D face $\mathcal{P}(\mathbf{x}(\alpha), \zeta)$, and $\mathbf{f}(\beta)$ is the instance of the feature-based texture model corresponding to the parameters β .

With a similar idea, Gecer et al. [64] used a perceptual loss that minimised the cosine distance of image features extracted from \mathbf{I}_{in} and \mathbf{I}_{mod} using the ArcFace network [71]. They also minimised the Euclidean distance between features from intermediate layers, together with the image error (eq. (4)) and a landmarks error, to estimate the shape, expression, and texture 3DMM parameters, and the rendering parameters. Differently from the other works, Gecer et al. [64] trained a generative adversarial network to estimate a refined texture UV-map from the texture parameters estimated by minimising the cost function.

The works studied above [62, 17, 61, 57, 52, 59, 64] jointly optimised the shape, texture, and projection parameters by minimising a single cost function. However, other approaches [58, 60, 63, 31, 49, 51] proposed to reconstruct the 3D facial shape by minimising a cost function in different stages.

Some researchers [58, 31, 51, 49] proposed to estimate the 3D face in stages where each one estimated finer details than the previous one. Qu et al. [51] fitted the 3D facial model only by minimising the landmarks error, first using a single image and then including multiple images to refine the previous reconstruction.

Jin et al. [31] divided the fitting process into a coarse and a fine-scale stage, estimating in a prior step the projection parameters using a regression model. In the global fitting stage, they minimised the distance between the 2D-landmarks and the projections of the 3D-landmarks into the image, as in eq. (6). Then, in the detail fitting stage,

they minimised the difference between the input image and the rendered image, as in eq. (4), adding a term that enforced the model parameters in the detail fitting stage to be similar to the parameters estimated in the global fitting stage. Similarly, Shi et al. [49] estimated in the global stage the shape and expression model parameters together with the projection parameters. They also used the image error to refine the coarse 3D face; however, unlike [31] who assumed a Phong reflectance model, they adopted a Lambertian reflectance model and regularised the parameters by minimising the difference to reference parameters, where the reference surface normals were extracted from the coarse 3D shape and the reference albedo from the FaceWarehouse [41].

Garrido et al. [58] also used the coarse-to-fine framework to estimate the facial geometry. In a coarse-scale stage, they optimised all the parameters by minimising a cost function with an image distance term $\mathbb{E}_{\mathbf{I}}$, a landmark distance term $\mathbb{E}_{\text{lmk2D}}$, and a regularisation term \mathbb{E}_{reg} . In the medium-scale stage, all the parameters were fixed except the projection parameters, which were reestimated together with a 3D deformation field by minimising again the same cost function but deforming the reconstructed shape according to the estimated deformation field. Finally, the fine-scale deformation field was estimated by inverse rendering optimisation such that the synthesised shading gradients matched the gradients of the illumination in the corresponding input image as good as possible.

Hu et al. [60] and Jiang et al. [63] also minimised a non-linear error function at different stages. Unlike [58, 31, 51, 49], who estimated in each stage more subtle details than the previous one, [60, 63] split the 3D facial reconstruction process into the estimation of the facial geometry of the subject and the estimation of the appearance, including the illumination.

Different from [60] who clearly separated the geometric and the photometric stages, Jiang et al. [63] refined in the photometric stage the reconstruction resulting from the geometric stage, while estimating the appearance. In the geometric stage, they minimised the distance between the 2D landmarks and the projection of the 3D landmarks, estimating the projection, shape and expression parameters. In the photometric stage, a Lambertian reflectance model was assumed and approximated using spherical harmonic functions. First, the albedo and illumination parameters were estimated by minimising the image error $\mathbb{E}_{\mathbf{I}}$ (eq. (4)) using the shape estimated in the geometric stage. Then, a vertex displacement was allowed and estimated by minimising again the image error using the already estimated albedo and illumination parameters. Finally, fine geometric details were recovered using a shape-from-shading method that reestimated the surface normals by minimising the difference in intensity gradients between the input image and the rendered image.

In the work by Hu et al. [60], both stages are iterated in turn a few times to refine the solution. The geometric phase is composed of three steps: in the first step the

projection parameters ζ are estimated by minimising the distance between the projection of the 3D-landmarks and the 2D-landmarks, $\mathbb{E}_{\text{lmk2D}}$ (eq. (6)); in the second step the shape parameters α are estimated by minimising the distance between 3D-landmarks in the model $\ell^{3\text{D}}$ and the back-projected 2D-landmarks $\hat{\ell}^{3\text{D}}$ to the model using the already estimated projection parameters:

$$\mathbb{E}_{\text{lmk3D}}(\alpha) = \sum_{i=1}^L \left\| \ell_i^{3\text{D}} - \hat{\ell}_i^{3\text{D}} \right\|_2^2.$$

In the last step of the geometric stage, they detected contour facial points in the input and the rendered images, and added these points to the set of landmarks used in the previous steps (the estimation of the camera and the shape parameters) to refine the solution.

The second stage is also divided in three steps where the light direction, the light intensity and the texture parameters are estimated assuming the Phong model as a reflectance model of the facial surface. First, the light direction is estimated by minimising the image distance $\mathbb{E}_{\mathbf{I}}$ (eq. (4)) and taking all the other variables as constants. The estimated light direction is fed to the next step where the light intensity is computed again by minimising the image distance. The same procedure is used to estimate the texture parameters.

One notable contribution of Hu et al. [60] with respect to the previous approaches is that they linearised all the error functions except the one that estimates the projection parameters (i.e. the ones used to estimate the shape, light direction, light intensity, and texture parameters). This linearisation resulted on closed-form solutions, which they claimed increases the computational efficiency.

This idea of linearising the cost function was also exploited by Bas et al. [56] who again divided the 3D face reconstruction in two parts: the estimation of the shape and projection parameters in a linear manner (with closed-form solutions) and a non-linear refinement of the estimated shape. Unlike [60], they linearised the estimation of the projection parameters. Rather than a perspective projection (see eq. (5)), they considered a scaled orthographic projection. The scaled orthographic projection model assumes that the variation in depth is small relative to the distance from the camera. Under these assumptions, the projection of $\mathbf{v} \in \mathbb{R}^3$ only depends on a uniform scale factor $s \in \mathbb{R}$. Thus, for a set of projection parameters $\zeta = \{\mathbf{R}, \tau, s\}$:

$$\mathcal{P}_{\text{SOP}}(\mathbf{v}, \zeta) = s \begin{pmatrix} 1 & 0 & 0 \\ 0 & 1 & 0 \end{pmatrix} \mathbf{R}\mathbf{v} + s\tau. \quad (8)$$

With this projection model, the projection parameters, which are estimated by minimising the landmarks distance $\mathbb{E}_{\text{lmk2D}}$ (eq.(6)), are obtained in a linear manner using the POS algorithm [72]. Likewise, since the landmarks in the 3D model $\ell^{3\text{D}}$ depend on the shape parameters α , matching their projections $\hat{\ell}^{2\text{D}}$ by eq. (8) to the landmarks

in the input image ℓ^{2D} , they obtained a linear system of equations for α , $A\alpha = \mathbf{b}$. These initial estimations of ζ and α are refined by including texture edges to the fitting procedure, minimising a non-linear cost function with a landmark distance term $\mathbb{E}_{\text{lmk}2D}$, a regularisation term \mathbb{E}_{reg} , and an edge distance term \mathbb{E}_{edge} defined as

$$\mathbb{E}_{\text{edge}} = \frac{1}{|\mathcal{B}_{3D}|} \sum_{\mathbf{v} \in \mathcal{B}_{3D}} \min_{\mathbf{p} \in \mathcal{B}_{2D}} \|\mathbf{p} - \mathcal{P}_{\text{SOP}}(\mathbf{v}, \zeta)\|_2^2,$$

where \mathcal{B}_{2D} is the set of pixels in the input image detected as texture edges, \mathcal{B}_{3D} is the occluding boundary of the 3D face, defined as the set of vertices that lie on a mesh edge whose adjacent mesh faces have a change of visibility, and $|\mathcal{B}_{3D}|$ indicates the size of \mathcal{B}_{3D} .

3.3. Linear approaches

All the previously mentioned works exploit the optimisation of a non-linear error function very similarly to the approach presented originally by Blanz and Vetter [30, 69]. However, Aldrian and Smith [44] observed that the optimisation problem proposed by Blanz and Vetter [69] (and followed by many others) is highly complex, computationally expensive and prone to be stuck on local minima due to its ill-posed nature. To avoid that, they proposed an alternative: to fit the 3DMM in a linear manner, separately for the projection parameters, the facial geometry and the texture. Unlike [56], who refined in a non-linear manner the reconstruction resulting from the linear stage, Aldrian and Smith [44] proposed a completely linear approach that was later further explored [46, 45, 47, 50].

Aldrian and Smith [44] proposed to estimate a camera projection matrix \mathbf{C} such that the projection of the 3D-landmarks matches the 2D-landmarks, i.e., ideally $\ell_i^{2D} = \hat{\ell}_i^{2D}$ where $\hat{\ell}_i^{2D} = \mathcal{P}(\ell_i^{3D}, \mathbf{C}) = \mathbf{C}\ell_i^{3D}$, $\forall i = 1, \dots, L$. That is, \mathbf{C} is such that the landmark distance $\mathbb{E}_{\text{lmk}2D}$ is minimised

$$\begin{aligned} \mathbb{E}_{\text{lmk}2D}(\mathbf{C}) &= \sum_{i=1}^L \left\| \ell_i^{2D} - \hat{\ell}_i^{2D} \right\|_2^2 \\ &= \sum_{i=1}^L \left\| \ell_i^{2D} - \mathbf{C}\ell_i^{3D} \right\|_2^2. \end{aligned}$$

They solved this minimisation problem using the Gold Standard algorithm [73], which constructs a linear system of equations by assuming an affine camera model.

Then, they estimated the shape model parameters by maximising the posterior probability over the shape parameters α given the set of 2D-landmarks in the image $\mathcal{L}^{2D} = \{\ell_1^{2D}, \dots, \ell_L^{2D}\}$, i.e. maximising $p(\alpha | \mathcal{L}^{2D})$. By applying the Bayes' theorem, maximising the posterior probability is equivalent to maximising $p(\mathcal{L}^{2D} | \alpha)p(\alpha)$, where $p(\alpha)$ is known from the 3DMM (see eq. (3)) and $\mathcal{L}^{2D} | \alpha \sim \mathcal{N}(\hat{\mathcal{L}}^{2D} | \sigma_{2D}^2)$, where $\hat{\mathcal{L}}^{2D}$ is the projection of the 3D-landmarks and σ_{2D}^2 the variances of the 2D-landmarks. These variances are estimated ad-hoc from the projection of the 3D landmarks of a set of new faces generated with the model. The posterior probability is then differentiated,

which leads to a linear system of equations, and solved for the shape parameters. Once the camera and the shape parameters are computed, the texture is estimated by assuming a white illumination and a Lambertian reflectance model (diffuse-only reflectance), and the estimation is based on the observation that ratios between pairs of colour channels in the input image are functions only of the ratio of texture in the corresponding vertices of the 3D face. Thus, each pixel i in the facial region of \mathbf{I}_{in} has a corresponding vertex in the 3D face whose RGB colours are defined by $\bar{\mathbf{c}}_{[R(i), G(i), B(i)]} + \Psi_{[R(i), G(i), B(i)]}\beta$, then

$$\frac{\bar{c}_{R(i)} + \Psi_{R(i)}\beta}{\bar{c}_{G(i)} + \Psi_{G(i)}\beta} = \frac{\mathbf{I}_{\text{in}}^{R(i)}}{\mathbf{I}_{\text{in}}^{G(i)}}$$

and

$$\frac{\bar{c}_{G(i)} + \Psi_{G(i)}\beta}{\bar{c}_{B(i)} + \Psi_{B(i)}\beta} = \frac{\mathbf{I}_{\text{in}}^{G(i)}}{\mathbf{I}_{\text{in}}^{B(i)}},$$

where $(\mathbf{I}_{\text{in}}^{R(i)}, \mathbf{I}_{\text{in}}^{G(i)}, \mathbf{I}_{\text{in}}^{B(i)})$ are the RGB colours of the pixel i in the image \mathbf{I}_{in} . For a set of pixel-vertex correspondences, they constructed a linear system of equations by imposing R-G and G-B ratios that is solved for the texture model parameters.

In their following works [46, 45, 47], Aldrian and Smith imposed less restrictive assumptions on the illumination model of the face. Whereas in [44] they assumed a Lambertian reflectance model (diffuse-only), thereafter they adopted a Phong reflectance model, which comprises additive diffuse and specular terms. In [46, 45] they proposed different approaches to estimate the texture and illumination parameters, which are later summarised in [47].

In [46], they proposed to use an specular-invariant representation of the texture to estimate the diffuse reflectance assuming that all light sources have the same fixed known colour. This specular-invariant representation is the SUV colour space [74], which is a rotation of the RGB colour space such that one of the axes is aligned with the direction of the colour of the light source. More precisely, assuming a dichromatic light model, the input image \mathbf{I}_{in} is a linear combination of the diffuse colour \mathbf{I}_d and the specular colour \mathbf{I}_s , i.e. $\mathbf{I}_{\text{in}} = \lambda_d \mathbf{I}_d + \lambda_s \mathbf{I}_s$. Thus, the SUV representation of an RGB image is $\mathbf{I}^{\text{SUV}} = \mathbf{R}\mathbf{I}^{\text{RGB}} = \mathbf{R}(\lambda_d \mathbf{I}_d + \lambda_s \mathbf{I}_s) = \lambda_d \mathbf{R}\mathbf{I}_d + \lambda_s \mathbf{R}\mathbf{I}_s$, where \mathbf{R} is the rotation matrix. Since \mathbf{R} aligns one channel (S in this case) with the colour of the light source, the specular colour, \mathbf{I}_s , then $\mathbf{R}\mathbf{I}_s = (1, 0, 0)^T = \mathbf{I}^S$. Thus, the representation of \mathbf{I}^{RGB} in the SUV colour space is only defined by the intensities of the remaining colour channels U and V: $\mathbf{I}^U = \mathbf{r}_2^T \mathbf{I}^{\text{RGB}} = \lambda_d \mathbf{r}_2^T \mathbf{I}_d$ and $\mathbf{I}^V = \mathbf{r}_3^T \mathbf{I}^{\text{RGB}} = \lambda_d \mathbf{r}_3^T \mathbf{I}_d$, where \mathbf{r}_2^T and \mathbf{r}_3^T are the second and third row of the rotation matrix \mathbf{R} .

Besides, they modelled both the diffuse and the specular reflectance with spherical harmonics basis functions. However, to model the specular part, they used functions constructed from the spherical harmonics but reflecting

the normals about the viewing direction. Thus, the rendered image is constructed as

$$\mathbf{I}_{\text{mod}} = \mathcal{I} * (\mathcal{D}\gamma_{\text{d}} * (\bar{\mathbf{c}} + \Psi\beta) + \mathcal{S}\gamma_{\text{s}})$$

where \mathcal{I} denotes the colour of the light source, γ_{d} and γ_{s} are the diffuse and specular lighting parameters, and \mathcal{D} and \mathcal{S} the respective spherical harmonics basis functions. The symbol $*$ denotes the element-wise multiplication.

With this image-formation model, they first estimated the diffuse light parameters γ_{d} and the texture parameters β in the SUV space by minimising $\mathbb{E}(\gamma_{\text{d}}, \beta) = \mathbb{E}_{\text{U}}(\gamma_{\text{d}}, \beta) + \mathbb{E}_{\text{V}}(\gamma_{\text{d}}, \beta)$, where

$$\begin{aligned} \mathbb{E}_{\text{U}} &= \sum_{k=1}^K \left[(\mathbf{I}_{\text{in}})_{\text{k}}^{\text{U}} - (\mathbf{I}_{\text{mod}})_{\text{k}}^{\text{U}} \right]^2 \\ &= \sum_{k=1}^K \left[\mathbf{r}_2^{\text{T}}(\mathbf{I}_{\text{in},\text{d}})_{\text{k}} - \mathbf{r}_2^{\text{T}}(\mathbf{I}_{\text{mod},\text{d}})_{\text{k}} \right]^2 \\ &= \sum_{k=1}^K \left[\mathbf{r}_2^{\text{T}}(\mathbf{I}_{\text{in},\text{d}})_{\text{k}} - \mathbf{r}_2^{\text{T}}(\mathcal{I}_{\text{k}} * \mathcal{D}_{\text{k}}\gamma_{\text{d}} * (\bar{\mathbf{c}}_{\text{k}} + \Psi_{\text{k}}\beta)) \right]^2 \end{aligned}$$

(and \mathbb{E}_{V} is defined analogously) for K intensity observations. This error function is minimised by setting to zero the partial derivatives, which leads to a linear system of equations that is solved for the texture model parameters β and the diffuse light parameters γ_{d} . To estimate the specular reflectance parameters γ_{s} , they considered separately the low and the high frequencies (low and high order spherical harmonics) so that $\mathbf{I}_{\text{s}} = \mathbf{I}_{\text{s},\text{l}} + \mathbf{I}_{\text{s},\text{h}}$. For the low order frequencies, they used the illumination environment computed in the diffuse fitting stage (γ_{d} and β). Thus, specular reflectance parameters γ_{s} are computed considering the specular-only image, which is computed as the difference between the corrected image and the diffuse-only image

$$\mathbf{I}_{\text{s}} = \mathbf{I}_{\text{in}} - \mathcal{I} * \mathcal{D}\gamma_{\text{d}} * (\bar{\mathbf{c}} + \Psi\beta) = \mathcal{I} * \mathcal{S}\gamma_{\text{s}}. \quad (9)$$

Therefore, for known γ_{d} and β , eq. (9) is a linear system of equations. For higher orders, given that lighting is unknown, they solved the unconstrained problem using least-squares.

In [45], Aldrian and Smith relaxed further the assumptions and considered an unconstrained illumination, avoiding the premise of a common, known and fixed colour for all the light sources, but assuming non-specular reflectance to estimate the diffuse part. As in [46], they modelled the illumination using spherical harmonics basis functions. However, the rendered image \mathbf{I}_{mod} is constructed slightly different since an unconstrained illumination is assumed,

$$\mathbf{I}_{\text{mod}} = \mathcal{D}\gamma_{\text{d}} * (\bar{\mathbf{c}} + \Psi\beta) + \mathcal{S}\gamma_{\text{s}}.$$

They also considered the colour response of the camera in the model by adding a colour transformation and an offset, which are determined using the mean texture as initialisation to correct the input image. Then, they estimated the diffuse reflectance parameters γ_{d} and the texture pa-

rameters β by ignoring the specular part and minimising the difference between the corrected image $\tilde{\mathbf{I}}_{\text{in}}$ and the rendered image $\mathcal{D}\gamma_{\text{d}} * (\bar{\mathbf{c}} + \Psi\beta)$, with some regularisation terms on the parameters. The specular reflectance parameters γ_{s} are estimated in the same way as in [46] with the equivalent specular-only image

$$\mathbf{I}_{\text{s}} = \tilde{\mathbf{I}}_{\text{in}} - \mathcal{D}\gamma_{\text{d}} * (\bar{\mathbf{c}} + \Psi\beta) = \mathcal{S}\gamma_{\text{s}}.$$

Although Aldrian and Smith proposed different strategies to reconstruct the texture [44, 46, 45, 47], the suggested approach to estimate the 3D facial geometry remains unchanged throughout their works. Ding et al. [50] considered that Aldrian and Smith’s approach has two main drawbacks: first, in the camera projection matrix estimation, they do not take into account the orthonormal nature of the rotation matrix, and second, estimating the camera and the shape parameters separately, in a two-step manner, does not guarantee to decrease the cost function in each step. To solve the first drawback, they proposed to rescale and orthogonalise the camera projection matrix resulting from Aldrian and Smith’s algorithm to enforce orthonormality of the rotation matrix. The second disadvantage was solved by jointly estimating the camera projection matrix and the shape parameters using the Levenberg-Marquardt algorithm.

3.4. Probabilistic approach

A very different approach for fitting a 3DMM was proposed by Schönborn et al. [48] where they reformulated the process of fitting a 3DMM as a probabilistic inference problem, drawing samples from the posterior distribution over the set of all the parameters θ - containing the 3DMM’s parameters (shape α and texture β), the illumination and the projection parameters ζ - given the input image \mathbf{I}_{in} , $p(\theta|\mathbf{I}_{\text{in}})$. Although the use of the posterior probability was also exploited by others [44, 46, 45, 47, 50], Schönborn et al. [48] reinterpreted the model fitting procedure. They used the Metropolis-Hastings algorithm to draw samples of the parameters θ distributed according the posterior distribution $p(\theta|\mathbf{I}_{\text{in}})$ by stochastically accepting or rejecting samples. Such posterior distribution was computed by applying the Bayes’ theorem, $p(\theta|\mathbf{I}_{\text{in}}) \propto p(\mathbf{I}_{\text{in}}|\theta)p(\theta)$. The first term, $p(\mathbf{I}_{\text{in}}|\theta)$, is a Gaussian distribution where each pixel is treated independently, considering different distributions for foreground and background pixels. The background distribution is trained on all the background pixels of the input image and the foreground distribution is known from the 3DMM. In the second term, $p(\theta)$, they integrated all sources of information to estimate a distribution of the parameters. Basically, they observed that, given a completely automatic pipeline where a face detector and a landmarks detector are needed, both detectors are forced to make an early decision that might be unreliable due to strong pose and illumination variations. Thus, they included the results of the face and landmarks detectors as detection maps, assigning each pixel

in the image the likelihood of having a face (or a specific landmark) in that position. In this way, for each detected face box $_i$, $p(\theta)$ is biased with the position and size of the box and with the landmarks detection map of the box \mathcal{L}_i , $p(\theta|\text{box}_i, \mathcal{L}_i)$. Then, all these proposal distributions (one per detected face) are combined constructing a global distribution $p(\theta|\text{allboxes}, \mathcal{L})$ by computing the mean of the face box-distributions, which includes the knowledge about all the detections.

3.5. Local approaches

Most of the proposed techniques to reconstruct the 3D face of a person from one or more images approach the problem in a global manner, fitting the whole facial model to the image(s). However, Ding et al. [50] and Piotraschke and Blanz [57] addressed the fitting procedure in a local manner considering subregions of the face, although in slightly different ways.

Ding et al. [50] divided the face into four subregions (nose, mouth, eyes, rest) and fitted each of them locally, depending on both their own vertices and adjacent subregions. They estimated the shape parameters four times separately, $\alpha_i, i = 1, 2, 3, 4$, each ensuring that the corresponding face region was optimally fitted without considering the others. Then, the four shape parameters vectors were linearly combined with blending weights that depended on the vertices: $\mathbf{x} = \bar{\mathbf{x}} + \sum_{i=1}^4 \mathbf{w}_i (\Phi \alpha_i)$, with $\sum_{i=1}^4 w_{ij} = 1, \forall$ vertex j . The four shape parameters vectors were estimated at the same time by maximising the posterior probability of the shape parameters given a set of known landmark locations similarly to Aldrian and Smith [44, 46, 45, 47]. Nevertheless, there are two differences: 1) the projection of the 3D-landmarks into the image plane $\hat{\ell}^{2D}$ is the linear combination of the projected 3D-landmarks of the four shapes reconstructed with each α_i , and 2) instead of estimating ad-hoc the variances of the landmarks in the image plane σ_{2D}^2 in $\ell^{2D}|\alpha \sim \mathcal{N}(\hat{\ell}^{2D}|\sigma_{2D}^2)$, a constant weighting factor was used.

Piotraschke and Blanz [57] used multiple in-the-wild pictures of a person and reconstructed individual 3D shapes from each of them very similarly to [69]. Then, they evaluated their quality and combined the best results to form a single 3D face. They studied and compared four quality measures: the Mahalanobis distance, which measures the distance of the reconstruction from the mean shape taking into account the standard deviations observed in the training data, the Euclidean distance from the reconstruction to the mean shape of the model, and the normal distance, which measures the difference between the surface normals of the reconstructed face and the normals of the average face. They found that this last distance measure was the closest to the quality judgements of humans observers. Therefore, the proposed strategy for building a single 3D facial shape from several reconstructions is: 1) fit the 3DMM separately to each of the input pictures, 2) on each segment of the face, select a set

of the K best results according to the normal distance, $\{\mathbf{S}_k^{\text{seg}}\}_{k=1}^K$, 3) for each segment, compute a weighted linear combination of the best reconstructions,

$$\mathbf{S}^{\text{seg}} = \sum_{k=1}^K \lambda_k \mathbf{S}_k^{\text{seg}} \quad \text{with} \quad \lambda_k = \frac{1 - \frac{k-1}{K}}{\sum_{i=1}^K 1 - \frac{i-1}{K}},$$

and finally 4) merge the segments into a single 3D face.

3.6. Take-home message

As stated before, fitting a 3DMM to 2D images basically consists on finding the linear combination of the model bases that produce a 3D face that best resembles the person of the pictures. To do so, the community used different input modalities and proposed different approaches. Whereas the most widespread input is a single image, since it is the most challenging, some researchers fitted a 3DMM to a collection of images from the same subject or even video sequences, which provide more information by observing the subject from different poses and illuminations. Also, most of the proposed works used a set corresponding landmarks to drive the fitting process, but other features such as texture edges [56] or image features [53] have been adopted.

We have identified three main approaches to fit a 3DMM to images: the optimisation of a non-linear cost function, which is the most widespread, the linearisation of the cost function, and a probabilistic point of view. Although all three approaches are different in the way they optimise the model parameters, the fitting process is guided by the same main elements: the landmarks or corresponding 2D-3D points, the rendered image, and statistical regularisation. The set of 2D-3D corresponding points guides the fitting by imposing the known 2D location of the 3D points when projected to the image plane. The rendered image does so by imposing some similarity measure between the rendered and the input images. And, finally, plausible reconstructions are ensured by imposing the statistical regularisation that is defined by the 3DMM.

Whereas the optimisation of a non-linear cost function allows incorporating many different (complex) terms easily, it may be prone to get stuck on local minima or even diverge, and it can be slower than desired due to its computational cost. On the other hand, the linearisation of the cost function avoids most of the issues posed by non-linear approaches given its simpler nature, but it does not allow adding complex terms to the optimisation problem. Finally, probabilistic approaches favour the modelling of uncertainties to the probabilistic inference problem, however, the process of drawing samples from a posterior distribution may be very slow.

4. Photometric Methods

Photometric 3D-from-2D face reconstruction methods estimate the lighting parameters and surface normals from

a set of images usually assuming a Lambertian reflectance model, which defines each pixel (x, y) in an image \mathbf{I} as

$$\mathbf{I}(x, y) = \mathcal{A}(x, y)\mathbf{l}^T\mathbf{n}(x, y) \quad (10)$$

where $\mathcal{A}(x, y)$ is the albedo of the pixel (x, y) , \mathbf{n} its surface normal and \mathbf{l} the light source vector. This model can be approximated using spherical harmonics basis functions, $\mathcal{Y}(\mathbf{n})$, as

$$\mathbf{I}(x, y) \approx \mathcal{A}(x, y)\gamma^T\mathcal{Y}(\mathbf{n}) \quad (11)$$

where γ are the coefficients of the spherical harmonics functions.

This approach to reconstruct the 3D geometry of a surface based on photometry was originally introduced by Woodham [75] who proposed to estimate the surface normals from several 2D images by observing the object under different lighting conditions. However, Woodham’s work assumed a rigid geometry of the object, fixed Lambertian reflectance, fixed camera pose, and uniform albedo. These assumptions have been relaxed by subsequent works to adapt to more realistic settings.

As stated above, the 3D-from-2D face reconstruction problem is ill-posed when considering a single image, and additional constraints are needed to adequately constrain the solution. Some approaches, like Woodham [75], do so by using only a collection of images of the same subject [76, 77, 78, 79] (Section 4.1), whereas others also used template shapes [80, 81] or 3D facial models [82] (Section 4.2). The reviewed works on 3D-from-2D face reconstruction based on photometry are summarised in Table 4, and main conclusions are outlined in Section 4.3.

4.1. Multiple images methods

Kemelmacher-Shlizerman and Seitz [76] reconstructed

the 3D facial shape of a subject given a collection of in-the-wild photos. They proposed to decompose the matrix $\mathbf{M} \in \mathbb{R}^{n \times d}$ of the n vectorised and frontalised images into a matrix $\mathbf{\Gamma} \in \mathbb{R}^{n \times 4}$ containing the coefficients of the lighting and a matrix $\mathbf{S} \in \mathbb{R}^{4 \times d}$ containing the albedo and the surface normals. The initial estimation of $\mathbf{\Gamma}$ and \mathbf{S} was computed using singular value decomposition and taking the rank-4 approximation. Then, the matrices were refined by selecting, for each pixel, the images whose decomposition error was small in that pixel and using them to recalculate their shape vector (the corresponding column of \mathbf{S}). This process was repeated until convergence was achieved.

This work [76] inspired many others. Snape et al. [79] also proposed to decompose a matrix formed by vectorised images; however, the collection of photos was not restricted to a single subject. Thus, they proposed to decompose \mathbf{M} into $(\mathbf{\Gamma} * \mathbf{C})\mathbf{S}$, where $*$ denotes the Khatri-Rao product and \mathbf{C} is a matrix containing the shape coefficients. This allowed them to recover normals for multiple subjects at the same time, unlike Kemelmacher-Shlizerman and Seitz [76], who only recovered the facial geometry of one individual.

Suwajanakorn et al. [78] used the work proposed by Kemelmacher-Shlizerman and Seitz [76] to build a personalised reference shape from a photo collection of a single subject. Their goal was to reconstruct a 3D shape for each frame of a video sequence. Thus, they deformed the personalised template shape to match each frame. These deformations were estimated via a proposed 3D optical flow approach combined with shading cues. This 3D optical flow algorithm computed dense correspondences between the 3D personalised shape and each frame and deformed the mesh to fit the image. These deformations were then refined by minimising a photometric error.

Table 4: 3D-from-2D face reconstruction approaches based on photometry.

Reference	Images	Prior	Illumination model
Kemelmacher-Shlizerman and Seitz [76]	Multiple	Collection of images	Lambertian
Kemelmacher-Shlizerman and Basri [83]	Single	Template mesh	Lambertian
Lee and Choi [84]	Single	Illumination-shape model	Lambertian
Kumar et al. [85]	Single	Illumination-shape model	Non-Lambertian
Lee and Choi [86]	Single	Illumination-shape model	Lambertian
Lee and Choi [87]	Single	Illumination-shape model	Lambertian
Suwajanakorn et al. [78]	Video	Collection of images	Lambertian
Snape et al. [79]	Multiple	Collection of images from multiple subjects	Lambertian
Roth et al. [80]	Multiple	Collection of images and template mesh	Lambertian
Roth et al. [82]	Multiple	Collection of images and 3DMM	Lambertian
Liang et al. [77]	Multiple	Collection of images	Lambertian
Zeng et al. [81]	Three	Collection of reference meshes	Lambertian
Cao et al. [88]	Single	3DMM fitting	Lambertian
Li et al. [89]	Single	3DMM fitting	Lambertian
Rotger et al. [90]	Single	3DMM fitting	Lambertian

Also using only a collection of photos of the same person, Liang et al. [77] reconstructed the whole head. They proposed to clusterise the photos according to the yaw angle of the face. The frontal cluster was used to initialise the reconstruction, and then the different clusters were used to reconstruct the rest of the head progressively. Their method was also based on the work by Kemelmacher-Shlizerman and Seitz [76].

Unlike the works above, Zeng et al. [81] proposed to use only three images (one frontal and two profile ones) and a set of reference meshes. First, an initial estimation of the shape is computed using [76]. This initialisation is refined by minimising an energy function with three terms: a shading term that penalises dissimilarity between the initial and the new estimations; a multi-view consistency term that forces projections of the same 3D point onto neighbouring views to be similar for all the reference shapes; and finally a smoothness term that ensures smooth transitions in depth. According to Zeng et al. [81], using a set of reference meshes, contrary to using a single template mesh, helps increasing the probability of finding the most similar candidate for the input face.

With a similar idea, Roth et al. [80] used a single 3D facial template mesh but, instead of three input images [81], they used a collection of photos. The mesh was warped to all the images by deforming it so that the projection of its landmarks matched the 2D landmarks in all the images (with individual projection matrices). This personalised template mesh was projected into all the images to obtain facial regions for each of them. The facial regions were used to build the matrix \mathbf{M} that was decomposed into $\mathbf{\Gamma}$ and \mathbf{S} following [76]. In their latter publication [82], Roth et al. extended their work by building the personalised template via 3DMM fitting [54]. Also, instead of following [76] to estimate the normals, albedo, and lighting parameters in the Lambertian reflectance model (see eq. (10)), they proposed to minimise an energy function. This function consisted of a term that penalised the difference between each image pixel and its estimated value (according to eq. (10)), and another one that penalised the distance between the ground truth and the estimated surface normals. Finally, they use a coarse-to-fine scheme to first fit the overall face shape and later adapt the coarse estimation to the details present in the collection.

4.2. Single image methods

Differently from the works studied above, Kemelmacher-Shlizerman and Basri [83], Lee and Choi [84, 86, 87] and Kumar et al. [85] only used a single image to reconstruct the 3D face of a person. Whereas Kemelmacher-Shlizerman and Basri [83] included a template mesh as prior knowledge, Lee and Choi [84, 86, 87] and Kumar et al. [85] trained a model that integrated illumination and shape information. Differently, Rotger et al. [90], Cao et al. [88] and Li et al. [89] used photometric methods to refine a coarse 3D face estimated by means of 3DMM fitting.

Kemelmacher-Shlizerman and Basri [83] proposed to recover the albedo, surface normals, and lighting by adopting the spherical harmonics approximation (eq. (11)) of the Lambertian model using a template face for which the albedo, surface normals, and depth map were known. The proposed reconstruction scheme consisted in: 1) recovering the spherical harmonics coefficients γ by fitting the reference shape to the input image (using the normals and albedo of the reference template), 2) estimating the depth map for the input image (by writing the normals as functions of the depth) given the estimated γ and the albedo of the template, and 3) recovering the albedo with the estimated spherical harmonics coefficients and depth map.

Lee and Choi [84, 86, 87] reformulated the estimation of the 3D shape as a photometry-based model fitting problem. Whereas the above approaches vectorised the images to build 2D matrices, Lee and Choi kept the 2D nature of the images and worked with tensors. They assumed a Lambertian reflectance model and approximated it using spherical harmonics such that

$$\mathbf{I} = \mathbf{F} \times_3 \mathbf{l}^T$$

where $\mathbf{I} \in \mathbb{R}^{n_x \times n_y}$ is an image, $\mathbf{F} \in \mathbb{R}^{n_x \times n_y \times n_l}$ is the 3rd-order tensor related to surface characteristics (albedo, normals), and $\mathbf{l} \in \mathbb{R}^{n_l}$ is the light source vector. In Lee and Choi [84], they proposed to parametrise \mathbf{F} as a function of a personal identity vector ι by decomposing it similarly to 3DMM (see Section 2.1) and using N -mode singular value decomposition so that $\mathbf{F} = \bar{\mathbf{F}} + \mathbf{T} \times_4 \iota$, where $\bar{\mathbf{F}} \in \mathbb{R}^{n_x \times n_y \times n_l}$ is the mean of \mathbf{F} , $\mathbf{T} \in \mathbb{R}^{n_x \times n_y \times n_l \times n_{id}}$ is formed by the basis functions, and $\iota \in \mathbb{R}^{n_{id}}$. Thus, an image \mathbf{I}_{new} is reconstructed by finding the \mathbf{l} and ι vectors that minimise the reconstruction error between \mathbf{I}_{new} and $(\bar{\mathbf{F}} + \mathbf{T} \times_4 \iota) \times_3 \mathbf{l}^T$.

In [86], Lee et al. proposed a method to estimate an image depth by fitting a model that considers cast shadows. Similarly to [84], they first reduced the dimension of the training images by building a subspace with tensor decomposition techniques. The representations of the training examples in that subspace were transformed to hyperspherical coordinates to simplify the problem. Finally, a linear mapping was learnt to estimate the depth from these hyperspherical coordinates. The work presented in [84] and [86] was compiled in [87].

Kumar et al. [85], different from all the works above, did not assume a Lambertian model but used apparent bidirectional reflectance distribution functions to model the illumination of faces. They proposed to approximate the field of such functions using *tensor splines*, which are combinations of Cartesian tensors and B-splines. However, whereas the Lambertian model (see eq. (10)) explicitly includes the surface normals in the formula, *tensor splines* do not; thus, recovering the surface normals from the illumination in the image is a nontrivial task. To solve this problem, Kumar et al. assumed local homogeneity of the apparent bidirectional reflectance distribution func-

tions field, i.e. neighbouring pixels have the same shape, only differing by a rotation, which allowed them to derive a surface normal at a pixel by rotating the known normal at another pixel.

Whereas the previous works estimated the 3D face by directly applying photometry-based methods, Rotger et al. [90], Cao et al. [88], and Li et al. [89] used photometry-based methods to refine a coarse 3D face that was estimated by fitting a 3DMM. The idea behind these works is to refine the coarse 3D face estimating per-vertex displacements, which, basically, result from the minimisation of an image error

$$\mathbf{E}_{\mathbf{I}} = \|\mathbf{I}_{\text{in}} - \mathcal{A}\gamma^T\mathcal{Y}\|_2^2$$

where \mathcal{A} , γ , and \mathcal{Y} are as in eq. (11).

Rotger et al. [90] modelled the per-vertex displacement ν^i as functions of the normals \mathbf{n}^i and a value d^i , which can be roughly understood as the distance from the i th pixel to a wrinkle. The wrinkles in \mathbf{I}_{in} were detected as changes on the facial texture according to the partial derivatives in both horizontal and vertical directions. Thus, the updated vertices were computed as $\mathbf{v}^i + \nu^i$, where $\nu_i = \lambda \mathbf{n}^i d^i$. $\lambda \in \mathbb{R}$ is the value that controls the magnitude of the displacement and was computed by minimising

$$\mathbf{E}_{\mathbf{I}} = \sum_{i=1}^{n_x \times n_y} \|\mathbf{I}_{\text{in}}^i - \mathcal{A}^i \gamma^T \mathcal{Y}(\mathbf{n}[\mathbf{v}^i + \nu^i])\|_2^2$$

where $\mathbf{n}[\mathbf{v}^i + \nu^i]$ denotes the normal vector estimated at the updated vertex $\mathbf{v}^i + \nu^i$, $\mathcal{Y}(\mathbf{n})$ denotes the spherical harmonics basis functions computed for \mathbf{n} , and $n_x \times n_y$ is the number of pixels in \mathbf{I}_{in} .

In contrast, Li et al. [89] and Cao et al. [88] directly updated the normals, instead of estimating displacements for each vertex. The first authors added to their image formation model the shadows that cannot be explained by a Lambertian model:

$$\mathbf{I} = \mathcal{A}\gamma^T\mathcal{Y} + \mathcal{B}. \quad (12)$$

They iteratively estimated \mathcal{A} and \mathcal{B} by minimising the difference between both sides of eq. (12) and fixing the normals as the coarse 3D face normals. In a following step, they fixed \mathcal{A} and \mathcal{B} , and estimated the normals.

Differently from the other authors, Cao et al. [88] considered a near point light model, instead of distant directional light sources, given that, since it requires a subset of $K < n_x \times n_y$ key pixels and E light sources, its computational cost and space requirements are lower. They modelled the near point light model by changing the light source vector \mathbf{l} in eq. (10) for the scaled directions \mathbf{e} , which depend on the lights positions and brightness. Thus, they jointly estimated the albedo \mathcal{A} , the normals update, and the light positions and brightness, by minimising the difference between the input and the modelled image.

4.3. Take-home message

3D-from-2D face reconstruction methods based on photometry try to recover the surface normals from a 2D image(s), generally, by assuming a Lambertian illumination model that decomposes an RGB image into albedo, lighting and normals. However, since the images are unconstrained, the source light is unknown and so is the pure albedo. Therefore, additional prior knowledge has to be added to the reconstruction problem in order to constrain it.

The type of prior knowledge used in the proposed works clearly separates them into two groups: the ones that constrain the reconstruction by taking a multiple images from the same subject under different lighting conditions, poses, expressions, etc., and the ones that use a single image but add 3D constraints in the form of 3DMMs or 3D facial templates.

Essentially, the approaches that use a collection of images are based on the decomposition of the matrix formed by the vectorised images into two matrices, one containing the lighting information and the other containing the albedo and surface normals. The single-image approaches are more heterogeneous. For example, some works constructed an illumination-shape model that is then fitted to the image, whereas others refine the coarse 3D face obtained with 3DMM-fitting by minimising the difference between the input image and the image obtained with the Lambertian model using the estimated refined normals.

5. Deep Learning Methods

The 3D-from-2D face reconstruction methods from Section 3 and 4 use models to embody prior knowledge: statistical model fitting methods include a geometry (and usually texture) model, and photometric methods model the reflectance of the face. In contrast, deep learning methods directly learn the mapping between the 2D image and the 3D face, encoding prior knowledge in the weights of the trained network.

Although deep learning has shown to be a very powerful tool in many different applications, its direct application in 3D-from-2D face reconstruction is hampered by the lack of ground truth 3D facial scans. However, researchers have proposed different approaches to generate and learn from realistic representative training data, circumventing the obstacle of the lack of ground truth data.

In this section, we present and compare the most relevant works in 3D-from-2D face reconstruction that use deep learning as the main tool. Among the many elements that are involved in the learning process, we consider three representative ones, namely, 1) the training set used to train the network, 2) the learning framework, and 3) the training criterion. We organise this section according to these items.

Tables 5, 6, and 7 summarise the main characteristics of each of the reviewed deep learning works according to the

Table 5: 3D-from-2D face reconstruction approaches based on deep learning - part I.

Reference	Synthetic training		Learning framework				Training criterion		
	Fit	Render	Network type	# Layers	Skip connect.	Iterative	Param. space	3D space	2D space
Song et al. [91]		–	Encoder Decoder	3 3	No No	No No	x		
Zhu et al. [92]	x	x	CNN	6	No	Yes	x		
Richardson et al. [93]		x	Residual	18	Yes	Yes		x	
Jourabloo and Liu [94]	x		CNN	6	No	Yes	x		
Jourabloo and Liu [95]	x		CNN CNN	5 6	No No	No Yes	x		x
Bhagavatula et al. [96]	x	x	CNN FC	8 (16) ¹ #lmks//4//4	No No	No No		x	
Dou et al. [97]		x	CNN CNN	16 19	No Yes	No No		x	
Alp Güler et al. [98]	x	x	Residual FC	101 4 × 1	Yes No	No No	x		
Jackson et al. [99]	x	x	Encoder Decoder	6 5	Yes Yes	No No		x	
Richardson et al. [100]		x	Residual CNN	19 16	Yes No	Yes No		x	x
Sela et al. [101]		x	Encoder Decoder	8 8	Yes Yes	No No		x	
Tewari et al. [102]	x	x	CNN	8	No	No			x
Jourabloo et al. [103]	x		CNN	24	Yes	No	x		
Trigeorgis et al. [104]	x	x	Residual	50	Yes	No		x	
Tran et al. [105]	x		Residual	101	Yes	No	x		
Tran et al. [19]	x		Residual Encoder Decoder	101 8 8	Yes Yes Yes	No No No	x		
Liu et al. [106]	x		Encoder Decoder	21 2 × 1	No No	No No		x	
Liu et al. [107]		x	Encoder Decoder	21 2 × 1	No No	No No		x	
Kim et al. [108]	x	x	CNN	8	No	Yes	x		
Tran and Liu [34]	x	x	Encoder Decoder	14 15 // 17	No No	No No			x
Sengupta et al. [109]		x	CNN Residual CNN	3 2 × 10 (2 × 3) // 2	No Yes No	No No No	x		x
Tewari et al. [110]	x	x	CNN	8	No	No			x
Feng et al. [111]	x	x	Encoder Decoder	21 17	Yes No	No No		x	
Guo et al. [18]		x	Residual Encoder Decoder	18 10 9	Yes Yes Yes	No No No			x
Genova et al. [112]		x	Encoder Decoder	22 3	No No	Yes Yes	x		
Tewari et al. [113]	x	x	CNN	8	No	No			x
Zhu et al. [114]	x	x	CNN	6 // 7	No	Yes	x		
Tran and Liu [115]	x	x	Encoder Decoder	14 15 // 17	No No	No No			x

¹ Bhagavatula et al. [96] compare two different CNNs, one with 8 layers and the other with 16.

Table 6: 3D-from-2D face reconstruction approaches based on deep learning - part II.

Reference	Synthetic training		Learning framework				Training criterion		
	Fit	Render	Network type	# Layers	Skip connect.	Iterative	Param. space	3D space	2D space
Tran et al. [116]	x	x	Encoder Decoder	14 15 // 17	No No	No No			x
Zhou et al. [117]	x	x	Encoder Decoder	11 // 4 4	No No	No No		x	x
Sanyal et al. [118]		–	Residual FC	50 3	Yes No	No Yes	x		x
Galteri et al. [119]	x	x	Generator Discriminator	19(enc)+19(dec) ¹ 19	No No	No No		x	
Galteri et al. [120]	x	x	Generator Discriminator	19(enc)+19(dec) ¹ 19	No No	No No		x	
Deng et al. [121]	x	x	Residual	50	Yes	No	x		x
Wu et al. [122]	x	x	CNN FC	19 2 × 2	No No	No No	x		x
Yi et al. [123]	x	x	Encoder ² Decoder ² CNN FC	6 5 5 3 × 1	Yes Yes No No	No No No No		x	x
Piao et al. [124]		x	Generator ³ Discriminator ³ Encoder Decoder	8(enc)+8(dec) ³ 6 20 5	Yes No No No	No No No No		x	x
Yoon et al. [125]	x		Encoder ⁴ Encoder ⁴ FC Decoder	19 5(enc)+6(dec) ⁵ 2 × 4 10	No Yes No No	No No No No	x		x
Wang et al. [126]		–	CNN	28	No	No			x
Savov et al. [127]		–	CNN	7	No	No			x
Ramon et al. [128]		–	CNN MLP	16 4	No No	No No		x	
Zeng et al. [129]	x	x	Encoder Decoder CNN	10 9 9+16 ⁶	Yes Yes Yes	No No No		x	x
Bai et al. [130]		x	Residual Residual	49 16	Yes Yes	Yes Yes		x	x
Chinaev et al. [131]	x		CNN	28	No	No		x	x
Chaudhuri et al. [132]	x		CNN FC	25 3 × 1	No No	No No		x	x
Chaudhuri et al. [133]		–	Residual Encoder Decoder	18 8 8	Yes Yes Yes	No No No	x	x	x
Zhang et al. [134]	x	x	CNN FC	4 3 × 3	No No	No No		x	x

¹ Galteri et al. [119, 120] proposed a generator with an encoder-decoder architecture, with 19 layers each.² Yi et al. [123] stacked two encoder-decoder networks, followed by two CNNs.³ Piao et al. [124] considered a CycleGAN composed of two stacked GANs. The generators are encoder-decoder networks with 8 layers each.⁴ Yoon et al. [125] used two parallel encoders for the same decoder.⁵ One of the encoders used by Yoon et al. [125] is an hourglass network, which has an encoder-decoder architecture with 5 and 6 layers, respectively.⁶ Zeng et al. [129] trained separately two CNN with skip connections, one that refines the output of the other.

Table 7: 3D-from-2D face reconstruction approaches based on deep learning - part III.

Reference	Synthetic training		Learning framework				Training criterion		
	Fit	Render	Network type	# Layers	Skip connect.	Iterative	Param. space	3D space	2D space
Guo et al. [135]	x	x	CNN FC	28 2×1	No No	No No	x	x	x
Lin et al. [136]		–	Generator Discriminator	Mixed ¹ 6	Mixed ¹ No	No No	x	x	x
Shang et al. [137]	x	x	Residual	50	Yes	No		x	x
Koizumi and Smith [138]		–	Encoder Decoder	8 8	Yes Yes	No No	x	x	
Lattas et al. [139]		–	Encoder ² Decoder ² CNN Generator Discriminator ²	19 19 1013 $24 + (3 \times 24)$ 3×4	No No Yes Yes No	No No Yes No No		–	x
Wang et al. [140]	x	x	Residual Enc-Dec Enc-Dec	18 $4(\text{enc})+4(\text{dec})^3$ $4(\text{enc})+4(\text{dec})^3$	Yes Yes Yes	No No No		x	x x x
Tewari et al. [141]		–	CNN CNN CNN	5 5 7	No No No	No No No			x
Chai et al. [142]	x	x	Encoder Decoder FC CNN CNN	16 2×5 2 16 16	No No No No Yes	No No No No No	x		x
Fan et al. [143]	x		CNN MLP	52 $\#\text{verts} \times 1$	Yes No	No No		x	
Li et al. [144]	x		Encoder Decoder	$18 // 50$ N/A	Yes No	No No		x	
Tu et al. [145]	x	x	Generator Discriminator	50 $6(\text{CNN})+4(\text{FC})$	Yes No	No No		x	
Wang et al. [146]	x	x	Residual Encoder Decoder	18 $(\#\text{images}+1) \times 4$ 5	Yes No No	No No No		x	x
Zhu et al. [147]	x	x	Encoder Decoder	21 17	Yes No	No No		x	
Chen et al. [148]		–	CNN Encoder Decoder	16 8 8	No Yes Yes	No No No	x		x x x
Gao et al. [149]	x	x	Generator Discriminator	Mixed ⁴ N/A	Mixed ⁴ No	No No		x	x
Shu et al. [150]	x	x	CNN Encoder Decoder	N/A 8 8	Yes Yes Yes	No No No	x		x x x

¹ Lin et al. [136] used a mixed generator composed of a CNN, a residual network and three GCN, two of them with skip connections.² Lattas et al. [139] used as generator the pre-trained network from Gecer et al. [64]. They also adopted the GAN architecture from Wang et al. [151] that has three discriminators.³ Wang et al. [140] trained two encoder-decoder networks separately for different tasks.⁴ The generator used by Gao et al. [149] is composed of a residual network, four parallel fully connected layers and three GCN, one of them with skip connections.

above items. The *training set* column indicates whether the network was built by fitting a 3DMM to real images or by rendering synthetic images from a 3D face (or both). In the learning framework, four attributes are specified: the network type, the number of layers, whether skip connections are used, and whether the learning process is iterative. The number of layers is indicated as $A \times B$ if the network consists of A networks of B layers each, and $B_1//B_2//\dots//B_n$ if there are n networks arranged in parallel with B_1, \dots, B_n layers respectively. Finally, the training criterion column indicates if the loss function is computed in a parameters space, the 3D space, and/or the 2D space.

5.1. Training data set

As we have mentioned above, the biggest obstacle when applying deep learning to 3D-from-2D face reconstruction is the lack of training data, since obtaining the huge number of 3D facial scans together with their corresponding 2D pictures required by deep learning algorithms is impractical. To overcome this limitation, researchers have proposed techniques for building synthetic training sets. These techniques take advantage of pre-built 3DMMs to obtain 3D faces in a much more accessible way.

We can distinguish two main strategies to build synthetic training sets. The first one is fitting a 3DMM to real images, and then rendering synthetic images using the estimated 3D faces. The second one is generating 3D faces by randomly sampling from a 3DMM and then, again, rendering synthetic images using the generated 3D faces. We refer to the first approach as *Fit&Render* and to the second one as *Generate&Render*.

The *Fit&Render* strategy was first introduced by Zhu et al. [92]. They proposed a face profiling technique that is used to generate images across larger poses, creating the 300W-LP (300W large poses) database. They first estimated a 3D mesh over the given face image by fitting a 3DMM using [152] and [54] over the background. Then, the 3D mesh was rotated and projected to the image to generate a synthetic image similar to the original one but with a large pose. This 300W-LP database has been used by many other authors [96, 111, 98, 99, 34, 115, 116, 123, 114, 134, 135, 137, 145, 149, 150] since it includes realistic and challenging facial images with the ground truth 3DMM and projection parameters. Galteri et al. [119, 120] also followed the *Fit&Render* strategy to augment the Face Recognition Grand Challenge dataset [153] by generating images with novel poses similarly to Zhu et al. [92].

Closely related to the *Fit&Render* strategy, some other works proposed to fit a 3DMM to images without rendering afterwards [94, 95, 103, 106, 105, 19, 125, 131, 132, 144]. Jourabloo and Liu [94, 95], Jourabloo et al. [103], and Chinnavev et al. [131], Chaudhuri et al. [132] and Li et al. [144] estimated the 3DMM parameters independently for each training image, whereas Liu et al. [106] and Tran et al. [105, 19] combined parameters extracted from multiple images of the same person. Liu et al. [106] fitted a 3DMM

to multiple images enforcing common shape parameters to all the images of the same subject and estimating independently for each image the shape deformation due to expressions. In contrast, Tran et al. [105, 19] computed a weighted average of the shape and texture parameters estimated from the pictures of the same person. The resulting parameters were considered the ground-truth for all the images of that subject. Differently from all the other works, Yoon et al. [125] used the non-linear face model created by Lombardi et al. [154], who used an autoencoder network to learn a non-linear representation of textured 3D faces, and took as training set the images fitted by Lombardi et al. [154] in their training phase. This training dataset consists of 2D videos (i.e. consecutive 2D images) from different angles and the corresponding model parameters.

The *Generate&Render* strategy was used by Richardson et al. [93], proposing a weak perspective projection and the Phong reflectance model Phong [68] to render the synthetic images. This approach was strictly followed by some [97, 100, 101] and inspired others [18]. Richardson et al. [100] and Sela et al. [101] trained their networks using only the dataset generated by [93], unlike Dou et al. [97], who also used publicly available 3D face databases, namely, the FRGC2 database [155], the BU-3DFE database [156], and the UHDB31 database [157]. Guo et al. [18] also followed the strategy presented by [93]. However, they considered that the rendered images in [93] were not sufficiently photo-realistic. To overcome this shortcoming, they proposed an inverse rendering method, which they used to create their own synthetic training set.

Similarly to Richardson et al. [93], Piao et al. [124] followed the *Generate&Render* strategy to build their training set. However, they added small free-form deformations to the nose and chin of some of the generated 3D faces. According to the authors, this allowed them to synthesise more realistic facial shapes, since real faces may not be completely captured by a linear model.

Sengupta et al. [109] and Genova et al. [112] trained their networks in a two stage manner. Sengupta et al. [109], in the first stage, trained a simple network over synthetic data extracted using the *Generate&Render* technique. In the second stage, they used the pre-trained simple network to obtain normal, albedo and lighting estimates for a set of real images. The training data set was composed of synthetic 3D-2D data and 2D real images with the estimated normals, albedo and lighting, whose goal was to prevent the network to produce trivial solutions. In contrast, Genova et al. [112] trained the network with different training sets in each stage. In the first stage, they used synthetic 3D-2D data generated following the *Generate&Render* strategy, whereas in the second stage, they used only unlabelled images within an autoencoder architecture.

The two main strategies, *Fit&Render* and *Generate&Render*, were combined by Trigeorgis et al. [104], Zeng et al. [129] and Kim et al. [108]. Trigeorgis et al. [104]

constructed their training dataset using the ICT-3DRFE database [158] and the Photoface database [159] to generate synthetic images varying the illumination. They followed the *Fit&Render* strategy using the LSFM [39] as 3DMM and adding expressions with the FaceWarehouse model [41]. With the same models, they randomly generated synthetic 3D faces, which were aligned to in-the-wild images to provide realistic backgrounds to the rendering. Zeng et al. [129] built their training set in a similar way, using both strategies, although they also added images from the CACD dataset [160] without corresponding 3D faces to train their network in a self-supervised manner. In contrast, Kim et al. [108] built a first training set using *Generate&Render* which was used to pre-train the network. Then, during iterative training, they followed the *Fit&Render* strategy using the pre-trained network to estimate the model parameters from real images. Gaussian noise was added to these estimated parameters before rendering synthetic images, which were used to train the network in the next iteration.

Although most of the works built training sets following one of the two main strategies, there are others that followed none of them. Song et al. [91], Bai et al. [130], Fan et al. [143], Ramon et al. [128], Lattas et al. [139], Wang et al. [146] and Zhu et al. [147] trained their network using only real data. The first authors obtained the 2D-3D pairs from the BU-3DFE database [156], whereas Bai et al. [130], and Fan et al. [143] used the Stirling/ESRC 3D face database and the FRGC v2.0 database, respectively. The first authors enlarged the training set by rendering 2D images from the textured 3D scans, whereas [143] fitted a 3DMM to 2D images and then non-rigidly registered them to the triangulated depth images to obtain ground truth 3D faces with the same triangulation. In a similar way, Zhu et al. [147] also fitted a 3DMM but to RGB-D images and the non-rigid registration was conducted by finding correspondences based on geometry and texture. Instead, Ramon et al. [128], Lattas et al. [139], and Wang et al. [146] built the training set themselves. The first [128] captured 2D images and 3D faces from more than 6,000 subjects, and the second [139] captured 3D faces and reflectance maps of over 200 individuals under 7 different expressions. Since Wang et al. [146] estimated the 3DMM parameters, they constructed a dataset by refining, with known photometric parameters, the coarse shape extracted by fitting a 3DMM to three images captured under different lighting conditions. In addition, they enlarged the training set by following the *Generate&Render* approach but transferring the albedo from the captured images. They also rendered synthetic images from 3D faces obtained by non-rigidly registering the mean of the 3DMM to the 3D faces in the Light Stage [161] database and, again, transferring the albedos from the captured images.

On the other hand, given the lack of real 2D-3D paired data, a new strategy is raising in the last few years that consists in self-supervised training. [102, 110, 113, 34, 115, 116, 121, 117, 127, 122, 136, 133, 138, 140, 141, 142, 148]

trained their networks in an self-supervised manner by adding a rendering layer at the end of the network, which renders a synthetic image given the features estimated by the main network. This enables to train the networks end-to-end without the need of ground truth 3D faces. Some works [102, 110, 113, 34, 115, 116, 121, 117, 122, 140, 142] trained their network with synthetically modified images to enlarge the variability in illumination, pose, etc., whereas others only used real images [127, 136, 133, 138, 141, 148].

In addition, Zhou et al. [117] used a set of real 3D facial scans to train an autoencoder network, whose decoder is used in the image-to-mesh encoder-decoder network, and Wu et al. [122] pretrained their network in a fully supervised manner using the 300W-LP dataset generated by Zhu et al. [92]. Sanyal et al. [118] and Wang et al. [126] also trained their network in a self-supervised manner, but instead of by rendering a synthetic image, they projected only the landmarks position onto the image plane.

Liu et al. [107] and Tu et al. [145] also trained their networks in a self-supervised manner, but they did not add a rendering layer. Liu et al. [107] trained a 3D-to-3D autoencoder network to use the decoder in the 3D face reconstruction process, similarly to [117]. Like [117], they used 3D facial scans to train the autoencoder in a self-supervised manner (without having dense correspondence between the input 3D scan and the output reconstruction), but included synthetic 3D faces generated using a 3DMM to also train it in a supervised manner (having dense correspondence). On the other hand, Tu et al. [145] combined images with ground truth 3DMM and pose parameters, with images without supervision. In this way, the network estimates parameters for the images without ground truth from the conditional distribution learnt from the images with ground truth.

5.2. Learning framework

The core part of a deep learning algorithm is the network itself, in terms of its architecture and how it learns its weights. The most straightforward learning framework is a single neural network that is trained in a single pass (Section 5.2.1). As an alternative, networks can be trained iteratively (Section 5.2.2) and/or exploiting the potential of multiple networks, such as in the encoder-decoder architecture (Section 5.2.3), in the generative adversarial networks (Section 5.2.4), or by training each network for a specific task (Section 5.2.5)

5.2.1. Single Network with Single-Pass Training

Chinaev et al. [131], Guo et al. [135], Chaudhuri et al. [132], Ramon et al. [128], Tewari et al. [102, 110, 113], Savov et al. [127], Wang et al. [126] and Wu et al. [122] used a convolutional neural network (CNN). Chinaev et al. [131] and Guo et al. [135] used the MobileNet [162] to estimate the parameters of a 3DMM. Whereas the first authors directly estimated the 3DMM, the rendering and projection

parameters with the MobileNet, [135] passed its output through two separated fully-connected layers: one to estimate the 3DMM and projection parameters and the other to estimate the 2D landmark locations. Chaudhuri et al. [132] built a CNN with Fire Modules from the SqueezeNet [163] and squeeze-and-excite modules [164] with the aim of reducing the model size and complexity without compromising the accuracy of the results. Similarly, Ramon et al. [128] used the VGGNet [165] concatenated with a 3-layers multilayer perceptron to estimate the shape and the projection parameters for each of the K input images of the same subject, thus obtaining K different outputs. The K shape parameters vectors are then combined by a multilayer perceptron to output a single vector. Tewari et al. [102, 110, 113] and Savov et al. [127] based their network on the AlexNet architecture [166] to estimate the 3DMM parameters (shape, expression, and texture) together with the rendering parameters (projection and illumination parameters). Besides, Savov et al. [127] used an additional AlexNet to estimate the age of the person, and they employed a soft weights sharing strategy [167] between both networks, which consists in adding layers that linearly combine activations from analogous layers from both networks. In the training stage, the weights of the linking layers are learnt jointly to the rest of both AlexNets, and thus the network learns which weights to share.

Tewari et al. [110, 113] improved their work [102] by refining the output of the CNN by estimating displacements for each vertex in the resulting 3D face as coefficients from a generative model that is learnt directly from the training data. Similarly, Wang et al. [126] trained a CNN to output shape and expression parameters from a 3DMM, the projection parameters, and middle-level corrections. These corrections are represented as a deformation 3D field modelled by linear manifold harmonics basis functions [168]. In contrast, Wu et al. [122] used the VGGNet [165] to extract features from three images of the same subject (frontal, left, and right views). These features are then processed by two separated fully-connected layers: one of them estimates the projection parameters of each image, and the other one estimates the 3DMM shape and expression parameters of the subject from the concatenation of all the features extracted by the network. Finally, a coloured mesh is obtained by recovering the texture of the face from the input images.

On the other hand, Tran et al. [105], Trigeorgis et al. [104], Deng et al. [121], Shang et al. [137], Jourabloo et al. [103] and Koizumi and Smith [138] used residual CNNs. Whereas the first four authors used the ResNet architecture [169], the first one with 101 layers and the latter three with 50 layers, Jourabloo et al. [103] added two fully-connected layers at the end of each residual block, and Koizumi and Smith [138] adopted the U-Net [170].

Whereas [104, 137, 138] used a simple learning framework, they differ in some aspect from the rest of the proposed works. Trigeorgis et al. [104] estimated the facial

normals instead of regressing the 3D face or 3DMM parameters. Unlike the other works, which are focused on single-image reconstruction, Shang et al. [137] proposed to use two additional images from adjacent views with respect to the target image. This multi-view framework allows them to further drive the reconstruction by imposing multi-view consistency. Finally, Koizumi and Smith [138] trained their network to build a correspondence map between a 3DMM and the input image without the need of any predefined initial set of correspondences (e.g. 2D-3D landmark correspondences), also estimating a depth map. With the correspondence and depth maps, they are able to solve a least squares problem to first estimate the 3DMM shape parameters and then the 3DMM texture and the rendering parameters. The network is trained end-to-end by adding the least squared layer and a rendering layer.

5.2.2. Iterative Training

In contrast to the single pass training adopted by the works in the previous section, other authors proposed to train their networks in an iterative manner. We can distinguish two different approaches: one is based on iteratively improving the synthetic training set, and the other on iteratively refining the result of the previous iteration.

Kim et al. [108] followed the first approach. They updated the training set in each iteration by adding synthetic images that were rendered using parameters (after adding a Gaussian noise) estimated from real images by the trained network up to the current iteration. Thus, in each iteration, the network was trained over a training set generated by the “previous” network. In this way, the training data distribution is more similar to the real distribution, alleviating the bias effect of the synthetic data in the training process.

The second approach follows a similar idea to that of a cascaded regressor: each regressor estimates an update of the input parameters, which are estimated by the previous regressor, such that they are closer to the ground truth.

Richardson et al. [93], Sanyal et al. [118], Zhu et al. [92, 114], Bai et al. [130] and Zhang et al. [134] used the same architecture for all the iterations. Richardson et al. [93] and Sanyal et al. [118] proposed a network based on the ResNet architecture [169], although the latter added 3 fully-connected layers to regress 3DMM parameters from the features extracted by the ResNet. In contrast, Zhang et al. [134] and Zhu et al. [92] used simple 4 and 6-layers CNNs, respectively. In addition, the first authors stacked 3 streams of 3 fully-connected layers to regress separately the 3D shape, the 2D landmarks, and the pose parameters. Similarly, Zhu et al., in their extended work [114], proposed a two-stream network: two separated CNNs with 5 and 6 layers each and a fully-connected layer to combine the output of both streams. This architecture allowed them to separately process two different types of features extracted from the 3D face estimated in the previous iteration. Differently from [93, 118, 92, 114], Bai et al. [130]

reconstructed the 3D facial shape of a subject from a collection of 2D pictures. In addition, their approach differs from that of the other works since, instead of estimating the parameters update, they estimated an update of the previously estimated 3D face for 3 iterations. In each of them, they learn an *adaptive basis* Φ_{adap} that models the current update as $\Delta \mathbf{x}^i = \Phi_{\text{adap}}^i \alpha_{\text{adap}}^i$, thus the final reconstruction is computed as $\mathbf{x} = \bar{\mathbf{x}} + \Phi \alpha + \sum_{i=1}^3 \Phi_{\text{adap}}^i \alpha_{\text{adap}}^i$. The model parameters α , α_{adap} and the pose parameters are estimated by minimising a cost function composed of a landmark error and a photo-consistency term, which ensures consistency across all the images. The minimisation is done using gradient descent, where the best step size is computed using a multi-layer perceptron network.

In contrast, Jourabloo and Liu [94, 95] considered two different regressors that were alternated: one that estimated the 3DMM parameters updates, and another one that estimated the projection parameters updates. Whereas in [94] they used a “simple” CNN, in [95] they changed all the regressors except the first one. They used a Siamese network [171] that has two branches with shared weights. The input to this network is the original face image together with its mirrored image. This ensures that the estimated update of the 2D landmarks (projection of the 3D landmarks) for both the input image and the mirrored image are similar, which they claimed that further constrains the face alignment problem, and thus ending up with better reconstructions.

5.2.3. Encoder-Decoder

The encoder-decoder architecture partitions the network in two parts: the encoder, which extracts representative features of reduced fixed dimensionality from the input face image, and the decoder, which estimates a reconstruction of the input data from the features estimated by the encoder. This reconstruction may be a synthetic 2D image resembling the input one, a 3D face whose geometry corresponds to that of the face from the input image, or parameters of a 3DMM with which the 3D face can be recovered, among others.

Tran and Liu [34] proposed to use a single CNN encoder that estimates the projection parameters and two sets of features that can be related to shape and texture. These two sets of features are decoded by two CNNs: one decoder converts the shape features estimated by the encoder into a 3D shape, and the other decoder transforms the texture features into an UV texture map. The resulting coloured 3D face is then rendered into a synthetic 2D image that is used to train the network in a self-supervised manner. In their latter works, [115, 116], they estimated separately the lighting of the input image, instead of estimating jointly all the texture-related features. They assumed a Lambertian illumination model and approximated it using spherical harmonic basis functions, so the encoder estimated the spherical harmonics coefficients, in addition to the projection, the shape, and the texture (without lighting) param-

eters.

Chaudhuri et al. [133], Li et al. [144], Yoon et al. [125] and Zhou et al. [117] followed a very similar approach but without separating the shape-related and texture-related features and proposing a more complex architecture. Chaudhuri et al. [133] and Li et al. [144] trained two networks in an end-to-end manner to estimate separately the identity-specific features and the expression-specific features. The first authors [133] trained the *ModelNet*, an encoder-decoder network with one encoder and two separate decoders that estimate shape and albedo corrections. The *TrackNet* is a residual network that estimates the pose, expression, and illumination coefficients for each of the input images. Like in [34, 115, 116], a rendering layer is added to train both networks in a self-supervised manner. On the other hand, Li et al. [144] trained two parallel encoder-decoder networks to estimate the identity and the expression features separately by taking global and local perspectives, respectively. To do so, the identity network inputs the cropped face from the input image, whereas the expression network inputs different local regions of the input facial image, both detected using [172]. The encoders are ResNet networks [169], with 18 layer and 50 layers, each. The decoders are MLP networks that estimate the identity and the expression deformations with respect to the mean face of a 3DMM.

Unlike [133, 144], Yoon et al. [125] and Zhou et al. [117] considered two different encoders but only one decoder. The first authors used the VGGNet [165] and the hourglass network [173] to extract features from the input image. Features extracted from intermediate layers from both encoders are concatenated and processed by two separate blocks of fully-connected layers [174]. With this architecture they estimated separately the pose parameters and the parameters of the deep appearance face model of Lombardi et al. [154]. As explained in Section 5.1, this model is constructed as an autoencoder network, where the encoder learns a representation of a textured 3D face, and the decoder recovers the original surface from the representation. Thus, the decoder used by Yoon et al. [125] that recovers the textured 3D face from the model parameters is the pre-trained decoder from the model.

In contrast, Zhou et al. [117] used one encoder to extract features from a 2D image and the other one to extract features from a 3D coloured facial meshes. Therefore, their architecture consists of a mesh-to-mesh stream and an image-to-mesh stream, which share the decoder. This allowed them to jointly train the decoder 1) in a fully supervised manner for the mesh-to-mesh stream; and 2) in a self-supervised manner for the image-to-mesh stream by adding a final rendering layer that creates a synthetic image from the resulting 3D face. For the image-encoder they used a simple CNN, whereas the mesh-encoder and the decoder consist of four geometric convolutional filters as presented by Ranjan et al. [175].

In other encoder-decoder approaches, the decoder reconstructs a 3D representation of the face from the image

features extracted by the encoder. Song et al. [91], Genova et al. [112], Liu et al. [106] and Liu et al. [107] output a 3D facial mesh reconstructed from an input image. Song et al. [91] stacks two radial basis function networks, which extract the same intrinsic representation from the 2D image (the *2D-network*) and from the 3D face (the *3D-network*), respectively. Thus, the encoder-decoder architecture was constructed by stacking the *2D-network* (encoder) and the inverted *3D-network* (decoder). Liu et al. [106] and Liu et al. [107] used the SphereFace network [176] to estimate separately identity and identity-irrelevant (expression) features. Two different multilayer perceptron networks were used as decoders, which output the identity and identity-irrelevant difference with respect to a mean shape. The final reconstruction was computed adding these differences to the mean shape. However, whereas [106] trained directly the image-to-mesh network, [107] trained a mesh-to-mesh autoencoder, similarly to [117], and then used the trained decoder as the decoder in the image-to-mesh network. Unlike [91, 106, 107], Genova et al. [112] estimated the parameters of a 3DMM using the FaceNet network [177] as the encoder and a network with two fully-connected layers as the decoder.

Sela et al. [101] and Feng et al. [111] estimated depth maps from the input images by using encoder-decoder networks with skip connections. The former based their network on the U-Net architecture [170], where the skip connections are used between corresponding layers in the encoder and the decoder. The network’s output are a depth map and a correspondence map from each pixel of the image to a vertex of a reference mesh, with which a coarse facial mesh is built. From this coarse mesh and the input image, fine details are reconstructed by estimating a displacement map. On the other hand, Feng et al. [111] proposed a residual CNN with an encoder-decoder architecture where the encoder maps the input image to a feature map and the decoder converts this feature map into a position map containing the XYZ coordinates of the estimated shape. Zhu et al. [147] trained the network from [111] to estimate a shape update from an initial shape estimation \mathbf{x}^0 obtained with [114]. More specifically, they input the vertex positions and the texture of \mathbf{x}^0 as UV-maps. The texture UV-map is weighted by an attention map extracted from the visibility of the vertices in the input image. The final reconstruction is obtained by adding the estimated update to \mathbf{x}_0 .

Differently from all the previous works, Jackson et al. [99] reconstructed volumetric representations of the face by stacking two encoder-decoder networks to refine the output of the first network with the second one. Each network is a hourglass network [173], which uses residual modules and skip connections between corresponding layers in the encoder and the decoder. Using residual modules allowed the authors to compute the next-resolution features by taking into account features from previous resolutions. The feature representation estimated by the encoder is mapped back to the spatial domain using residual

modules and combining features from different resolutions from the encoder using the skip connections. A closely related work was presented by Yi et al. [123], who used [99] to map the input image to a volumetric representation. However, Yi et al. [123] added a CNN to estimate the projections parameters and the shape and expression parameters from a 3DMM. The projection parameters are refined in a post-processing step by aligning the facial geometry estimated with the 3DMM to the volume predicted by the hourglass networks.

5.2.4. Generative Adversarial Networks

Lin et al. [136], Galteri et al. [119, 120], Tu et al. [145], Gao et al. [149], and Piao et al. [124] proposed to use generative adversarial networks (GANs) to learn the distribution of the ground truth parameters. Basically, the idea behind GANs is to jointly train two separate networks, the generator and the discriminator, to compete with each other. The generator $G : \mathcal{X} \rightarrow \mathcal{Y}$ is a simple mapping function that maps the input data $\mathbf{x} \in \mathcal{X}$ to a (possibly) different space $\mathbf{y} \in \mathcal{Y}$, $G(\mathbf{x}) = \mathbf{y}$. The discriminator estimates the probability of a data point $\mathbf{y} \in \mathcal{Y}$ of being ground truth data and not being synthetically generated by G . In this framework, the discriminator is trained to correctly distinguish between real and synthetic data, whereas the generator is trained to fool the discriminator by generating data resembling real data.

Lin et al. [136] and Galteri et al. [119, 120] trained a GAN architecture to refine the coarse approximation obtained with 3DMM fitting approaches. Specifically, Lin et al. [136] used this approach to refine the texture estimated by the 3DMM-based reconstruction network proposed by [121]. The texture parameters are the input of a graph convolutional network (GCN) [178, 179] with 8 graph convolutional layers and skip-connections similar to a residual network. At the same time, image features are extracted from the input image using FaceNet [177], which are decoded by a GCN similar to the previous one. The outputs of the GCNs are stacked together and further processed by a single graph convolutional layer. The output of this architecture is a refined per-vertex texture. Finally, a rendering layer generates a synthetic image that is passed to a 6-layer CNN discriminator.

On the other hand, Galteri et al. [119, 120] refined the coarse shape obtained by fitting a 3DMM using a conditional GAN. It consists of an encoder-decoder generator that inputs a coarse 3D face and outputs its detailed version, and a discriminator, with the same architecture as the encoder, that estimates the probability of a detailed 3D face of being a ground truth 3D face, given the coarse face. In addition, this conditional GAN was trained using the procedure proposed by Karras et al. [180], which is based on progressively and simultaneously growing the dimension of the generator and the discriminator. That is, in each iteration, the coarse 3D face and the real detailed 3D face are down-sampled to a certain resolution and the GAN architecture is trained. When the training

for a given resolution is concluded, the scale of the input is doubled, and a new set of convolutional layers is added to both G and D . According to the authors, this way of training the GAN model allows progressively learning finer details as the resolution of the input increases.

Since processing 3D meshes is harder than processing 2D images, Galteri et al. [119, 120] converted the 3D faces into 2D images by projecting them to the image plane using an orthographic projection. Nonetheless, instead of projecting the (x, y, z) coordinates of the mesh vertices, they extracted 3 features from each vertex. Galteri et al. [119] used the depth (i.e. z coordinate) and the azimuth and elevation angles of the normal vector. However, Galteri et al. [120] experimentally found that the azimuth angle did not add relevant information, and thus they replaced it by the mean curvature of the surface at the given vertex, which encodes the local variability of the face.

Tu et al. [145] and Gao et al. [149] used a discriminator to enforce the generator to regress more realistic reconstructions. The first authors [145] proposed a conditional GAN, where the generator is a 50-layer ResNet network [169] that estimates 3DMM shape α and expression β parameters, and the projection parameters ζ , and the discriminator determines whether the estimated parameters follow the conditional distribution learnt from images with ground truth parameters. More specifically, they processed images \mathbf{I} with known $\{\alpha, \beta, \zeta\}$, and images $\tilde{\mathbf{I}}$ with $\{\tilde{\alpha}, \tilde{\beta}, \tilde{\zeta}\}$ estimated by the generator with a 6-layer CNN that outputs feature vectors \mathbf{f} and $\tilde{\mathbf{f}}$, respectively. Then, a 4-layer fully-connected network determines if \mathbf{f} is consistent with $\{\tilde{\alpha}, \tilde{\beta}, \tilde{\zeta}\}$ in the same way as \mathbf{f} is consistent with the ground truth $\{\alpha, \beta, \zeta\}$. This way, according to the authors, the generator is trained to regress more precise and robust parameters. Gao et al. [149] followed a similar idea, in this case, training a discriminator to distinguish real 3D faces from the ones estimated by the generator. The generator is an encoder-decoder network. The encoder is a 50-layer ResNet [169] to which 4 fully-connected branches are attached to estimate separately the lighting and pose parameters and identity and expression features. Unlike Tu et al. [145], the identity and expression are not modelled by a 3DMM, but decoded by 2 GNCs: one that estimated the 3D face from both features and the other that used only the identity to estimate the albedo. This architecture was trained during a fix number of epochs, until the lighting parameters were learnt, and then changed the albedo decoder by a CNN with skip-connections with the encoder. According to the authors, this allows improving the details of the facial albedo.

Piao et al. [124] argued that training, on the one hand, training the network directly on 2D-3D synthetic pairs causes the network to have trouble dealing with real images, due to the gap between synthetic and real data. On the other hand, training the network in a self-supervised manner is likely to overfit. To overcome this, Piao et al. [124] used a cycle-consistent GAN (CycleGAN) [181] to

transform realistic 2D images to synthetic-style images, which were then processed by an encoder-decoder network to estimate position UV-maps of the 3D face, similarly to Feng et al. [111] (see Section 5.2.3). A CycleGAN consists of two GANs concatenated forming a cycle. More in detail, consider a GAN formed by a generator $G_r : \mathcal{S} \rightarrow \mathcal{R}$ that maps a synthetic image \mathbf{I}_s to a real image \mathbf{I}_r , and a discriminator D_r that estimates the probability of an image $\mathbf{I} \in \mathcal{R}$ of being an actual real image and not one generated by G_r . Analogously, we can define its “inverse” GAN, which is formed by the generator $G_s : \mathcal{R} \rightarrow \mathcal{S}$ and the discriminator D_s . Then, the whole end-to-end trainable network is:

$$\mathbf{I}_r \xleftarrow{G_s} \mathbf{I}_s \xrightarrow{\text{Enc-Dec}} \text{Facial position UV-map.} \quad (13)$$

According to the authors, mapping the realistic images to a synthetic-style facilitates the shape estimation process of the 3D face reconstruction network.

5.2.5. Multiple Networks for Different Tasks

In this section, we group the approaches that use multiple networks, where each one is trained for different tasks. These approaches can be divided into three main blocks: multi-stage systems, coarse-to-fine systems, and networks with multiple-branches.

A multi-stage system consists in training multiple networks to estimate different parameters in a sequential manner. Sengupta et al. [109], Bhagavatula et al. [96] and Tewari et al. [141] used a CNN to extract features from the input image(s) and considered multiple networks to estimate different parameters from the CNN’s output. However, whereas the input in [109, 96] is a single image, Tewari et al. [141] used four frames from a video. Sengupta et al. [109] used two different residual blocks to learn to separate low and high frequency variations into normals and albedo (separately). Then, the output of the two residual blocks and the input image were jointly used to learn the lighting parameters. Bhagavatula et al. [96] estimated the warping parameters from a template to the input image and the projection parameters using different fully connected networks. Then, the 3D face was built using the estimated parameters, and 3D landmarks were projected into the image. Finally, the projected 3D landmarks were refined by extracting features from each of them and estimating their offset with a fully connected layer. On the other hand, Tewari et al. [141] used a Siamese CNN to extract features from the input frames. These features are fed into a CNN, which averages them and estimates the shape and albedo parameters, common to all the frames. Also the per-frame parameters (pose, illumination, and expression) are estimated with another Siamese CNN using as input the features of the frame and the shape and albedo parameters. However, the main contribution of [110] is that the shape and albedo models were learnt in the training stage, constructing facial models. Then, in the test

step, only the model parameters are regressed.

Unlike the above works, where each network regresses different features from the input image, Shu et al. [150] proposed a main network that estimated a depth map and two additional networks that helped regularise the output of the main network. First, a DenseNet [182] was trained to estimate the 3DMM shape and expression parameters and the projection parameters. Once trained, this network was fixed and used to regularise the output depth map estimated by the main network, a U-Net network [170]. This network was trained with images whose ground truth depth map is known, but also with pairs of unlabelled images taken at the same time instance from different points of view. According to the authors, this type of data allows generalising to unseen real images, but ensuring photo-consistency directly on the multi-view images is not possible since the same anatomical point may have different pixel colours in both images due to lighting. For this reason, they trained another network (at the same time as the main one) to predict the suitability of each pixel to be used in the multi-view photo-consistency loss, giving more weight to those pixels whose colours do not change much between images.

A coarse-to-fine system successively refines the output of the first network with a second network, each of them specifically trained to estimate a coarse 3D face and fine-level details, respectively. This approach was followed by [143, 100, 18, 19, 129, 139, 140, 146, 148]. Fan et al. [143] first estimated a personalised template and then refined it by estimating an update using a network based on the 50-layer ResNet [169]. The personalised template is initially estimated by fitting a 3DMM to the input image, then each vertex of the initial template is refined by different 1-layer multi-layer perceptron (MLP) networks. These MLP take into consideration not only the vertex in question but also a neighbourhood, together with their colours extracted by projecting the template into the input image.

Wang et al. [146], Richardson et al. [100], Tran et al. [19] and Chen et al. [148] also proposed to use two different networks, one that estimated the coarse 3D face (coarse network) and the other one that refined it (fine network). All of them obtained the coarse 3D face by regressing parameters of a 3DMM. The coarse networks of the first three works [146, 100, 19] was based in the ResNet network [169], whereas the latter [148] trained the VGG-Face [183] architecture. Unlike the other works, Richardson et al. [100] estimated the 3DMM and rendering parameters in the fine network iteratively by adding a feedback channel.

Wang et al. [146] converted the parameters into a normal map, which, together with the input image(s), was the input of the fine network. In the refinement stage, the normal map is processed by a 4-layer CNN encoder, and so are the input images, but in this case the encoders share their weights. The features extracted from the normal map and the input images are passed to a 5-layer CNN decoder that estimates the refined normal map. In contrast, Richardson et al. [100] converted the resulting parameters into a

depth map, which was the input of the fine network based on the hypercolumn architecture [184] with the VGG-Face network [183] as a base. This work [100] inspired Guo et al. [18] to apply the coarse-to-fine framework to videos instead of single images. To do so, they included a tracking coarse network that predicted the next frame’s coarse parameters.

On the other hand, Tran et al. [19] and Chen et al. [148] represented the fine details as a displacement map from the coarse face, and both used the image-translation network proposed by Isola et al. [185]. Tran et al. [19] computed the ground truth displacements maps with [186], whereas Chen et al. [148] added a rendering layer to train the network in a self-supervised manner. More specifically, the fine network from [148] inputs two UV-texture maps, one extracted from the input image and the other extracted from the albedo estimated with the coarse network, and estimates a displacement map. To train this network, the refined textured 3D face was rendered to generate a synthetic image that was compared to the input image.

Differently from the other authors that proposed a coarse-to-fine scheme, Zeng et al. [129], Wang et al. [140] and Lattas et al. [139] stacked three different networks. Zeng et al. [129] trained each of them to refine the depth map estimated by the previous network by taking into account also the input image. The coarse network is a U-Net [170], whereas the fine and the finer networks are CNNs based on the hypercolumn architecture [184] with 9 and 16 layers, respectively. The first two networks were trained in a fully supervised manner, whereas the last one was self-supervised. In contrast, Wang et al. [140] and Lattas et al. [139] reconstructed photo-realistic 3D faces by refining the texture estimated by a 3DMM fitting-based approach, instead of refining directly the geometry. Wang et al. [140] computed the 3D facial normals and an UV texture map from the coarse 3D facial shape. First, with a 18-layers ResNet [169] network, they estimated the texture and illumination parameters modelled by a 3DMM and spherical harmonics (see eq. (11)), respectively. These parameters are then used to train a U-Net-based [170] network to translate the texture UV map into an albedo UV map, which is then used to train another U-Net-based network to refine the coarse 3D face by estimating per-vertex displacements. In contrast, Lattas et al. [139] refined the output from [64] by inferring the diffuse and specular albedo and normals, which are then used to improve the reconstructed 3D face. First, the texture UV map estimated by [64] is enhanced with a super resolution network [187], then an image-to-image network [151] is trained to estimate the diffuse albedo by removing the illumination from the enhanced UV texture map. Finally, another 3 image-to-image networks [151] are trained to infer the specular albedo, specular and diffuse normals.

Finally, the third block is composed of approaches whose architectures have multiple parallel networks that process the input image to estimate different attributes. Alp Güler et al. [98] and Dou et al. [97] attached different branches

to a main network where each of them estimates different parameters. Alp Güler et al. [98] proposed to add branches at the end of a ResNet-based network [169] to separately estimate the U- and the V-coordinates of an UV-map. In contrast, the network proposed by Dou et al. [97] has a “sub-CNN” that combines features from intermediate layers of the VGG-Face network [183]. This sub-CNN estimates expression-specific features while the main network, the VGG-Face, estimates the identity-specific features. Both types of features are then combined to form a 3D face.

On the other hand, Chai et al. [142] proposed to process the input image by two separate streams: one to estimate the shape and the other to estimate the texture. The shape stream is an encoder-decoder architecture: the VGGNet [165] extracted features from the image, which are decoded by two 5-layers (transposed) CNNs to estimate identity and expression attributes, respectively. These attributes are added to construct the final 3D shape. In addition, the features extracted by the encoder are passed through two fully-connected layers to estimate the pose, illumination, and albedo parameters, these last ones modelled by a 3DMM. The texture stream basically consists of a style transfer network, where the style of the input image is transferred to the albedo modelled by the 3DMM. First, another VGGNet [165] processes the sampled visible face region from the input image. Then, the output of this VGGNet, together with the estimated albedo, are passed as input to a 16-layers CNN containing residual blocks to estimate a realistic skin-style texture map. Finally, the estimated shape, texture, pose, and illumination are used to render a synthetic image that is used to train the network.

5.3. Training criterion

Another decisive element for the learning is the training criterion, i.e the loss function (also called cost or error function) minimised by the network in the training process. Evidently, this loss function depends directly on the output of the network since, roughly, the weights of the network are learnt to minimise the error between the estimated output and the ground truth.

Most of the works presented above estimate the parameters of a 3DMM from the input image. Among them, a popular term included in the cost function is the error between the estimated and the ground truth parameters [112, 94, 95, 108, 109, 105, 19, 92, 114].

Tran et al. [105, 19] found that the Euclidean loss favours estimates closer to the origin, resulting in faces closer to the mean face, thus less detailed. To avoid this, they used the *asymmetric Euclidean loss*, which decouples the over-estimation and under-estimation errors (first and second terms in eq. (14), respectively), favouring recon-

structions further away from the mean

$$\begin{aligned} \mathbb{E}_{\text{asym}}(\theta, \theta_{\text{gt}}) &= \\ &= w_1 \|\text{abs}(\theta_{\text{gt}}) - \max(\text{abs}(\theta), \text{abs}(\theta_{\text{gt}}))\|_2^2 + \\ &w_2 \|\text{abs}(\theta) - \max(\text{abs}(\theta), \text{abs}(\theta_{\text{gt}}))\|_2^2, \end{aligned} \quad (14)$$

where $\text{abs}(\cdot)$ and $\max(\cdot)$ are defined for each element of the vector of estimated parameters θ and the vector of ground truth parameters θ_{gt} . The weights $w_1, w_2 \in \mathbb{R}$ control the trade-off between the over- and under-estimation errors. In addition, in [19] they included a loss function to learn to predict the bump map $\Gamma(x, y)$ defined as a displacement for each pixel (x, y) in the input image, that refines the 3D face estimated by [105]. This *bump loss* computes the error of the estimated bump map, including the difference between the gradient of the estimated and the ground truth bump maps to favour smoother surfaces

$$\begin{aligned} \mathbb{E}_{\text{bump}}(\Gamma, \Gamma_{\text{gt}}) &= \|\Gamma - \Gamma_{\text{gt}}\|_1 + \left\| \frac{\partial \Gamma}{\partial x} - \frac{\partial \Gamma_{\text{gt}}}{\partial x} \right\|_1 + \\ &\left\| \frac{\partial \Gamma}{\partial y} - \frac{\partial \Gamma_{\text{gt}}}{\partial y} \right\|_1. \end{aligned}$$

5.3.1. Weighted Parameters Errors

Kim et al. [108], Jourabloo et al. [103], Zhu et al. [92, 114], Tu et al. [145], Guo et al. [135] and Genova et al. [112] used a *weighted parameters distance cost*, which computes the Euclidean distance between θ and θ_{gt} , but with weighting factors for each parameter to balance their global importance:

$$\mathbb{E}_{\text{wpdc}}(\theta, \theta_{\text{gt}}) = (\theta - \theta_{\text{gt}})^T \mathbf{W} (\theta - \theta_{\text{gt}}). \quad (15)$$

The main difference between each of these works is the weighting matrix. Kim et al. [108] proposed to use a weight matrix $\mathbf{W} = \Sigma^T \Sigma$ where Σ is a diagonal matrix with weights that incorporate the standard deviation of each parameter, σ_i , $\Sigma = \text{diag}(\sigma_1 w_1, \dots, \sigma_K w_K)$, where the w_i are empirically determined by the authors. Similarly, the weight matrix used by Jourabloo et al. [103] is a diagonal matrix with the inverse of the standard deviations of each parameter, $\mathbf{W} = \text{diag}\left(\frac{1}{\sigma_1}, \dots, \frac{1}{\sigma_K}\right)$, which normalises the importance of each element in the loss function.

As described in Section 5.2.2, Zhu et al. [92, 114] used a cascaded regressor approach to iteratively estimate the parameters update $\Delta\theta^k$ to move the initial parameters θ^0 closer to the θ_{gt} . Thus, the cost function in eq. (15) is slightly modified to

$$\mathbb{E}_{\text{wpdc}}(\Delta\theta, \Delta\theta_{\text{gt}}) = (\Delta\theta - \Delta\theta_{\text{gt}})^T \mathbf{W} (\Delta\theta - \Delta\theta_{\text{gt}})$$

where $\Delta\theta_{\text{gt}} = \theta_{\text{gt}} - \theta^0$. In both works, the weight matrix is a diagonal matrix $\mathbf{W} = \text{diag}(\mathbf{w})$, $\mathbf{w} = (w_1, \dots, w_K)$. Zhu

et al. [92] defined the weights w_i , $i = 1, \dots, K$ as

$$w_i = \frac{\left\| \mathcal{P}(\mathbf{x}(\tilde{\theta}^{[i]}), \tilde{\theta}^{[i]}) - \mathcal{P}(\mathbf{x}(\theta_{\text{gt}}), \theta_{\text{gt}}) \right\|_2}{\sum_{k=1}^K w_k}. \quad (16)$$

Here, $\tilde{\theta}^{[i]}$ defines the vector of parameters where the i th element comes from the estimated parameter $\tilde{\theta}_i^{[i]} = \theta_i$, whereas the rest come from the ground truth $\tilde{\theta}_j^{[i]} = \theta_{j,\text{gt}}$, $\forall j \neq i$. $\mathbf{x}(\theta)$ defines the 3D facial shape built with the shape and expression parameters from θ , and $\mathcal{P}(\mathbf{x}(\theta), \theta)$ defines the projection of $\mathbf{x}(\theta)$ according to the projection parameters in θ . On the other hand, Zhu et al. [114] proposed to optimise the weights in each iteration

$$\begin{aligned} \mathbf{w}^* = \arg \min_{\mathbf{w}} & \left\| \mathcal{P}(\mathbf{x}(\check{\theta}), \check{\theta}) - \mathcal{P}(\mathbf{x}(\theta_{\text{gt}}), \theta_{\text{gt}}) \right\|_2^2 \\ & + \lambda \left\| \text{diag}(\mathbf{w})(\theta - \theta_{\text{gt}}) \right\|_2^2 \\ \text{s.t. } & 0 \leq w_i \leq 1, \quad \forall i \end{aligned}$$

where $\check{\theta} = \theta + \text{diag}(\mathbf{w})(\theta - \theta_{\text{gt}})$ and $\lambda \in \mathbb{R}$. According to the authors, adding the weighted updated $\text{diag}(\mathbf{w})(\theta - \theta_{\text{gt}})$ to the current estimated parameters θ allowed estimating a new face closer to the ground truth face, thus improving the final result.

Tu et al. [145] and Guo et al. [135] proposed a weighting matrix highly based on that of [92] (eq. 16). Whereas the former [145] only computed the projection of the landmarks, rather than projecting the whole facial reconstruction $\mathbf{x}(\theta)$, Guo et al. [135] computed the distance between the 3D faces directly and normalised the weights by their maximum value:

$$w_i = \frac{\left\| \mathbf{x}(\tilde{\theta}^{[i]}) - \mathbf{x}(\theta_{\text{gt}}) \right\|_2}{\max \{w_k\}_{k=1}^K}.$$

In contrast to the previous works, Genova et al. [112] used a common weight for all the parameters of the same space, i.e., one weight for the shape parameters and another one for the texture parameters. Additionally, they used other two terms: identity loss and batch distribution loss. The first one ensures that the ID-features \mathbf{f} extracted from a real input image and from the image rendered using the parameters estimated by the decoder over the real input image are similar, and it is computed based on cosine similarity: $\mathbb{E}_{\text{id}}(\mathbf{f}_i, \mathbf{f}_j) = \mathbf{f}_i \cdot \mathbf{f}_j$. The batch distribution loss is a regularisation term applied at a batch level rather than to the whole training set, which enforces the estimated parameters to match a zero-mean standard normal distribution, assumed by the 3DMM.

5.3.2. L_p Norms in the Parameters Space

Wu et al. [122], Yoon et al. [125], Jourabloo and Liu [94, 95], Sengupta et al. [109], Chaudhuri et al. [132] and Shu et al. [150] used a loss function over the parameters that consisted simply in computing the L_p norm of the

difference between the estimated and ground truth parameters (raised to p th power):

$$\mathbb{E}_{p\text{-norm}^p}(\theta, \theta_{\text{gt}}) = \|\theta - \theta_{\text{gt}}\|_p^p = \sum_{i=1}^K |\theta_i - \theta_{i,\text{gt}}|^p. \quad (17)$$

Chaudhuri et al. [132] used the L_1 norm to compute the parameters error, together with a landmarks error term. On the other hand, Chai et al. [142], Wu et al. [122], Yoon et al. [125], Jourabloo and Liu [94, 95], and Shu et al. [150] used the L_2 norm. The first authors [132] used it to estimate the pose, illumination and texture parameters, as well as the identity and expression attributes of the shape stream (see Section 5.2.5). [122, 125] used it to pre-train their network in a fully supervised-manner, and [94, 95] estimated the update of the parameters in the cascaded CNN they proposed. Thus, for Jourabloo and Liu [94, 95], in eq. (17), θ_{gt} is the ground truth update (difference between current estimate and ground truth parameters), and θ is the update estimated by the current CNN. In addition, Jourabloo and Liu [95] also estimated the location of the 2D landmarks in the input face; thus they included a landmark term that ensures the landmarks on the input face are similar to the landmarks on the mirrored image (with a reordering). This term minimises the L_2 norm of the difference between the projected landmarks over the original image and over the mirrored image. Similarly, Wu et al. [122], Yoon et al. [125] and Shu et al. [150] added a landmark term, but they minimised the distance between the landmarks on the input image and the projection of the landmarks of the estimated 3D face. In addition, Shu et al. [150] ensured consistency in the parameters estimated from images taken simultaneously but from different points of view by minimising their difference.

Sengupta et al. [109] used a loss function composed of four terms $\mathbb{E} = w_{\mathbf{n}}\mathbb{E}_{\mathbf{n}} + w_{\beta}\mathbb{E}_{\beta} + w_{\mathbf{I}}\mathbb{E}_{\mathbf{I}} + w_{\gamma}\mathbb{E}_{\gamma}$. The error over the lighting parameters γ was computed using a L_2 norm, whereas the first three terms, namely, the error over the surface normals \mathbf{n} , the error over the 3DMM texture parameters β , and the image error were computed using the L_1 norm:

$$\begin{aligned} \mathbb{E}_{\gamma}(\gamma, \gamma_{\text{gt}}) &= \|\gamma - \gamma_{\text{gt}}\|_2, \\ \mathbb{E}_{\mathbf{n}}(\mathbf{n}, \mathbf{n}_{\text{gt}}) &= \|\mathbf{n} - \mathbf{n}_{\text{gt}}\|_1, \end{aligned} \quad (18)$$

$$\begin{aligned} \mathbb{E}_{\beta}(\beta, \beta_{\text{gt}}) &= \|\beta - \beta_{\text{gt}}\|_1, \\ \mathbb{E}_{\mathbf{I}}(\mathbf{I}_{\text{mod}}, \mathbf{I}_{\text{in}}) &= \|\mathbf{I}_{\text{mod}} - \mathbf{I}_{\text{in}}\|_1. \end{aligned} \quad (19)$$

The image error $\mathbb{E}_{\mathbf{I}}$ was defined as the L_p norm of the per-pixel difference between the input image \mathbf{I}_{in} and the image rendered with the estimated parameters \mathbf{I}_{mod} . Whereas Sengupta et al. [109], Tran and Liu [34], Zhou et al. [117] and Deng et al. [121] used a L_1 norm as in eq. (19), [102, 110, 113, 100, 115, 116, 122, 127, 133] computed the image error using the Euclidean distance (L_2 norm).

5.3.3. Self-Supervision

Unlike the above works, Tewari et al. [102, 110, 113, 141], Tran and Liu [34, 115], Tran et al. [116], Deng et al. [121], Savov et al. [127], Chaudhuri et al. [133], Chen et al. [148], Shang et al. [137], Gao et al. [149] used the image error to drive the learning in a self-supervised manner by training the network to produce 3D faces whose rendered images are similar to the input images. They used the self-supervision over the whole reconstruction process. Therefore, to further constrain the training, they added a 2D landmarks error to the loss function:

$$\mathbb{E}_{\text{lmk2D}} = \sum_{i=1}^L \left\| \ell_i^{2\text{D}} - \hat{\ell}_i^{2\text{D}} \right\|_2^2, \quad (20)$$

where $\ell^{2\text{D}}$ are the landmarks in the input image and $\hat{\ell}^{2\text{D}}$ the projection of the landmarks onto the 3D face. Also, Chen et al. [148] further ensured the image similarity by minimising the difference between the image features extracted using the pre-trained VGG-Face network [183] from the input and the rendered image.

In addition, the estimated parameters have to be regularised to ensure the reconstruction of realistic 3D faces. Tewari et al. [102, 110, 113], Chen et al. [148], Savov et al. [127] and Shang et al. [137] used a statistical regularisation term. Tewari et al. [141] also used statistical regularisation but only for the expression parameters, since the expression model is the only one not learnt during training. They regularised the shape and albedo by adding a smoothness term for both of them.

As explained in Section 5.2.1, Shang et al. [137] used two additional adjacent images to improve the quality of the final reconstruction. Thus, they added an image consistency loss that is defined as

$$\mathbb{E}_{\text{px consistency}}(\hat{\mathbf{I}}_{\text{mod}}, \mathbf{I}_{\text{in}}) = \frac{1}{|\mathcal{I}|} \sum_{i \in \mathcal{I}} \left\| \mathbf{I}_{\text{in}}(i) - \hat{\mathbf{I}}_{\text{mod}}(i) \right\|_1$$

where $\hat{\mathbf{I}}_{\text{mod}}$ is the synthesised target image from the adjacent image, $\mathbf{I}(i)$ represents the i th pixel value of \mathbf{I} and \mathcal{I} is the set of pixels jointly visible in the target and the adjacent images.

On the other hand, Chaudhuri et al. [133] regularised the parameters with L_1 loss, in addition to two terms that ensured smooth shape deformations. Tran and Liu [34] added an adversarial loss, training a discriminator network to distinguish between real images and rendered images while training the generator to produce more realistic faces. In their latter work, Tran and Liu [115] stated that the adversarial loss does not encourage the rendered image to be similar to the input image, but only to be close to the distribution of real images. To solve this issue, they proposed a perceptual loss to enforce similar feature representations of both the rendered and the input image as

computed by a feature extraction function φ :

$$\mathbb{E}_{\mathbf{I}, \varphi}(\mathbf{I}_{\text{mod}}, \mathbf{I}_{\text{in}}) = \frac{1}{|\mathcal{C}|} \sum_{j \in \mathcal{C}} \frac{\|\varphi_j(\mathbf{I}_{\text{mod}}) - \varphi_j(\mathbf{I}_{\text{in}})\|_2^2}{W_j H_j C_j}. \quad (21)$$

They chose φ to be the VGG-Face network [183], thus $\varphi_j(\mathbf{I})$ is the activation of the j th layer of the VGG-Face network when processing \mathbf{I} with dimension $W_j \times H_j \times C_j$. \mathcal{C} is a subset of layers of the network. The image error used by Tran and Liu [115] is then a combination of the image error as in eq. (19) (using the L_2 norm) and the features error as in eq. (21). Finally, they added three regularisation terms: albedo symmetry and albedo constancy and shape smoothness within a neighbourhood. Tran et al. [116] claimed that the strong regularisations used by Tran and Liu [115] prevented the network from estimating high-level details and proposed another strategy to regularise the resulting shapes and textures. Such strategy consisted in applying the strong regularisation to auxiliary shapes and albedos and regularising the original ones by imposing similarity between them.

Similarly to Tran and Liu [115], Deng et al. [121] used the L_1 image error (eq. (19)), the landmarks error (eq. (20)) and a perceptual loss, which, in this case, was defined as the cosine distance between features extracted using the FaceNet [177] from \mathbf{I}_{in} and \mathbf{I}_{mod} ,

$$\mathbb{E}_{\mathbf{I}, \varphi}(\mathbf{I}_{\text{mod}}, \mathbf{I}_{\text{in}}) = 1 - \frac{\varphi(\mathbf{I}_{\text{in}})^T \varphi(\mathbf{I}_{\text{mod}})}{\|\varphi(\mathbf{I}_{\text{in}})\|_2 \|\varphi(\mathbf{I}_{\text{mod}})\|_2}. \quad (22)$$

Finally, they added statistical regularisation for all the estimated parameters. In addition, they proposed an approach to reconstruct the 3D face of a subject given multiple images. They observed that the shape parameters should be the same across different images, but that the rest of them depend on each image. Thus, they jointly trained a CNN to estimate a positive value measuring the confidence of the shape parameters for each of the images and used these confidences to compute the final shape parameters.

Like in the previous works, Wu et al. [122] and Yoon et al. [125] trained their network in a self-supervised manner using an image error and a landmarks error. However, since they reconstructed the 3D face of a subject from several images, they adapted the image error. As described in Section 5.2.1, Wu et al. [122] used three images (frontal, left, and right views), thus their image error takes into account the difference between several pairs of images:

$$\mathbb{E}_{\mathbf{I}} = \left\| \mathbf{I}_{\text{in}}^B - \mathbf{I}_{\text{mod}}^{A \rightarrow B} \right\|_2^2 + \left\| \mathbf{I}_{\text{in}}^B - \mathbf{I}_{\text{mod}}^{C \rightarrow B} \right\|_2^2 + \left\| \mathbf{I}_{\text{in}}^A - \mathbf{I}_{\text{mod}}^{B \rightarrow A} \right\|_2^2 + \left\| \mathbf{I}_{\text{in}}^C - \mathbf{I}_{\text{mod}}^{B \rightarrow C} \right\|_2^2 \quad (23)$$

where \mathbf{I}_{in}^A , \mathbf{I}_{in}^B , and \mathbf{I}_{in}^C are the three input images (right, frontal, and left, respectively), and $\mathbf{I}_{\text{mod}}^{i \rightarrow j}$ represents the estimated 3D face coloured with image \mathbf{I}_{in}^i projected into \mathbf{I}_{in}^j . However, the authors stated that using only the image

error does not ensure good alignment between the input and the rendered images, thus they proposed an alignment term that minimised the flow between them

$$\mathbb{E}_{\text{align}}(\mathbf{I}_{\text{in}}^B, \mathbf{I}_{\text{mod}}^{A \rightarrow B}) = \sum_{\mathbf{p}} \left(\left\| \mathcal{F}(\mathbf{I}_{\text{mod}}^{A \rightarrow B}(\mathbf{p}), \mathbf{I}_{\text{in}}^B(\mathbf{p})) \right\|_2^2 + \left\| \mathcal{F}(\mathbf{I}_{\text{in}}^B(\mathbf{p}), \mathbf{I}_{\text{mod}}^{A \rightarrow B}(\mathbf{p})) \right\|_2^2 \right)$$

where $\mathcal{F}(\mathbf{I}^i(\mathbf{p}), \mathbf{I}^j(\mathbf{p}))$ is the optical flow from \mathbf{I}^i to \mathbf{I}^j at pixel \mathbf{p} estimated using [188]. This alignment error was computed for the same pairs of images as in the image error (eq. (23)):

$$\mathbb{E}_{\text{align}} = \mathbb{E}_{\text{align}}(\mathbf{I}_{\text{in}}^B, \mathbf{I}_{\text{mod}}^{A \rightarrow B}) + \mathbb{E}_{\text{align}}(\mathbf{I}_{\text{in}}^B, \mathbf{I}_{\text{mod}}^{C \rightarrow B}) + \mathbb{E}_{\text{align}}(\mathbf{I}_{\text{in}}^A, \mathbf{I}_{\text{mod}}^{B \rightarrow A}) + \mathbb{E}_{\text{align}}(\mathbf{I}_{\text{in}}^C, \mathbf{I}_{\text{mod}}^{B \rightarrow C}).$$

Shu et al. [150] also used a multi-view photo-consistency loss very similar to [122] (eq. (23)) but with two images instead of three. However, they stated that the same anatomical point may not have the same pixel colour across the different images. Therefore, to account for this issue, they added a suitability map $\mathbf{S}(\mathbf{I}_{\text{in}}^A)$ estimated from \mathbf{I}_{in}^A by another network that weighted the suitability of a pixel to be used for computing the photo-consistency loss:

$$\mathbb{E} = \left\| \mathbf{S}(\mathbf{I}_{\text{in}}^A) \odot \mathbf{M} \odot (\mathbf{I}_{\text{in}}^A - \mathbf{I}_{\text{mod}}^{B \rightarrow A}) \right\|$$

where \mathbf{M} is the occlusion mask to account for the common visible face region and \odot the Hadamard product.

On the other hand, Yoon et al. [125] used 2D videos as input and, thus, added a texture consistency term that ensured the recovered 3D texture did not change much along consecutive frames.

Differently from the previous self-supervised works that used both the image and the landmarks errors (eqs. (19) and (20)) to train their networks, Chai et al. [142], Wang et al. [140], Lin et al. [136], Koizumi and Smith [138], Zhou et al. [117], Sanyal et al. [118], Wang et al. [126] only considered one of them: [140, 136, 138, 117, 142] used only the image error, whereas Sanyal et al. [118] and Wang et al. [126] employed the landmarks errors. Given that both trained their networks in a self-supervised manner, only one of those error functions is not sufficient to drive the training process, and thus they added other losses to constrain it.

Chai et al. [142] and Wang et al. [140] trained multiple networks to estimate different attributes of the 3D face (see Section 5.2.5): the first estimated separately the shape and the texture, whereas the latter trained three different networks that use the previous one to refine the reconstruction. Chai et al. [142] trained in a self-supervised manner only the texture stream to transferred the style of the face region in the input image to the texture modelled by a 3DMM, obtaining a realistic skin texture \mathbf{T}_{out} . The 3DMM texture parameters are estimated in the shape stream, which was trained in a fully-supervised manner.

The texture stream was trained using an image error of the visible facial regions and the cosine distance (eq. (22)) between id-features extracted from ArcFace [71]. In addition, the style transfer was ensured by including a perceptual and style losses. The perceptual loss was computed as in eq. (21) but between the 3DMM texture and the output transferred texture, \mathbf{T}_{out} , and using φ as the VGGNet [165]. The style loss was computed as

$$\mathbb{E}_{\text{style}}(\mathbf{T}_{\text{in}}^{\text{face}}, \mathbf{T}_{\text{out}}) = \frac{1}{|\mathcal{C}|} \sum_{j \in \mathcal{C}} \left\| \mathbf{G}_j^\varphi(\mathbf{T}_{\text{in}}^{\text{face}}) - \mathbf{G}_j^\varphi(\mathbf{T}_{\text{out}}) \right\|_{\text{F}}^2,$$

where \mathcal{C} is a subset of layers of the VGGNet [165] represented as φ , $\mathbf{T}_{\text{in}}^{\text{face}}$ is the visible facial regions of the input image, and $\|\cdot\|_{\text{F}}$ is the Frobenius norm. $\mathbf{G}_j^\varphi(\mathbf{I})$ is the Gram matrix defined as

$$\mathbf{G}_j^\varphi(\mathbf{I}) = \frac{\hat{\varphi}_j(\mathbf{I})^T \hat{\varphi}_j(\mathbf{I})}{W_j H_j C_j},$$

where $\hat{\varphi}_j(\mathbf{I})$ is the activation of the j th layer of φ (whose shape is $W_j \times H_j \times C_j$) reshaped into a 2D matrix of dimension $W_j H_j \times C_j$, for an input image \mathbf{I} .

On the other hand, Wang et al. [140] trained their first network to estimate the albedo β and illumination parameters with an L_1 image error term and a L_2 regularisation term over β . Their second network was trained to estimate an albedo UV map with an adversarial loss, an image error, and a perceptual loss (eq. (21)), similar to [115]. Finally, their third network, which estimates per-vertex displacement from the coarse 3D face, was trained with the L_1 norm of the difference between the gradient of the input and the rendered images, claiming that using the gradients of the images forces the networks to focus on geometric details. The displacements were regularised with two terms, one that ensured small values and another that ensured similarity between displacements of neighbouring vertices. Similarly to [115] and the second network of [140], Lin et al. [136] trained a GAN architecture to refine the 3D facial texture (see Section 5.2.4) with a loss function that consisted of: the L_2 image error computed over the facial region, the perceptual loss from [121] (eq. (22)), the L_2 norm of the per-vertex difference between the coarse and the refined texture, and an adversarial loss. On the other hand, Koizumi and Smith [138] trained the U-Net [170] to build a correspondence map between the input image and a 3DMM, with which the 3DMM and rendering parameters are estimated using least squares and a rendering layer. Thus, apart from an image error, they computed the least squares residuals so as to train the network to obtain a correspondence map that allows the LS layer to reconstruct accurate 3D faces. Also, the 3DMM parameters and intrinsic camera parameters are regularised: the first statistically and the latter by penalising different vertical and horizontal focal lengths and shear.

As explained in Section 5.2.3, Zhou et al. [117] proposed an architecture with two encoders that share a sim-

gle decoder, leading to two streams: one mesh-to-mesh, where the input of the encoder is a 3D coloured mesh; and another one image-to-mesh, where the input of the encoder is a 2D image. They jointly trained both streams by linearly combining a reconstruction error for the mesh-to-mesh, defined as the norm of the difference between the input coloured mesh and the estimated coloured mesh; and an image error for the image-to-mesh stream. This joint training procedure allowed the authors to constrain the self-supervision on the image-to-mesh stream. Liu et al. [107] followed a similar idea: they trained a mesh-to-mesh autoencoder network where the decoder extracted features from the input mesh and the decoders recovered the 3D face (see Section 5.2.3). Once trained, the decoders may be stacked to the SphereFace network [176], that acts as encoder extracting features from images, to form a 3D-from-2D face reconstruction encoder-decoder network. The mesh-to-mesh network was trained in both self-supervised and supervised manner (see Section 5.1) with cost functions that consisted of per-vertex Euclidean distance between the input and the output, the cosine distance between their normals, and a term that encourages the edges lengths to be similar between the input mesh and the reconstruction:

$$\mathbb{E}_{\text{edge-length}} = \frac{1}{|\mathcal{E}|} \sum_{(i,j) \in \mathcal{E}} \left| 1 - \frac{\|\mathbf{x}_i^{\text{out}} - \mathbf{x}_j^{\text{out}}\|}{\|\mathbf{x}_i^{\text{in}} - \mathbf{x}_j^{\text{in}}\|} \right|$$

where \mathcal{E} is the set of edges, \mathbf{x}_i^{in} is the i -th vertex of the input mesh (respectively for the output mesh \mathbf{x}^{out}).

On the other hand, whereas Wang et al. [126] combined several landmarks databases to increase the number of anchor points, Sanyal et al. [118] proposed to feed the network with subsets of R images during training, where $R - 1$ of these images were of the same person and the R th image belonged to a different person. This subset of images allowed the authors to impose shape consistency among the reconstructions of the same person, while imposing them to be different from the reconstruction of the “other person”. This shape consistency constraint was mathematically expressed as

$$\|\alpha_i - \alpha_j\|_2^2 + \eta \leq \|\alpha_i - \alpha_R\|_2^2 \quad (24)$$

for all $i, j = 1, \dots, R - 1, i \neq j$ and some $\eta \in \mathbb{R}$, where α_i is the estimated shape parameters vector of a 3DMM for the i th image. They translated eq. (24) into the loss function

$$\mathbb{E} = \sum_{i,j=1}^{R-1} \max \left(0, \|\alpha_i - \alpha_j\|_2^2 + \eta - \|\alpha_i - \alpha_R\|_2^2 \right).$$

Contrary to the other works, which used self-supervision to train their 3D-from-2D reconstruction network, Richardson et al. [100] used self-supervision to train a network to refine the depth map estimated by the coarse network, \mathbf{z}_c (trained only using the Euclidean loss). They ap-

plied a loss function that consisted of three terms. Apart from the image error explained above, a fidelity term was added to ensure that the refined map is similar to the coarse depth map, $\mathbb{E}_{\text{fidel}}(\mathbf{z}) = \|\mathbf{z} - \mathbf{z}_c\|_2^2$. Also, a smoothness term prevents the gradient of the map to be too large, $\mathbb{E}_{\text{smooth}} = \|\Delta z\|_1$, where Δ is the Laplacian operator. Similarly, Tewari et al. [113] carried out a refinement of the 3D face resulting from the network by estimating per-vertex displacements in an optimisation-based manner. To do so, they proposed to minimise a loss function consisting in three terms: an image error, a gradient matching term, that ensures matching colour gradients between the input and the rendered image (within a neighbourhood), and a regularisation term, which ensures the displacements to be similar within a neighbourhood.

5.3.4. Loss Functions in the 3D Space

Another loss function that was used is the Euclidean distance over the 3D faces directly [96, 97, 106, 93, 100, 123, 129, 130, 131, 134, 135, 143, 144, 146, 147, 149]. [96, 106, 134, 130, 143, 147, 144, 149] outputted the regressed 3D face, whereas [97, 93, 100, 131, 135, 123, 146] outputted 3DMM parameters. Thus, to apply the Euclidean loss to the 3D faces, first the 3D geometry (and texture in some cases) have to be recovered by multiplying the model basis to the estimated parameters. In addition, Chinaev et al. [131] included the L_2 norm between the projection to the image plane of the ground truth and the reconstructed 3D faces, and Gao et al. [149], Guo et al. [135] and Wang et al. [146] included the L_2 norm between the ground truth 2D landmarks and the projection of the estimated 3D landmarks. Also, Wang et al. [146] added an angular distance between the estimated and the ground truth normals, $\frac{1}{|\mathcal{I}|} \sum_{i \in \mathcal{I}} 1 - \mathbf{n}_i^T \mathbf{n}_{i,\text{gt}}$; and Li et al. [144] added the cross-entropy loss to obtain more robust identity-features.

Gao et al. [149] trained their network with unlabelled images in a self-supervised manner (Section 5.3.3), but also with images with corresponding shape α and expression δ 3DMM parameters. For these labelled images, they minimised the difference between the reconstructed $\tilde{\mathbf{x}}$ and the ground truth $\mathbf{x}(\alpha, \delta)$ 3D faces, but also added a term to ensure smooth reconstructions and another term to train the network to disentangle the identity from the expression. The smoothness was ensured by comparing the difference of each vertex in the reconstruction $\tilde{\mathbf{x}}_i$ to its first order neighbours \mathcal{N}_i to that of a template \mathbf{x}^t (the mean of the 3DMM):

$$\mathbb{E}_{\text{smooth}}(\tilde{\mathbf{x}}, \mathbf{x}^t) = \sum_i \left| \left(\tilde{\mathbf{x}}_i - \frac{1}{|\mathcal{N}_i|} \sum_{j \in \mathcal{N}_i} \tilde{\mathbf{x}}_j \right) - \left(\mathbf{x}_i^t - \frac{1}{|\mathcal{N}_i|} \sum_{j \in \mathcal{N}_i} \mathbf{x}_j^t \right) \right|.$$

To train the network to separate the identity from the expression, Gao et al. [149] included a term that swaps

the identity and the expression of two input images \mathbf{I}_A and \mathbf{I}_B from different subjects:

$$\mathbb{E} = \|\mathbf{x}(\alpha^A, \delta^B) - \tilde{\mathbf{x}}(\mathbf{f}_{\text{id}}^A, \mathbf{f}_{\text{exp}}^B)\|_1$$

where $\mathbf{x}(\alpha^A, \delta^B)$ is the 3D face recovered from the shape parameters α^A from \mathbf{I}_A and the expression parameters δ^B from \mathbf{I}_B , and similarly $\tilde{\mathbf{x}}(\mathbf{f}_{\text{id}}^A, \mathbf{f}_{\text{exp}}^B)$ is the decoded 3D face taking the identity features \mathbf{f}_{id}^A estimated by the encoder from \mathbf{I}_A and the expression features $\mathbf{f}_{\text{exp}}^B$ estimated from \mathbf{I}_B . Also, the albedo symmetry was ensured by minimising the difference between the estimated albedo and its flipped version.

Unlike the other works, Yi et al. [123] separated the influence of the shape parameters α and the expression parameters δ to the final facial geometry: $\mathbf{x}(\alpha, \delta)$

$$\mathbb{E}_{\mathbf{x}} = w_{\alpha} \|\mathbf{x}(\alpha, \delta_{\text{gt}}) - \mathbf{x}(\alpha_{\text{gt}}, \delta_{\text{gt}})\|_2^2 + w_{\delta} \|\mathbf{x}(\alpha_{\text{gt}}, \delta) - \mathbf{x}(\alpha_{\text{gt}}, \delta_{\text{gt}})\|_2^2,$$

where α_{gt} and δ_{gt} are the ground-truth shape and expression parameters, respectively. Also, they added a landmarks error computed as the distance between the projection of the landmarks of the ground-truth 3D face $\mathbf{x}(\alpha_{\text{gt}}, \delta_{\text{gt}})$ using the estimated projection parameters and the ground-truth projection parameters.

Also differently from the previous works, Tu et al. [145] proposed a set of three landmark errors to ensure consistency in 3D and in the image plane. The first is the distance between the projected 3D landmarks (from the reconstructed 3D face), $\hat{\ell}^{2D}$, and the ground truth 2D landmarks, ℓ^{2D} . The second is the distance between the 3D landmarks of the estimated 3D face, ℓ^{3D} , and the back-projection of $\hat{\ell}^{2D}$ estimated in the backward pass, $\hat{\hat{\ell}}^{3D}$. Finally, to ensure the consistency of the cycle formed by the forward and the backward pass, they computed the distance between the ground truth 2D landmarks, ℓ^{2D} , and the projection of $\hat{\hat{\ell}}^{3D}$ into the image plane, $\hat{\hat{\ell}}^{2D}$.

As explained in Section 5.2.5, Chen et al. [148] refines a coarse 3D face modelled by a 3DMM by estimating a displacement depth map. To do so, they trained a network in a self-supervised manner by minimising the image error. Although, without further constraints, artefacts and distortions may appear. For this reason, they added a smoothness term that ensured similar estimations in a neighbourhood, and a regularisation term that prevented large displacements. Also in a coarse-to-fine manner, Zeng et al. [129] estimated a depth map from a single image by stacking three networks. Unlike [148], Zeng et al. [129] trained their networks with ground truth reconstructions. Therefore, the coarse network was trained in a fully-supervised manner by minimising the difference between predicted \mathbf{D} and ground-truth \mathbf{D}_{gt} depths maps

$$\mathbb{E}_{\mathbf{D}} = \|\mathbf{D} - \mathbf{D}_{\text{gt}}\|_1. \quad (25)$$

They also included the normals error as in eq. (18) to avoid over-sharpening estimations produced by the L_1 loss in the depth error function. The loss function used to train the fine network was a linear combination of the depth error (eq. (25)) and the fully supervised version of the image error (eq. (19)). Similarly to many other works, Zeng et al. [129] rendered the synthetic image by modelling the illumination with spherical harmonics basis functions (see eq. (11)). However, since the ground-truth normals \mathbf{n}_{gt} are known, the lighting parameters for the γ can be recovered as

$$\gamma^* = \arg \min_{\gamma} \|\mathcal{A}\gamma^T \mathcal{Y}(\mathbf{n}_{\text{gt}}) - \mathbf{I}_{\text{in}}\|_2^2$$

where \mathcal{A} is the albedo estimated by the SfsNet [109], and $\mathcal{Y}(\mathbf{n}_{\text{gt}})$ are the spherical harmonics basis functions computed with \mathbf{n}_{gt} . Therefore, the supervised image error is

$$\mathbb{E}_{\mathbf{I}(\mathbf{n})} = \|\mathcal{A}\gamma^* \mathcal{Y}(\mathbf{n}) - \mathbf{I}_{\text{in}}\|_2. \quad (26)$$

Finally, the finer network, that refines the output of the F-Net, was trained in a self-supervised manner using the depth error (eq. (25)) and the supervised image error (eq. (26)), although taking \mathbf{D}_{gt} and \mathbf{n}_{gt} as the output of the F-Net.

Shu et al. [150] and Shang et al. [137] also considered a depth loss (eq. (25)) like [129]. The first authors also added the normals error but regularised the output depth with a 3DMM. They also minimised the difference between the estimated depth map and the depth map obtained from a 3DMM-reconstruction $\mathbf{x}(\alpha, \delta)$, where α and δ are the shape and expression 3DMM parameters estimated from the input image with a pre-trained network. In contrast, Shang et al. [137] used the depth error as an additional multi-view consistency loss to ensure depth consistency across the three input images. The designed depth consistency loss is very similar to the image consistency loss (eq. (5.3.3)) but the synthesised depth map from the adjacent view are scaled to rectify the difference of scale in both depth maps.

To also train the network on face recognition, Liu et al. [106] added to the Euclidean loss a softmax loss that served as a face identification error. Bhagavatula et al. [96] added an Euclidean loss over the 2D regressed landmarks so the network also learned to estimate the 2D landmarks over the input image.

5.3.5. Adversarial loss

As explained in Section 5.2.4, Tu et al. [145], Galteri et al. [119, 120], Gao et al. [149], Piao et al. [124], Lin et al. [136] used GANs, which consists of a generator G and a discriminator D , which are jointly trained for D to discriminate between real and fake data and for G to fool D . Therefore, D is trained to maximise $\log(D(\mathbf{y}_{\text{gt}})) \in (-\inf, 0]$, while G is trained to minimise $\log(1 - D(G(\mathbf{x}))) \in (-\inf, 0]$. This is expressed mathe-

matically as the following minimax problem

$$\min_G \max_D \mathcal{L}_{\text{adv}}(G, D)$$

where

$$\mathcal{L}_{\text{adv}}(G, D) = \mathbb{E} \left[\log(D(\mathbf{y}_{\text{gt}})) \right] + \mathbb{E} \left[\log(1 - D(G(\mathbf{x}))) \right] \quad (27)$$

and $\mathbb{E}[X]$ expresses the expected value of a random variable X .

In the case of Tu et al. [145], since they evaluated the consistency of the predicted 3DMM with the input image by taking pairs consisting of the parameters and a latent representation of the image computed with an encoder, eq. (27) is modified as

$$\mathcal{L}_{\text{adv}}(G, D) = \mathbb{E} \left[\log(D([\mathbf{f}, \mathbf{p}])) \right] + \mathbb{E} \left[\log(1 - D([\tilde{\mathbf{f}}, G(\mathbf{I})])) \right]$$

where \mathbf{f} is the latent representation of an image with ground truth parameters \mathbf{p} and $\tilde{\mathbf{f}}$ is the latent representation of an image \mathbf{I} with parameters $G(\mathbf{I})$ estimated by the generator.

Galteri et al. [119, 120], Gao et al. [149] and Lin et al. [136] trained a simple GAN by adopting the paradigm of Improved Wasserstein GAN [189] which allows for a more stable training, where the adversarial loss is defined as

$$\mathcal{L}_{\text{adv}}(G, D) = \mathbb{E} \left[D(\mathbf{I}_{\text{in}}) \right] - \mathbb{E} \left[D(\mathbf{I}_{\text{mod}}) \right] + \lambda \mathbb{E} \left[\left\| \nabla_{\hat{\mathbf{I}}} D(\hat{\mathbf{I}}) \right\| \right] \quad (28)$$

where $\hat{\mathbf{I}}$ is uniformly sampled between pairs of points from the distribution of real and generated images. Since Gao et al. [149] used the discriminator to distinguish real from fake 3D faces and not images, in eq. (28), \mathbf{I}_{in} is the real 3D face, \mathbf{I}_{mod} is the estimated 3D face, and $\hat{\mathbf{I}}$ are 3D faces uniformly sampled between the real and fake distributions.

In contrast, Piao et al. [124] used a CycleGAN to map the real images to synthetic-style images and backwards. The CycleGAN is composed of two GANs concatenated forming a cycle (see eq. (13)) and it is trained following the same idea of the simple GANs but, additionally, a cycle-consistency loss has to be taken into account. This loss function enforces both generators to be able to recover the original image after performing a cycle. That is, let $G_r : \mathcal{S} \rightarrow \mathcal{R}$ and $G_s : \mathcal{R} \rightarrow \mathcal{S}$ be both generators, with \mathcal{R} and \mathcal{S} the space of the real and the synthetic images, respectively; then, the cycle-consistency loss is defined as

$$\mathcal{L}_{\text{cyc}}(G_s, G_r) = \mathbb{E} \left[\left\| G_r(G_s(\mathbf{I}_r)) - \mathbf{I}_r \right\|_1 \right] + \mathbb{E} \left[\left\| G_s(G_r(\mathbf{I}_s)) - \mathbf{I}_s \right\|_1 \right]$$

where $\mathbf{I}_r, G_r(\mathbf{I}_s) \in \mathcal{R}$ and $\mathbf{I}_s, G_s(\mathbf{I}_r) \in \mathcal{S}$. Also, Piao et al.

[124] noticed that the adversarial losses (eq. (27)) for each GAN and the cycle-consistency loss are not sufficient to avoid artefacts and large deformations in the image domain-transfer results. To further constrain the image mapping between the real and synthetic image spaces, they considered a landmarks error defined as

$$\mathcal{L}_{\text{lmks}}(G_1, G_2) = \mathbb{E} \left[\left\| \ell_{\mathbf{I}_s}^{2D} - \ell_{G_s(\mathbf{I}_r)}^{2D} \right\|_2 \right] + \mathbb{E} \left[\left\| \ell_{\mathbf{I}_r}^{2D} - \ell_{G_r(\mathbf{I}_s)}^{2D} \right\|_2 \right]$$

where $\ell_{\mathbf{I}}^{2D}$ denotes the landmarks coordinates estimated in the image \mathbf{I} . Finally, the 3D face reconstruction network, which inputs a synthetic-style image and recovers the position UV-map (see eq. (13)), was trained by minimising three loss functions: one that computed the distance between the resulting and the ground-truth position UV-maps, another one that computed the scalar product between the ground-truth normals and the vectors formed by adjacent vertices, and a landmarks distance term.

5.3.6. Other Losses

Ramon et al. [128] and Guo et al. [18] used the Euclidean distance between the projections of the estimated and ground-truth 3D faces. The first authors inputted a set of K images of the same subject, thus the loss function is

$$\mathbb{E} = \sum_{k=1}^K \left\| \mathcal{P}(\mathbf{x}(\alpha^k), \zeta^k) - \mathcal{P}(\mathbf{x}_{\text{gt}}, \zeta_{\text{gt}}^k) \right\|_2^2 \quad (29)$$

where ζ^k and ζ_{gt}^k are the estimated and ground-truth projection parameters of the k th image, respectively, $\mathbf{x}(\alpha^k)$ and \mathbf{x}_{gt} are the estimated and ground-truth 3D faces, and $\mathcal{P}(\mathbf{x}, \zeta)$ represents the projection of \mathbf{x} according to ζ .

As explained in Section 5.2.5, Guo et al. [18] considered three different networks: the coarse network, which computed a coarse estimate of all the parameters; the tracking coarse network, which estimated the coarse parameters of the next frame in a video sequence; and the fine network, which refined the coarse result. The coarse network was trained similarly to Guo et al. [18] (eq. (29)). However, to be able to control the effect the projection parameters ζ and the geometry parameters θ_{geo} (shape and expression) individually, the estimated 3D face was projected considering the projection parameters as the estimated values and the geometry parameters as the ground truth values (and the other way around):

$$\mathbb{E} = w \mathbb{E}_{\text{proj}} + (1 - w) \mathbb{E}_{\text{geo}}$$

where

$$\mathbb{E}_{\text{proj}} = \left\| \mathcal{P}(\mathbf{x}(\theta_{\text{geo}}^{\text{gt}}, \zeta) - \mathcal{P}(\mathbf{x}(\theta_{\text{geo}}^{\text{gt}}, \zeta^{\text{gt}})) \right\|_2^2 \text{ and}$$

$$\mathbb{E}_{\text{geo}} = \left\| \mathcal{P}(\mathbf{x}(\theta_{\text{geo}}, \zeta^{\text{gt}}) - \mathcal{P}(\mathbf{x}(\theta_{\text{geo}}^{\text{gt}}, \zeta^{\text{gt}})) \right\|_2^2.$$

In the tracking coarse network, to this loss function, they added an image error term, and they trained the fine network with an Euclidean distance loss between the ground

truth and the estimated displacement map.

Song et al. [91] trained a coupled radial basis function network with a loss function that consists of a reconstruction error, a smoothness regularisation term, and a point distribution consistency. The first one ensures that both networks can be stacked together by minimising the difference between the input of one and the output of the other. The second one minimises the energy of the gradient of the map that converts a 2D image (or 3D face) into an intrinsic representation and the gradient of its inverse. And the third one makes the distributions of two sets of intrinsic representations (one from 3D and the other from 2D) similar to each other.

Jackson et al. [99] and Yi et al. [123] used the sigmoid cross-entropy loss to train an hourglass network to estimate the volumetric representation of a face. Trigeorgis et al. [104] compared two different losses to learn to estimate surface normals from facial images: the angular distance between the estimated and the ground truth normals, $\mathbb{E} = 1 - \sum_i \mathbf{n}_i^T \mathbf{n}_{i,gt}$, and the smoothed version of the L_1 norm proposed by [190].

Alp Güler et al. [98], Sela et al. [101] and Feng et al. [111] proposed three different ways to train a network to estimate a depth representation of the 3D face. The first one [98] divided each dimension of the UV-space into a discrete part and a residual part. They used the softmax cross-entropy loss to estimate the discrete part and the smoothed version of the L_1 norm proposed by [190] to estimate the residual part. Sela et al. [101] proposed a loss function that is a linear combination of the L_1 norm over the difference between the estimated and ground truth depth maps and the L_1 norm of the difference between the normals of both depth maps. And Feng et al. [111] proposed a loss function that computes the Euclidean distance between the ground truth and the estimated position UV-maps with a weight mask that assigns a weight to each pixel in the map to penalise errors on the facial regions that have more discriminative features.

Finally, Shang et al. [137] proposed an epipolar loss to account for multi-view consistency. This loss is computed as the symmetric epipolar distance between the 2D landmarks of the input image and the corresponding 2D landmarks in the adjacent-view images.

5.4. Take-home message

Deep learning has proven to be a very powerful tool applicable in many different fields, gaining the attention of great part of the research community, and 3D-from-2D face reconstruction is not an exception. In the last few years, a large amount of works have proposed to reconstruct the 3D facial geometry of a person from one or more images, or even video sequences, using deep learning, as can be seen in Tables 5, 6, and 7.

However, deep learning has an important drawback: the need of huge training sets, in this case, composed of corresponding pairs of 2D images and 3D faces. Since obtaining this amount of ground truth 3D facial scans is not

always feasible, the first works focused on building synthetic data by fitting a 3DMM to real images [92] and/or rendering synthetic images from 3D faces obtained by sampling from the 3DMM [93]. Even though these approaches allow for the construction of large heterogeneous training sets, reconstructing of 3D faces outside the distribution learnt by the 3DMM may be a difficult task, given that the network is not taught with anything but 3DMM-generated faces, and therefore facial details are hardly captured.

To avoid the need of corresponding 3D faces, most recent works train their network in a self-supervised manner by adding a rendering layer that generates a synthetic image from the reconstructed 3D face, and minimising the difference between the input and the rendered image. In most works, this rendering layer is complemented with a more complex learning framework, such as encoder-decoder networks or generative adversarial networks. Also, many works followed a “divide and conquer” approach by proposing architectures composed of several networks where each of them is trained for an specific task. For example, some trained each of the networks to estimate a single attribute (identity, expression, albedo, lighting, pose, etc.), and others proposed sequential networks where each of them refines the output of the previous one.

6. Other Machine Learning Methods

Although deep learning has been a widely used tool in 3D-from-2D face reconstruction, other machine learning methods have been explored. Some researchers approached the 3D-from-2D face reconstruction as a regression problem [191, 192, 193, 194, 195, 196, 197, 198, 199].

Sánchez-Escobedo et al. [198], Rara et al. [196] and Dou et al. [191] trained regressors using the partial least squares algorithm [200]. Sánchez-Escobedo et al. [198] proposed to build a regression matrix \mathcal{B} that regresses the 3D face surfaces as a linear combination of the contour of the images, $\mathbf{X} = \mathcal{C}\mathcal{B}$. The response matrix $\mathbf{X} \in \mathbb{R}^{M \times 3N}$ is built by concatenating the M vectorised 3D training shapes. The predictor matrix $\mathcal{C} \in \mathbb{R}^{M \times 2L}$ is built by concatenating the pixel locations (x, y) of the L 2D contours of the input images (with different poses). After training, this regression matrix can reconstruct a 3D face \mathbf{x} from the contours of the input images of a subject \mathbf{c} , as $\mathbf{x} = \mathcal{B}\mathbf{c}$.

Rara et al. [196] trained two partial least squares regression models to estimate shape and texture model coefficients from the parameters of a spherical harmonics projection model. The shape and texture models were built applying PCA over aligned shapes and textures from the USF Human ID 3D database (similarly to 3DMM, see Section 2.1), whereas the spherical harmonics projection model was built from the input image and the training images as explained next. From each image \mathbf{I}_i in the training set, its reflected light \mathbf{B}_i is estimated assuming a Lambertian illumination model as $\mathcal{A}_i \mathcal{Y}^T$ in eq. (11). Therefore, each image can be recovered as a weighted combination of the columns of \mathbf{B}_i : $\mathbf{I}_i = \mathbf{B}_i \mathbf{l}_i$. Then, for an input image

\mathbf{I}_{in} , we can solve $\mathbf{I}_{\text{in}} = \mathbf{B}_i \mathbf{l}_{i,\text{in}}$ for $\mathbf{l}_{i,\text{in}}$ for each \mathbf{B}_i . This allows to compute the spherical harmonics projection images $\mathcal{I}_i = \mathbf{B}_i \mathbf{l}_{i,\text{in}}$, from a spherical harmonics projection model is built using PCA similarly to the shape and texture models.

A similar idea was followed by Dou et al. [191]. They built two statistical models; one that encoded the variation of the position of the 2D landmarks in a face, and another one that encoded the variation of the 3D landmarks. Thus, given coefficients of the 2D-landmarks-model, their proposed partial least squares regressor estimated coefficients of the 3D-landmarks-model, which were mapped back to landmarks in \mathbb{R}^3 . The 3D landmarks were used to reconstruct the 3D facial shape by recovering the coefficients of a coupled dictionary model. Such model was built from corresponding pairs of sparse 3D landmarks and dense point sets.

Different from the previous works, Rara et al. [197] used a principal component regression model. Their proposed approach resembles that of [191] in the sense that their regressor also estimates coefficients on a 3D shape model from coefficients on a 2D shape model. The main difference is that Rara et al. [197] estimated directly parameters on a statistical model built from dense 3D shapes, instead of a model built from sparse sets of 3D landmarks.

In contrast to the above approaches that used a single regressor, [192, 193, 194, 195, 201, 199] proposed a cascade of linear regressors to estimate the 3D shape. Tian et al. [199], similarly to [197], trained a cascade of regressors \mathcal{R}^k to predict the shape update $\Delta \mathbf{x}^k$ according to the difference between the ground truth 2D landmarks ℓ_{gt}^{2D} and the 3D landmarks of the previous shape projected into the image $\hat{\ell}^{2D,k-1}$, $\mathbf{x}^k = \mathbf{x}^{k-1} + \Delta \mathbf{x}^k = \mathbf{x}^{k-1} + \mathcal{R}^k \left(\ell_{\text{gt}}^{2D} - \hat{\ell}^{2D,k-1} \right)$. The regressors are trained by minimising the Euclidean distance between the ground truth shape update $\Delta \mathbf{x}_{\text{gt}}^k = \mathbf{x}_{\text{gt}} - \mathbf{x}^{k-1}$ and the estimated shape update by the current regressor over the M training pairs,

$$\mathcal{R}^k = \arg \min_{\mathcal{R}} \sum_{m=1}^M \left\| \Delta \mathbf{x}_{m,\text{gt}}^k - \mathcal{R} \left(\ell_{m,\text{gt}}^{2D} - \hat{\ell}_m^{2D,k-1} \right) \right\|_2^2.$$

Jeni et al. [192, 193] and Liu et al. [194, 195, 201] estimated the 2D landmarks in the input image along with the 3D shape. The first two methods [192, 193] used as input a 2D video, reconstructing the 3D face for each frame. They applied a cascaded regressor that estimated a dense set of facial points in the 2D frame, which were in correspondence with the vertices of a 3D face model. Then, the 3D face model was fitted to the frame by minimising the Euclidean distance between the projection of the model vertices and the estimated 2D facial points. Liu et al. [194, 195, 201] jointly estimated the 2D landmarks and the 3D shape, alternately updating each of them. In each step, the 2D landmarks were updated through the landmarks regressor \mathcal{R}_{ℓ}^k on the texture features extracted

around the landmarks in the input image $h(\mathbf{I}_{\text{in}}, \ell^{2D,k-1})$,

$$\begin{aligned} \ell^{2D,k} &= \ell^{2D,k-1} + \Delta \ell^{2D,k} \\ &= \ell^{2D,k-1} + \mathcal{R}_{\ell}^k(h(\mathbf{I}_{\text{in}}, \ell^{2D,k-1})). \end{aligned}$$

Then, a shape regressor estimated the update of the shape according to the landmarks update, $\mathbf{x}^k = \mathbf{x}^{k-1} + \Delta \mathbf{x}^k = \mathbf{x}^{k-1} + \mathcal{R}_{\mathbf{x}}^k(\Delta \ell^{2D,k})$. Finally, the 2D landmarks were refined by projecting the 3D landmarks on the updated shape assuming a weak perspective projection whose projection matrix is estimated as

$$\mathbf{P}^k = \arg \min_{\mathbf{P}} \left\| \ell^{2D,k} - \mathbf{P} \times \ell^{3D,k} \right\|_2^2.$$

Whereas in their preliminary work, Liu et al. [194, 195] estimated the face shape update jointly for the identity-related and expression-related deformations, in their latter work [201], they considered $\mathbf{x}^k = \mathbf{x}^{k-1} + \Delta \mathbf{x}_{\text{id}}^k + \Delta \mathbf{x}_{\text{exp}}^k$, thus the regressor estimated the identity and the expression updates as separated elements, i.e., $\mathcal{R}_{\mathbf{x}}^k(\Delta \ell^{2D,k}) = (\Delta \mathbf{x}_{\text{id}}^k, \Delta \mathbf{x}_{\text{exp}}^k)$.

Differently from all the previous works, Wang et al. [202] addressed the 3D face reconstruction from an uncalibrated 2D video as a minimisation problem based on dense optical flow. First, a 3D personalised template is obtained from the collection of frames with [80], and the method by [203] is applied to estimate a dense 2D optical flow of the video. With this two elements, they proposed the following energy function to translate the 2D optical flow to the personalised template,

$$\mathbb{E}(\mathbf{f}, \mathbf{R}, \tau) = \sum_{i=1}^N \left\| \mathbf{P}(\mathbf{R}(\mathbf{v}_i + \mathbf{f}(\mathbf{v}_i)) + \tau) - L(\mathbf{P}(\mathbf{R}\mathbf{v}_i + \tau)) \right\|_e$$

where $\{\mathbf{v}_i\}_{i=1}^N$ is the set of 3D vertices of the personalised 3D facial template, $\mathbf{P} = \begin{pmatrix} 1 & 0 & 0 \\ 0 & 1 & 0 \end{pmatrix}$ is the projection matrix of the weak perspective camera model and \mathbf{R} and τ are the rotation and translation. $\mathbf{f}(\mathbf{v}) = (\Delta v^x, \Delta v^y, \Delta v^z) \in \mathbb{R}^3$ is the per-vertex displacement which is to be estimated from the 2D optical flow L . Also, two additional terms are added to ensure local smoothness and rigidity of the deformations $\mathbf{f}(\cdot)$, and a fourth term to regularise the deformations in the temporal domain, i.e., deformations from consecutive frames cannot be very different. Finally, the resulting 3D face is refined by minimising the difference between the input images and the synthetic image obtained by assuming a Lambertian reflectance modelled using spherical harmonics (eq. (11)).

7. Summary and Conclusions

In this paper, we review the state-of-the-art of 3D-from-2D face reconstruction in the last decade, separating the different proposed approaches into three main strategies: 3D facial model fitting (Section 3), photometric stereo (Section 4), and deep learning (Section 5).

As we have explained throughout this paper, recovering the 3D face from uncalibrated 2D pictures is an underdetermined problem, thus, further constraints must be added to reconstruct unequivocally the 3D facial geometry. In the last decade, researchers have explored two different ways of adding such constraints: one way is considering a collection of photos from the same person, and the other way is adding statistical constraints.

The first approach is mostly followed by photometric stereo-based methods, which base the reconstruction process on studying the reflectance of the light on the face, i.e. on recovering the 3D geometry according to shadows. The use of multiple images allows the researchers to have many samples of lighting conditions. Whereas these methods are able to recover geometric details, the assumptions they consider, such as Lambertian reflectance, are too restrictive, and the estimated 3D faces usually show artefacts. As a result, this strategy has been barely explored, and most researchers have focused their efforts on constraining the problem with statistical priors.

Statistical constraints help obtaining plausible 3D faces by restricting the space of solutions of the 3D-from-2D face reconstruction problem avoiding artefacts or unrealistic 3D faces. The 3DMM are the most widespread statistical facial models, because of their capacity of encoding the geometric (and possibly texture) variations of the human face, and they are used to ensure plausibility of the solutions. For this reason, many researchers have explored the strategy of fitting a 3DMM to an image to recover the 3D face. Essentially, this fitting consists in estimating the model parameters by minimising the difference between the image and the projection of the 3DMM onto the image plane. However, minimising this difference on the 2D space is not sufficient to recover fine facial details. Thus, most 3DMM fitting approaches only reconstruct coarse shapes, and they are not able to recover subtle geometric details that are still important to achieve faithful reconstructions.

In the last few years, there has been a growing trend towards recovering such subtle details of each person, while keeping a realistic 3D face. This has produced a decrease on the effort invested in the previous mentioned strategies, photometric stereo and 3DMM fitting. Instead, many researchers have applied deep learning methods, which have shown to perform satisfactorily in many fields. Nevertheless, the main drawback of deep learning methods is the huge amount of data needed to train them. Therefore, many researchers have taken advantage of pre-built 3DMM to generate synthetic training sets: fitting a 3DMM to real images and/or rendering synthetic images from randomly sampled faces from a 3DMM.

Even so, if a deep learning method is trained with a 3DMM-generated dataset, it will only learn to recover faces that are encoded by the 3DMM. Thus, as in 3DMM fitting methods, fine details are hardly captured. In view of this issue, the most recent methods are exploring the use of self-supervision with autoencoders or GANs, avoiding the need of corresponding 2D-3D data.

Appendix A. Notation

Appendix A.1. 3D facial model

M : number of faces in the model

N : number of vertices of the meshes

Shape model

\mathbf{x} : shapes in 3D

\widetilde{M} : number of eigenvectors in the 3D facial shape model

$\phi_i \in \mathbb{R}^{3N}$: eigenvectors of 3D facial shape model

$$\Phi = \begin{pmatrix} \vdots & & \vdots \\ \phi_1 & \cdots & \phi_{\widetilde{M}} \\ \vdots & & \vdots \end{pmatrix} \in \mathbb{R}^{(3N) \times \widetilde{M}}$$

$\sigma_{\alpha_i}^2 \in \mathbb{R}$: eigenvalues of shape model

$\alpha_i \in \mathbb{R}$: shape model parameters

$\alpha = (\alpha_1, \dots, \alpha_{\widetilde{M}})$

$\mathbf{x}(\alpha)$: 3D face generated by α

Texture model

\mathbf{c} : albedo of a 3D face (a.k.a texture or colour)

\widetilde{N} : number of eigenvectors in the 3D facial texture model

$\psi_i \in \mathbb{R}^{3N}$: eigenvectors of texture model

$$\Psi \in \mathbb{R}^{(3N) \times \widetilde{N}}$$

$\sigma_{\beta_i}^2 \in \mathbb{R}$: eigenvalues of texture model

$\beta_i \in \mathbb{R}$: texture model parameters

$\beta = (\beta_1, \dots, \beta_{\widetilde{N}})$

γ_d : diffuse lighting parameters

γ_s : specular lighting parameters

Appendix A.2. 3D facial model fitting

\mathbf{I}_{in} : input image

\mathbf{I}_{mod} : rendered image from reconstructed 3D face

L : number of landmarks

ℓ^{2D} : landmarks in the input image

ℓ^{3D} : landmarks in the 3D face

$\hat{\ell}^{2D}$: projection of landmarks in the 3D face ℓ^{3D} into the image plane

$\hat{\ell}^{3D}$: projection of landmarks in the image ℓ^{2D} into the 3D face

κ : intrinsic camera parameters (depends on the camera model, but usually focal length, principal point, ...)

\mathbf{R} : rotation matrix

τ : translation

$\zeta = \{\mathbf{R}, \tau, \kappa\}$: projection parameters (intrinsic and extrinsic)

ρ : rendering parameters (including κ , \mathbf{R} , τ and illumination parameters)

$\mathcal{P}(\mathbf{v}, \zeta)$: projection of $\mathbf{v} \in \mathbb{R}^3$ according to parameters ζ

$\mathbb{E}_{\mathbf{I}}$: distance between \mathbf{I}_{in} and \mathbf{I}_{mod}

\mathbb{E}_{lmk2D} : distance between ℓ^{2D} and $\hat{\ell}^{2D}$

\mathbb{E}_{lmk3D} : distance between ℓ^{3D} and $\hat{\ell}^{3D}$

\mathbb{E}_{reg} : regularisation of the fitting parameters

Acknowledgements

This work is partly supported by the Spanish Ministry of Economy and Competitiveness under project grant TIN2017-90124-P, the Ramon y Cajal programme, the Maria de Maeztu Units of Excellence Programme (MDM-2015-0502).

References

- [1] L. Zhang, M. Jiang, D. Farid, M. A. Hossain, Intelligent facial emotion recognition and semantic-based topic detection for a humanoid robot, *Expert Syst. Appl.* 40 (2013) 5160–5168.
- [2] D. W. Hansen, Q. Ji, In the eye of the beholder: A survey of models for eyes and gaze, *IEEE Trans. on Pattern Anal. and Machine Intel.* 32 (2010) 478–500.
- [3] S. Kaplan, M. A. Guvensan, A. G. Yavuz, Y. Karalurt, Driver behavior analysis for safe driving: A survey, *IEEE trans. Intell. Transp. Syst.* 16 (2015) 3017–3032.
- [4] A. M. Burton, S. Wilson, M. Cowan, V. Bruce, Face recognition in poor-quality video: Evidence from security surveillance, *Psychol. Sci.* 10 (1999) 243–248.
- [5] T. Weise, S. Bouaziz, H. Li, M. Pauly, Realtime performance-based facial animation, *ACM Trans. Graph.* 30 (2011) 77.
- [6] T. Weise, H. Li, L. Van Gool, M. Pauly, Face/off: Live facial puppetry, in: *Proc. of SCA*, 2009, pp. 7–16.
- [7] M. C. E. Rai, N. Werghi, H. Al Muhairi, H. Alsafar, Using facial images for the diagnosis of genetic syndromes: a survey, in: *Proc. of ICCSPA*, 2015, pp. 1–6.
- [8] M. Suttie, T. Foroud, L. Wetherill, J. L. Jacobson, C. D. Molteno, E. M. Meintjes, H. E. Hoyme, N. Khaole, L. K. Robinson, E. P. Riley, et al., Facial dysmorphism across the fetal alcohol spectrum, *Pediatrics* 131 (2013) 779–788.
- [9] J. J. Cerrolaza, A. R. Porras, A. Mansoor, Q. Zhao, M. Summar, M. G. Linguraru, Identification of dysmorphic syndromes using landmark-specific local texture descriptors, in: *Proc. of IEEE ISBI*, 2016, pp. 1080–1083.
- [10] R. J. Hennessy, P. A. Baldwin, D. J. Browne, A. Kinsella, J. L. Waddington, Three-dimensional laser surface imaging and geometric morphometrics resolve frontonasal dysmorphology in schizophrenia, *Biol. Psychiatry* 61 (2007) 1187–1194.
- [11] O. Alexander, M. Rogers, W. Lambeth, J.-Y. Chiang, W.-C. Ma, C.-C. Wang, P. Debevec, The digital Emily project: Achieving a photorealistic digital actor, *IEEE Comput. Graph. Appl.* 30 (2010) 20–31.
- [12] T. Beeler, B. Bickel, P. Beardsley, B. Sumner, M. Gross, High-quality single-shot capture of facial geometry, *ACM Trans. Graph.* 29 (2010) 40.
- [13] T. Beeler, F. Hahn, D. Bradley, B. Bickel, P. Beardsley, C. Gotsman, R. W. Sumner, M. Gross, High-quality passive facial performance capture using anchor frames, *ACM Trans. Graph.* 30 (2011) 75.
- [14] Y. Lee, D. Terzopoulos, K. Waters, Realistic modeling for facial animation, in: *Proc. of ACM SIGGRAPH*, 1995, pp. 55–62.
- [15] K. Khoshelham, S. O. Elberink, Accuracy and resolution of kinect depth data for indoor mapping applications, *IEEE Sens. J.* 12 (2012) 1437–1454.
- [16] L. Yang, L. Zhang, H. Dong, A. Alelaiwi, A. El Saddik, Evaluating and improving the depth accuracy of kinect for windows v2, *IEEE Sens. J.* 15 (2015) 4275–4285.
- [17] J. Booth, A. Roussos, E. Ververas, E. Antonakos, S. Ploumpis, Y. Panagakis, S. P. Zafeiriou, 3D reconstruction of “in-the-wild” faces in images and videos, *IEEE Trans. on Pattern Anal. and Machine Intel.* 40 (2018) 2638–2652.
- [18] Y. Guo, J. Zhang, J. Cai, B. Jiang, J. Zheng, CNN-based real-time dense face reconstruction with inverse-rendered photorealistic face images, *IEEE Trans. on Pattern Anal. and Machine Intel.* 41 (2018) 1294–1307.
- [19] A. T. Tran, T. Hassner, I. Masi, E. Paz, Y. Nirkin, G. Medioni, Extreme 3D face reconstruction: Seeing through occlusions, in: *Proc. of IEEE CVPR*, 2018, pp. 3935–3944.
- [20] A. F. Abate, M. Nappi, D. Riccio, G. Sabatino, 2D and 3D face recognition: A survey, *Pattern Recognit. Lett.* 28 (2007) 1885–1906.
- [21] C. Cao, Y. Weng, S. Lin, K. Zhou, 3D shape regression for real-time facial animation, *ACM Trans. Graph.* 32 (2013) 41.
- [22] C. A. Corneanu, M. O. Simón, J. F. Cohn, S. E. Guerrero, Survey on RGB, 3D, thermal, and multimodal approaches for facial expression recognition: History, trends, and affect-related applications, *IEEE Trans. on Pattern Anal. and Machine Intel.* 38 (2016) 1548–1568.
- [23] L. Tu, A. R. Porras, A. Boyle, M. G. Linguraru, Analysis of 3D facial dysmorphology in genetic syndromes from unconstrained 2D photographs, in: *Proc of MICCAI*, 2018, pp. 347–355.
- [24] M. D. Levine, Y. Yu, State-of-the-art of 3D facial reconstruction methods for face recognition based on a single 3D training image per person, *Pattern Recognit. Lett.* 30 (2009) 908–913.
- [25] G. Stylianou, A. Lanitis, Image based 3D face reconstruction: a survey, *Int. J. Image Graph.* 9 (2009) 217–250.
- [26] C. Y. Suen, A. Z. Langaroudi, C. Feng, Y. Mao, A survey of techniques for face reconstruction, in: *IEEE Int. Conf. Syst., Man, Cybern.*, 2007, pp. 3554–3560.
- [27] W. N. Widanagamaachchi, A. T. Dharmaratne, 3D face reconstruction from 2D images, in: *Proc. of DICTA*, 2008, pp. 365–371.
- [28] M. Zollhöfer, J. Thies, P. Garrido, D. Bradley, T. Beeler, P. Pérez, M. Stamminger, M. Nießner, C. Theobalt, State of the art on monocular 3D face reconstruction, tracking, and applications, *Comput. Graph. Forum* 37 (2018) 523–550.
- [29] B. Egger, W. A. P. Smith, A. Tewari, S. Wuhrer, M. Zollhoefer, T. Beeler, F. Bernard, T. Bolkart, A. Kortylewski, S. Romdhani, C. Theobalt, V. Blanz, T. Vetter, 3D morphable face models—past, present, and future, *ACM Trans. Graph.* 39 (2020).
- [30] V. Blanz, T. Vetter, A morphable model for the synthesis of 3D faces, in: *Proc. of ACM SIGGRAPH*, 1999, pp. 187–194.
- [31] H. Jin, X. Wang, Z. Zhong, J. Hua, Robust 3D face modeling

- and reconstruction from frontal and side images, *Comput. Aided Geom. Des.* 50 (2017) 1–13.
- [32] A. Brunton, T. Bolkart, S. Wuhrer, Multilinear wavelets: A statistical shape space for human faces, in: *Proc. of ECCV*, 2014, pp. 297–312.
- [33] M. Lüthi, T. Gerig, C. Jud, T. Vetter, Gaussian process morphable models, *IEEE Trans. on Pattern Anal. and Machine Intel.* 40 (2018) 1860–1873.
- [34] L. Tran, X. Liu, Nonlinear 3D face morphable model, in: *Proc. of IEEE CVPR*, 2018, pp. 7346–7355.
- [35] P. Paysan, R. Knothe, B. Amberg, S. Romdhani, T. Vetter, A 3D face model for pose and illumination invariant face recognition, in: *Proc of IEEE AVSS*, 2009, pp. 296–301.
- [36] B. Amberg, S. Romdhani, T. Vetter, Optimal step nonrigid ICP algorithms for surface registration, in: *Proc. of IEEE CVPR*, 2007, pp. 1–8.
- [37] P. Huber, G. Hu, J. R. Tena, P. Mortazavian, P. Koppen, W. J. Christmas, M. Ratsch, J. Kittler, A multiresolution 3D morphable face model and fitting framework, in: *Proc. of VISAPP*, 2016, pp. 79–86.
- [38] J. R. Tena, M. Hamouz, A. Hilton, J. Illingworth, A validated method for dense non-rigid 3D face registration, in: *Proc of IEEE AVSS*, 2006, pp. 81–81.
- [39] J. Booth, A. Roussos, A. Ponniah, D. Dunaway, S. Zafeiriou, Large scale 3D morphable models, *Int. J. Comput. Vis.* 126 (2017) 233–254.
- [40] H. Dai, N. Pears, W. A. P. Smith, C. Duncan, A 3D morphable model of craniofacial shape and texture variation, in: *Proc. of IEEE ICCV*, 2017, pp. 3104–3112.
- [41] C. Cao, Y. Weng, S. Zhou, Y. Tong, K. Zhou, FaceWarehouse: A 3D facial expression database for visual computing, *IEEE Trans. Vis. Comput. Graph.* 20 (2014) 413–425.
- [42] A. Myronenko, X. Song, Point set registration: Coherent Point Drift, *IEEE Trans. on Pattern Anal. and Machine Intel.* 32 (2010) 2262–2275.
- [43] T. F. Cootes, C. J. Taylor, D. H. Cooper, J. Graham, Active shape models - their training and application, *Comput. Vis. Image Underst.* 61 (1995) 38–59.
- [44] O. Aldrian, W. A. P. Smith, A linear approach of 3D face shape and texture recovery using a 3D morphable model, in: *Proc. of BMVC*, 2010, pp. 75:1–75:10.
- [45] O. Aldrian, W. A. P. Smith, Inverse rendering with a morphable model: A multilinear approach, in: *Proc. of BMVC*, 2011, pp. 88:1–88:10.
- [46] O. Aldrian, W. A. P. Smith, Inverse rendering in SUV space with a linear texture model, in: *Proc. of IEEE ICCV Workshops*, 2011, pp. 822–829.
- [47] O. Aldrian, W. A. P. Smith, Inverse rendering of faces with a 3D morphable model, *IEEE Trans. on Pattern Anal. and Machine Intel.* 35 (2013) 1080–1093.
- [48] S. Schönborn, A. Forster, B. Egger, T. Vetter, A monte carlo strategy to integrate detection and model-based face analysis, in: *Proc. of GCPR*, 2013, pp. 101–110.
- [49] F. Shi, H.-T. Wu, X. Tong, J. Chai, Automatic acquisition of high-fidelity facial performances using monocular videos, *ACM Trans. Graph.* 33 (2014) 222.
- [50] L. Ding, X. Ding, C. Fang, 3D face sparse reconstruction based on local linear fitting, *Vis. Comput.* 30 (2014) 189–200.
- [51] C. Qu, E. Monari, T. Schuchert, J. Beyerer, Fast, robust and automatic 3D face model reconstruction from videos, in: *Proc of IEEE AVSS*, 2014, pp. 113–118.
- [52] C. Qu, E. Monari, T. Schuchert, J. Beyerer, Adaptive contour fitting for pose-invariant 3D face shape reconstruction, in: *Proc. of BMVC*, 2015, pp. 87:1–87:12.
- [53] P. Huber, Z.-H. Feng, W. J. Christmas, J. T. Kittler, M. Ratsch, Fitting 3D morphable face models using local features, in: *Proc. of ICIP*, 2015, pp. 1195–1199.
- [54] X. Zhu, Z. Lei, J. Yan, D. Yi, S. Z. Li, High-fidelity pose and expression normalization for face recognition in the wild, in: *Proc. of IEEE CVPR*, 2015, pp. 787–796.
- [55] X. Zhu, J. Yan, D. Yi, Z. Lei, S. Z. Li, Discriminative 3D morphable model fitting, in: *Proc. of IEEE FG*, volume 1, 2015, pp. 1–8.
- [56] A. Bas, W. A. P. Smith, T. Bolkart, S. Wuhrer, Fitting a 3D morphable model to edges: A comparison between hard and soft correspondences, in: *Proc. of ACCV Workshops*, 2016, pp. 377–391.
- [57] M. Piotraschke, V. Blanz, Automated 3D face reconstruction from multiple images using quality measures, in: *Proc. of IEEE CVPR*, 2016, pp. 3418–3427.
- [58] P. Garrido, M. Zollhöfer, D. Casas, L. Valgaerts, K. Varanasi, P. Pérez, C. Theobalt, Reconstruction of personalized 3D face rigs from monocular video, *ACM Trans. Graph.* 35 (2016) 28.
- [59] J. Thies, M. Zollhöfer, M. Stamminger, C. Theobalt, M. Nießner, Face2Face: Real-time face capture and reenactment of rgb videos, in: *Proc. of IEEE CVPR*, 2016, pp. 2387–2395.
- [60] G. Hu, F. Yan, J. Kittler, W. Christmas, C. H. Chan, Z. Feng, P. Huber, Efficient 3D morphable face model fitting, *Pattern Recognit.* 67 (2017) 366–379.
- [61] M. Hernandez, T. Hassner, J. Choi, G. Medioni, Accurate 3D face reconstruction via prior constrained structure from motion, *Comput. Graph.* 66 (2017) 14–22.
- [62] J. Booth, E. Antonakos, S. Ploumpis, G. Trigeorgis, Y. Panagakis, S. Zafeiriou, 3D face morphable models “in-the-wild”, in: *Proc. of IEEE CVPR*, 2017, pp. 5464–5473.
- [63] L. Jiang, J. Zhang, B. Deng, H. Li, L. Liu, 3D face reconstruction with geometry details from a single image, *IEEE Trans. Image Process.* 27 (2018) 4756–4770.
- [64] B. Gecer, S. Ploumpis, I. Kotsia, S. Zafeiriou, GANFIT: Generative adversarial network fitting for high fidelity 3D face reconstruction, in: *Proc. of IEEE CVPR*, 2019, pp. 1155–1164.
- [65] P. Liu, Y. Yu, Y. Zhou, S. Du, Single view 3D face reconstruction with landmark updating, in: *Proc. of IEEE MIPR*, 2019, pp. 403–408.
- [66] E. Sariyanidi, C. J. Zampella, R. T. Schultz, B. Tunc, Inequality-constrained and robust 3D face model fitting, in: *Proc. of ECCV*, 2020.
- [67] M. R. Koujan, A. Roussos, Combining dense nonrigid structure from motion and 3D morphable models for monocular 4d face reconstruction, in: *Proc. of CVMP*, 2018, pp. 2:1–2:9.
- [68] B. T. Phong, Illumination for computer generated pictures, *Commun. ACM* 18 (1975) 311–317.
- [69] V. Blanz, T. Vetter, Face recognition based on fitting a 3D morphable model, *IEEE Trans. on Pattern Anal. and Machine Intel.* 25 (2003) 1063–1074.
- [70] G. Tzimiropoulos, S. Zafeiriou, M. Pantic, Robust and efficient parametric face alignment, in: *Proc. of IEEE ICCV*, 2011, pp. 1847–1854.
- [71] J. Deng, J. Guo, N. Xue, S. Zafeiriou, ArcFace: Additive angular margin loss for deep face recognition, in: *Proc. of IEEE CVPR*, 2019, pp. 4690–4699.
- [72] D. F. Dementhon, L. S. Davis, Model-based object pose in 25 lines of code, *Int. J. Comput. Vis.* 15 (1995) 123–141.
- [73] R. Hartley, A. Zisserman, *Multiple view geometry in computer vision*, 2 ed., Cambridge University Press, New York, NY, USA, 2003.
- [74] T. Zickler, S. P. Mallick, D. J. Kriegman, P. N. Belhumeur, Color subspaces as photometric invariants, *Int. J. Comput. Vis.* 79 (2008) 13–30.
- [75] R. J. Woodham, Photometric method for determining surface orientation from multiple images, *Opt. Eng.* 19 (1980) 139–144.
- [76] I. Kemelmacher-Shlizerman, S. M. Seitz, Face reconstruction in the wild, in: *Proc. of IEEE ICCV*, 2011, pp. 1746–1753.
- [77] S. Liang, L. G. Shapiro, I. Kemelmacher-Shlizerman, Head reconstruction from internet photos, in: *Proc. of ECCV*, 2016, pp. 360–374.
- [78] S. Suwajanakorn, I. Kemelmacher-Shlizerman, S. M. Seitz, Total moving face reconstruction, in: *Proc. of ECCV*, 2014, pp. 796–812.
- [79] P. Snape, Y. Panagakis, S. Zafeiriou, Automatic construction

- of robust spherical harmonic subspaces, in: Proc. of IEEE CVPR, 2015, pp. 91–100.
- [80] J. Roth, Y. Tong, X. Liu, Unconstrained 3D face reconstruction, in: Proc. of IEEE CVPR, 2015, pp. 2606–2615.
- [81] D. Zeng, Q. Zhao, S. Long, J. Li, Exemplar coherent 3D face reconstruction from forensic mugshot database, *Image Vis. Comput.* 58 (2017) 193–203.
- [82] J. Roth, Y. Tong, X. Liu, Adaptive 3D face reconstruction from unconstrained photo collections, in: Proc. of IEEE CVPR, 2016, pp. 4197–4206.
- [83] I. Kemelmacher-Shlizerman, R. Basri, 3D face reconstruction from a single image using a single reference face shape, *IEEE Trans. on Pattern Anal. and Machine Intel.* 33 (2011) 394–405.
- [84] M. Lee, C.-H. Choi, Fast facial shape recovery from a single image with general, unknown lighting by using tensor representation, *Pattern Recognit.* 44 (2011) 1487–1496.
- [85] R. Kumar, A. Barmpoutis, A. Banerjee, B. C. Vemuri, Non-lambertian reflectance modeling and shape recovery of faces using tensor splines, *IEEE Trans. on Pattern Anal. and Machine Intel.* 33 (2011) 533–567.
- [86] M. Lee, C.-H. Choi, A robust real-time algorithm for facial shape recovery from a single image containing cast shadow under general, unknown lighting, *Pattern Recognit.* 46 (2013) 38–44.
- [87] M. Lee, C.-H. Choi, Real-time facial shape recovery from a single image under general, unknown lighting by rank relaxation, *Comput. Vis. Image Underst.* 120 (2014) 59–69.
- [88] X. Cao, Z. Chen, A. Chen, X. Chen, S. Li, J. Yu, Sparse photometric 3D face reconstruction guided by morphable models, in: Proc. of IEEE CVPR, 2018, pp. 4635–4644.
- [89] Y. Li, L. Ma, H. Fan, K. Mitchell, Feature-preserving detailed 3D face reconstruction from a single image, in: Proc. of CVMP, 2018, pp. 1:1–1:9.
- [90] G. Rotger, F. Moreno-Noguer, F. Lumbreras, A. Agudo, Detailed 3D face reconstruction from a single RGB image, in: Proc. of WSCG, 2019, pp. 103–112.
- [91] M. Song, D. Tao, X. Huang, C. Chen, J. Bu, Three-dimensional face reconstruction from a single image by a coupled RBF network, *IEEE Trans. Image Process.* 21 (2012) 2887–2897.
- [92] X. Zhu, Z. Lei, X. Liu, H. Shi, S. Z. Li, Face alignment across large poses: A 3D solution, in: Proc. of IEEE CVPR, 2016, pp. 146–155.
- [93] E. Richardson, M. Sela, R. Kimmel, 3D face reconstruction by learning from synthetic data, in: Proc. of 3DV, 2016, pp. 460–469.
- [94] A. Jourabloo, X. Liu, Large-pose face alignment via CNN-based dense 3D model fitting, in: Proc. of IEEE CVPR, 2016, pp. 4188–4196.
- [95] A. Jourabloo, X. Liu, Pose-invariant face alignment via CNN-based dense 3D model fitting, *Int. J. Comput. Vis.* 124 (2017) 187–203.
- [96] C. Bhagavatula, C. Zhu, K. Luu, M. Savvides, Faster than real-time facial alignment: A 3D spatial transformer network approach in unconstrained poses, in: Proc. of IEEE ICCV, 2017, pp. 3980–3989.
- [97] P. Dou, S. K. Shah, I. A. Kakadiaris, End-to-end 3D face reconstruction with deep neural networks, in: Proc. of IEEE CVPR, 2017, pp. 5908–5917.
- [98] R. Alp Güler, G. Trigeorgis, E. Antonakos, P. Snape, S. Zafeiriou, I. Kokkinos, Densereg: Fully convolutional dense shape regression in-the-wild, in: Proc. of IEEE CVPR, 2017, pp. 6799–6808.
- [99] A. S. Jackson, A. Bulat, V. Argyriou, G. Tzimiropoulos, Large pose 3D face reconstruction from a single image via direct volumetric CNN regression, in: Proc. of IEEE ICCV, 2017, pp. 1031–1039.
- [100] E. Richardson, M. Sela, R. Or-El, R. Kimmel, Learning detailed face reconstruction from a single image, in: Proc. of IEEE CVPR, 2017, pp. 1259–1268.
- [101] M. Sela, E. Richardson, R. Kimmel, Unrestricted facial geometry reconstruction using image-to-image translation, in: Proc. of IEEE ICCV, 2017, pp. 1576–1585.
- [102] A. Tewari, M. Zollhöfer, H. Kim, P. Garrido, F. Bernard, P. Pérez, C. Theobalt, MoFA: Model-based deep convolutional face autoencoder for unsupervised monocular reconstruction, in: Proc. of IEEE ICCV, 2017, pp. 1274–1283.
- [103] A. Jourabloo, M. Ye, X. Liu, L. Ren, Pose-invariant face alignment with a single CNN, in: Proc. of IEEE ICCV, 2017, pp. 3200–3209.
- [104] G. Trigeorgis, P. Snape, I. Kokkinos, S. Zafeiriou, Face normals “in-the-wild” using fully convolutional networks, in: Proc. of IEEE CVPR, 2017, pp. 340–349.
- [105] A. T. Tran, T. Hassner, I. Masi, G. Medioni, Regressing robust and discriminative 3D morphable models with a very deep neural network, in: Proc. of IEEE CVPR, 2017, pp. 5163–5172.
- [106] F. Liu, R. Zhu, D. Zeng, Q. Zhao, X. Liu, Disentangling features in 3D face shapes for joint face reconstruction and recognition, in: Proc. of IEEE CVPR, 2018, pp. 5216–5225.
- [107] F. Liu, L. Tran, X. Liu, 3D face modeling from diverse raw scan data, in: Proc. of IEEE ICCV, 2019, pp. 9407–9417.
- [108] H. Kim, M. Zollhöfer, A. Tewari, J. Thies, C. Richardt, C. Theobalt, Inversefacenet: Deep monocular inverse face rendering, in: Proc. of IEEE CVPR, 2018, pp. 4625–4634.
- [109] S. Sengupta, A. Kanazawa, C. D. Castillo, D. W. Jacobs, Sf-SNet: Learning shape, reflectance and illuminance of faces in the wild, in: Proc. of IEEE CVPR, 2018, pp. 6296–6305.
- [110] A. Tewari, M. Zollhöfer, P. Garrido, F. Bernard, H. Kim, P. Pérez, C. Theobalt, Self-supervised multi-level face model learning for monocular reconstruction at over 250 Hz, in: Proc. of IEEE CVPR, 2018, pp. 2549–2559.
- [111] Y. Feng, F. Wu, X. Shao, Y. Wang, X. Zhou, Joint 3D face reconstruction and dense alignment with position map regression network, in: Proc. of ECCV, 2018, pp. 534–551.
- [112] K. Genova, F. Cole, A. Maschinot, A. Sarna, D. Vlasic, W. T. Freeman, Unsupervised training for 3D morphable model regression, in: Proc. of IEEE CVPR, 2018, pp. 8377–8386.
- [113] A. Tewari, M. Zollhöfer, F. Bernard, P. Garrido, H. Kim, P. Pérez, C. Theobalt, High-fidelity monocular face reconstruction based on an unsupervised model-based face autoencoder, *IEEE Trans. on Pattern Anal. and Machine Intel.* 42 (2020) 357–370.
- [114] X. Zhu, X. Liu, Z. Lei, S. Z. Li, Face alignment in full pose range: A 3D total solution, *IEEE Trans. on Pattern Anal. and Machine Intel.* 41 (2019) 78–92.
- [115] L. Tran, X. Liu, On learning 3D face morphable model from in-the-wild images, *IEEE Trans. on Pattern Anal. and Machine Intel.* (Early Access) (2019).
- [116] L. Tran, F. Liu, X. Liu, Towards high-fidelity nonlinear 3D face morphable model, in: Proc. of IEEE CVPR, 2019, pp. 1126–1135.
- [117] Y. Zhou, J. Deng, I. Kotsia, S. Zafeiriou, Dense 3D face decoding over 2500FPS: Joint texture & shape convolutional mesh decoders, in: Proc. of IEEE CVPR, 2019, pp. 1097–1106.
- [118] S. Sanyal, T. Bolkart, H. Feng, M. J. Black, Learning to regress 3D face shape and expression from an image without 3D supervision, in: Proc. of IEEE CVPR, 2019, pp. 7763–7772.
- [119] L. Galteri, C. Ferrari, G. Lisanti, S. Berretti, A. Del Bimbo, Coarse-to-fine 3D face reconstruction, in: Proc. of IEEE CVPR Workshops, 2019, pp. 25–31.
- [120] L. Galteri, C. Ferrari, G. Lisanti, S. Berretti, A. Del Bimbo, Deep 3D morphable model refinement via progressive growing of conditional generative adversarial networks, *Comput. Vis. Image Underst.* 185 (2019) 31–42.
- [121] Y. Deng, J. Yang, S. Xu, D. Chen, Y. Jia, X. Tong, Accurate 3D face reconstruction with weakly-supervised learning: From single image to image set, in: Proc. of IEEE CVPR Workshops, 2019, pp. 285–295.
- [122] F. Wu, L. Bao, Y. Chen, Y. Ling, Y. Song, S. Li, K. N. Ngan, W. Liu, MVF-Net: Multi-view 3D face morphable model regression, in: Proc. of IEEE CVPR, 2019, pp. 959–968.
- [123] H. Yi, C. Li, Q. Cao, X. Shen, S. Li, G. Wang, Y.-W. Tai,

- Mmface: A multi-metric regression network for unconstrained face reconstruction, in: Proc. of IEEE CVPR, 2019, pp. 7663–7672.
- [124] J. Piao, C. Qian, H. Li, Semi-supervised monocular 3D face reconstruction with end-to-end shape-preserved domain transfer, in: Proc. of IEEE ICCV, 2019, pp. 9398–9407.
- [125] J. S. Yoon, T. Shiratori, S.-I. Yu, H. S. Park, Self-supervised adaptation of high-fidelity face models for monocular performance tracking, in: Proc. of IEEE CVPR, 2019, pp. 4601–4609.
- [126] P. Wang, Y. Tian, W. Che, B. Xu, Efficient and accurate face shape reconstruction by fusion of multiple landmark databases, in: Proc. of ICIP, 2019, pp. 335–339.
- [127] N. Savov, M. Ngo, S. Karaoglu, H. Dibeklioglu, T. Gevers, Pose and expression robust age estimation via 3D face reconstruction from a single image, in: Proc. of IEEE ICCV Workshops, 2019, pp. 1270–1278.
- [128] E. Ramon, J. Eскур, X. Giró-i Nieto, Multi-view 3D face reconstruction in the wild using siamese networks, in: Proc. of IEEE ICCV Workshops, 2019, pp. 3096–3100.
- [129] X. Zeng, X. Peng, Y. Qiao, DF²Net: A dense-fine-finer network for detailed 3D face reconstruction, in: Proc. of IEEE ICCV, 2019, pp. 2315–2324.
- [130] Z. Bai, Z. Cui, J. A. Rahim, X. Liu, P. Tan, Deep facial non-rigid multi-view stereo, in: Proc. of IEEE CVPR, 2020, pp. 5849–5859.
- [131] N. Chinaev, A. Chigorin, I. Laptev, Mobileface: 3D face reconstruction with efficient CNN regression, in: Proc. of ECCV Workshops, 2018.
- [132] B. Chaudhuri, N. Veddapunt, B. Wang, Joint face detection and facial motion retargeting for multiple faces, in: Proc. of IEEE CVPR, 2019, pp. 9719–9728.
- [133] B. Chaudhuri, N. Veddapunt, L. Shapiro, B. Wang, Personalized face modeling for improved face reconstruction and motion retargeting, in: Proc. of ECCV, 2020.
- [134] G. Zhang, H. Han, S. Shan, X. Song, X. Chen, Face alignment across large pose via MT-CNN based 3D shape reconstruction, in: Proc. of IEEE FG, 2018, pp. 210–217.
- [135] J. Guo, X. Zhu, Y. Yang, F. Yang, Z. Lei, S. Z. Li, Towards fast, accurate and stable 3D dense face alignment, in: Proc. of ECCV, 2020.
- [136] J. Lin, Y. Yuan, T. Shao, K. Zhou, Towards high-fidelity 3D face reconstruction from in-the-wild images using graph convolutional networks, in: Proc. of IEEE CVPR, 2020, pp. 5891–5900.
- [137] J. Shang, T. Shen, S. Li, L. Zhou, M. Zhen, T. Fang, L. Quan, Self-supervised monocular 3D face reconstruction by occlusion-aware multi-view geometry consistency, in: Proc. of ECCV, 2020.
- [138] T. Koizumi, W. Smith, "look ma, no landmarks!" - unsupervised, model-based dense face alignment, in: Proc. of ECCV, 2020.
- [139] A. Lattas, S. Moschoglou, B. Gecer, S. Ploumpis, V. Triantafyllou, A. Ghosh, S. Zafeiriou, AvatarMe: Realistically renderable 3D facial reconstruction "in-the-wild", in: Proc. of IEEE CVPR, 2020.
- [140] P. Wang, C. Lin, B. Xu, W. Che, Q. Wang, Low-frequency guided self-supervised learning for high-fidelity 3D face reconstruction in the wild, in: Proc. of IEEE ICME, 2020, pp. 1–6.
- [141] A. Tewari, F. Bernard, P. Garrido, G. Bharaj, M. Elgharib, H.-P. Seidel, P. Pérez, M. Zollhofer, C. Theobalt, FML: Face model learning from videos, in: Proc. of IEEE CVPR, 2019, pp. 10812–10822.
- [142] X. Chai, J. Chen, C. Liang, D. Xu, C. Lin, Expression-aware face reconstruction via a dual-stream network, in: Proc. of IEEE ICME, 2020, pp. 1–6.
- [143] X. Fan, S. Cheng, K. Huyan, M. Hou, R. Liu, Z. Luo, Dual neural networks coupling data regression with explicit priors for monocular 3D face reconstruction, IEEE Trans. Multimedia (Early Access) (2020).
- [144] X. Li, Z. Weng, J. Liang, L. Cei, Y. Xiang, Y. Fu, A novel two-pathway encoder-decoder network for 3D face reconstruction, in: Proc. of IEEE ICASSP, 2020, pp. 3682–3686.
- [145] X. Tu, J. Zhao, M. Xie, Z. Jiang, A. Balamurugan, Y. Luo, Y. Zhao, L. He, Z. Ma, J. Feng, 3D face reconstruction from a single image assisted by 2d face images in the wild, IEEE Trans. Multimedia (Early Access) (2020).
- [146] X. Wang, Y. Guo, B. Deng, J. Zhang, Lightweight photometric stereo for facial details recovery, in: Proc. of IEEE CVPR, 2020, pp. 740–749.
- [147] X. Zhu, F. Yang, D. Huang, C. Yu, H. Wang, J. Guo, Z. Lei, S. Z. Li, Beyond 3DMM space: Towards fine-grained 3D face reconstruction, in: Proc. of ECCV, 2020.
- [148] Y. Chen, F. Wu, Z. Wang, Y. Song, Y. Ling, L. Bao, Self-supervised learning of detailed 3D face reconstruction, IEEE Trans. Image Process. 29 (2020) 8696–8705.
- [149] Z. Gao, J. Zhang, Y. Guo, C. Ma, G. Zhai, X. Yang, Semi-supervised 3D face representation learning from unconstrained photo collections, in: Proc. of IEEE CVPR Workshops, 2020, pp. 348–349.
- [150] Z. Shu, D. Ceylan, K. Sunkavalli, E. Shechtman, S. Hadap, D. Samaras, Learning monocular face reconstruction using multi-view supervision, in: Proc. of IEEE FG, 2020, pp. 762–769.
- [151] T.-C. Wang, M.-Y. Liu, J.-Y. Zhu, A. Tao, J. Kautz, B. Catanzaro, High-resolution image synthesis and semantic manipulation with conditional GANs, in: Proc. of IEEE CVPR, 2018, pp. 8798–8807.
- [152] S. Romdhani, T. Vetter, Estimating 3D shape and texture using pixel intensity, edges, specular highlights, texture constraints and a prior, in: Proc. of IEEE CVPR, volume 2, 2005, pp. 986–993.
- [153] P. J. Phillips, P. J. Flynn, T. Scruggs, K. W. Bowyer, J. Chang, K. Hoffman, J. Marques, J. Min, W. Worek, Overview of the face recognition grand challenge, in: Proc. of IEEE CVPR, 2005, pp. 947–954.
- [154] S. Lombardi, J. Saragih, T. Simon, Y. Sheikh, Deep appearance models for face rendering, ACM Trans. Graph. 37 (2018) 68:1–68:13.
- [155] P. J. Phillips, W. T. Scruggs, A. J. O’Toole, P. J. Flynn, K. W. Bowyer, C. L. Schott, M. Sharpe, FRVT 2006 and ICE 2006 large-scale experimental results, IEEE Trans. on Pattern Anal. and Machine Intel. 32 (2009) 831–846.
- [156] L. Yin, X. Wei, Y. Sun, J. Wang, M. J. Rosato, A 3D facial expression database for facial behavior research, in: Proc. of IEEE FG, 2006, pp. 211–216.
- [157] Y. Wu, S. K. Shah, I. A. Kakadiaris, Rendering or normalization? An analysis of the 3D-aided pose-invariant face recognition, in: Proc. of IEEE ISBA, 2016, pp. 1–8.
- [158] G. Stratou, A. Ghosh, P. Debevec, L.-P. Morency, Effect of illumination on automatic expression recognition: a novel 3D relightable facial database, in: Proc. of IEEE FG, 2011, pp. 611–618.
- [159] S. Zafeiriou, M. Hansen, G. Atkinson, V. Argyriou, M. Petrou, M. Smith, L. Smith, The Photoface database, in: Proc. of IEEE CVPR Workshops, 2011, pp. 132–139.
- [160] B.-C. Chen, C.-S. Chen, W. H. Hsu, Cross-age reference coding for age-invariant face recognition and retrieval, in: Proc. of ECCV, 2014, pp. 768–783.
- [161] W.-C. Ma, T. Hawkins, P. Peers, C.-F. Chabert, M. Weiss, P. Debevec, Rapid acquisition of specular and diffuse normal maps from polarized spherical gradient illumination, in: Eurographics conference on Rendering Techniques, 2007, pp. 183–194.
- [162] A. G. Howard, M. Zhu, B. Chen, D. Kalenichenko, W. Wang, T. Weyand, M. Andreetto, H. Adam, Mobilenets: Efficient convolutional neural networks for mobile vision applications, arXiv preprint arXiv:1704.04861 (2017).
- [163] F. N. Iandola, S. Han, M. W. Moskewicz, K. Ashraf, W. J. Dally, K. Keutzer, SqueezeNet: Alexnet-level accuracy with 50x fewer parameters and 0.5MB model size, arXiv preprint arXiv:1602.07360 (2016).

- [164] J. Hu, L. Shen, G. Sun, Squeeze-and-excitation networks, in: Proc. of IEEE CVPR, 2018, pp. 7132–7141.
- [165] K. Simonyan, A. Zisserman, Very deep convolutional networks for large-scale image recognition, in: Proc. of ICLR, 2015.
- [166] A. Krizhevsky, I. Sutskever, G. E. Hinton, ImageNet classification with deep convolutional neural networks, in: Proc. of NIPS, 2012, pp. 1097–1105.
- [167] I. Misra, A. Shrivastava, A. Gupta, M. Hebert, Cross-stitch networks for multi-task learning, in: Proc. of IEEE CVPR, 2016, pp. 3994–4003.
- [168] B. Vallet, B. Lévy, Spectral geometry processing with manifold harmonics, in: Comput. Graph. Forum, volume 27, 2008, pp. 251–260.
- [169] K. He, X. Zhang, S. Ren, J. Sun, Deep residual learning for image recognition, in: Proc. of IEEE CVPR, 2016, pp. 770–778.
- [170] O. Ronneberger, P. Fischer, T. Brox, U-net: Convolutional networks for biomedical image segmentation, in: Proc of MIC-CAI, 2015, pp. 234–241.
- [171] J. Bromley, I. Guyon, Y. LeCun, E. Säckinger, R. Shah, Signature verification using a “siamese” time delay neural network, in: Proc. of NIPS, 1993, pp. 737–744.
- [172] K. Zhang, Z. Zhang, Z. Li, Y. Qiao, Joint face detection and alignment using multitask cascaded convolutional networks, IEEE Signal Process. Lett. 23 (2016) 1499–1503.
- [173] A. Newell, K. Yang, J. Deng, Stacked hourglass networks for human pose estimation, in: Proc. of ECCV, 2016, pp. 483–499.
- [174] J. S. Yoon, F. Rameau, J. Kim, S. Lee, S. Shin, I. So Kweon, Pixel-level matching for video object segmentation using convolutional neural networks, in: Proc. of IEEE ICCV, 2017, pp. 2167–2176.
- [175] A. Ranjan, T. Bolkart, S. Sanyal, M. J. Black, Generating 3D faces using convolutional mesh autoencoders, in: Proc. of ECCV, 2018, pp. 725–741.
- [176] W. Liu, Y. Wen, Z. Yu, M. Li, B. Raj, L. Song, SphereFace: Deep hypersphere embedding for face recognition, in: Proc. of IEEE CVPR, 2017, pp. 212–220.
- [177] F. Schroff, D. Kalenichenko, J. Philbin, FaceNet: A unified embedding for face recognition and clustering, in: Proc. of IEEE CVPR, 2015, pp. 815–823.
- [178] D. K. Hammond, P. Vandergheynst, R. Gribonval, Wavelets on graphs via spectral graph theory, Appl. Comput. Harmon. Anal. 30 (2011) 129–150.
- [179] M. Defferrard, X. Bresson, P. Vandergheynst, Convolutional neural networks on graphs with fast localized spectral filtering, in: Proc. of NIPS, 2016, p. 3844–3852.
- [180] T. Karras, T. Aila, S. Laine, J. Lehtinen, Progressive growing of GANs for improved quality, stability, and variation, in: Proc. of ICLR, 2018.
- [181] J.-Y. Zhu, T. Park, P. Isola, A. A. Efros, Unpaired image-to-image translation using cycle-consistent adversarial networks, in: Proc. of IEEE ICCV, 2017, pp. 2223–2232.
- [182] G. Huang, Z. Liu, L. Van Der Maaten, K. Q. Weinberger, Densely connected convolutional networks, in: Proc. of IEEE CVPR, 2017, pp. 2261–2269.
- [183] O. M. Parkhi, A. Vedaldi, A. Zisserman, Deep face recognition, in: Proc. of BMVC, 2015, pp. 41:1–41:12.
- [184] B. Hariharan, P. Arbeláez, R. Girshick, J. Malik, Hypercolumns for object segmentation and fine-grained localization, in: Proc. of IEEE CVPR, 2015, pp. 447–456.
- [185] P. Isola, J.-Y. Zhu, T. Zhou, A. A. Efros, Image-to-image translation with conditional adversarial networks, in: Proc. of IEEE CVPR, 2017, pp. 1125–1134.
- [186] R. Or-El, G. Rosman, A. Wetzler, R. Kimmel, A. M. Bruckstein, RGBD-fusion: Real-time high precision depth recovery, in: Proc. of IEEE CVPR, 2015, pp. 5407–5416.
- [187] Y. Zhang, K. Li, K. Li, L. Wang, B. Zhong, Y. Fu, Image super-resolution using very deep residual channel attention networks, in: Proc. of ECCV, 2018, pp. 294–310.
- [188] D. Sun, X. Yang, M. Liu, J. Kautz, PWC-Net: CNNs for optical flow using pyramid, warping, and cost volume, in: Proc. of IEEE CVPR, 2018, pp. 8934–8943.
- [189] I. Gulrajani, F. Ahmed, M. Arjovsky, V. Dumoulin, A. Courville, Improved training of Wasserstein GANs, in: Proc. of NIPS, 2017, p. 5769–5779.
- [190] R. Girshick, Fast R-CNN, in: Proc. of IEEE ICCV, 2015, pp. 1440–1448.
- [191] P. Dou, Y. Wu, S. K. Shah, I. A. Kakadiaris, Robust 3D face shape reconstruction from single images via two-fold coupled structure learning, in: Proc. of BMVC, 2014, pp. 1–13.
- [192] L. A. Jeni, J. F. Cohn, T. Kanade, Dense 3D face alignment from 2D videos in real-time, in: Proc. of IEEE FG, 2015, pp. 1–8.
- [193] L. A. Jeni, J. F. Cohn, T. Kanade, Dense 3D face alignment from 2D video for real-time use, Image Vis. Comput. 58 (2017) 13–24.
- [194] F. Liu, D. Zeng, Q. Zhao, X. Liu, Joint face alignment and 3D face reconstruction, in: Proc. of ECCV, 2016, pp. 545–560.
- [195] F. Liu, D. Zeng, J. Li, Q.-j. Zhao, On 3D face reconstruction via cascaded regression in shape space, Front. Inf. Technol. Electron. Eng. 18 (2017) 1978–1990.
- [196] H. M. Rara, S. Elhabian, T. Starr, A. A. Farag, 3D face recovery from intensities of general and unknown lighting using partial least squares, in: Proc. of ICIP, 2010, pp. 4041–4044.
- [197] H. M. Rara, A. A. Farag, T. Davis, Model-based 3D shape recovery from single images of unknown pose and illumination using a small number of feature points, in: Proc. of IJCB, 2011, pp. 1–7.
- [198] D. Sánchez-Escobedo, M. Castelán, W. A. Smith, Statistical 3D face shape estimation from occluding contours, Comput. Vis. Image Underst. 142 (2016) 111–124.
- [199] W. Tian, F. Liu, Q. Zhao, Landmark-based 3D face reconstruction from an arbitrary number of unconstrained images, in: Proc. of IEEE FG, 2018, pp. 774–779.
- [200] P. Geladi, B. R. Kowalski, Partial least-squares regression: a tutorial, Analytica Chimica Acta 185 (1986) 1–17.
- [201] F. Liu, Q. Zhao, D. Zeng, et al., Joint face alignment and 3D face reconstruction with application to face recognition, IEEE Trans. on Pattern Anal. and Machine Intel. 42 (2020) 664–678.
- [202] S. Wang, X. Shen, J. Liu, Dense optical flow variation based 3D face reconstruction from monocular video, in: Proc. of ICIP, 2018, pp. 2665–2669.
- [203] R. Garg, A. Roussos, L. Agapito, A variational approach to video registration with subspace constraints, Int. J. Comput. Vis. 104 (2013) 286–314.